Spectroscopic Studies of Abiotic and Biological Nanomaterials: Silver Nanoparticles, Rhodamine 6G Adsorbed on Graphene, and *c*-Type Cytochromes and Type IV Pili in *Geobacter sulfurreducens*

Elizabeth S. Thrall

Submitted in partial fulfillment of the

requirements for the degree of

Doctor of Philosophy

under the Executive Committee

of the Graduate School of Arts and Sciences

COLUMBIA UNIVERSITY

2012

ABSTRACT

Spectroscopic Studies of Abiotic and Biological Nanomaterials: Silver Nanoparticles, Rhodamine 6G Adsorbed on Graphene, and *c*-Type Cytochromes and Type IV Pili in *Geobacter sulfurreducens*

Elizabeth S. Thrall

This thesis describes spectroscopic studies of three different systems: silver nanoparticles, the dye molecule rhodamine 6G adsorbed on graphene, and the type IV pili and *c*-type cytochromes produced by the dissimilatory metal-reducing bacterium *Geobacter sulfurreducens*. Although these systems are quite different in some ways, they can all be considered examples of nanomaterials. A nanomaterial is generally defined as having at least one dimension below 100 nm in size. Silver nanoparticles, with sub-100 nm size in all dimensions, are examples of zero-dimensional nanomaterials. Graphene, a single atomic layer of carbon atoms, is the paradigmatic two-dimensional nanomaterial. And although bacterial cells are on the order of 1 μm in size, the type IV pili and multiheme *c*-type cytochromes produced by *G. sulfurreducens* can be considered to be one- and zero-dimensional nanomaterials respectively. A further connection between these systems is their strong interaction with visible light, allowing us to study them using similar spectroscopic tools.

The first chapter of this thesis describes research on the plasmon-mediated photochemistry of silver nanoparticles. Silver nanoparticles support coherent electron

oscillations, known as localized surface plasmons, at resonance frequencies that depend on the particle size and shape and the local dielectric environment. Nanoparticle absorption and scattering cross-sections are maximized at surface plasmon resonance frequencies, and the electromagnetic field is amplified near the particle surface. Plasmonic effects can enhance the photochemistry of silver particles alone or in conjunction with semiconductors according to several mechanisms. We study the photooxidation of citrate by silver nanoparticles in a photoelectrochemical cell, focusing on the wavelength-dependence of the reaction rate and the role of the semiconductor substrate. We find that the citrate photooxidation rate does not track the plasmon resonance of the silver nanoparticles but instead rises monotonically with photon energy. These results are discussed in terms of plasmonic enhancement mechanisms and a theoretical model describing hot carrier photochemistry.

The second chapter explores the electronic absorption and resonance Raman scattering of the dye molecule rhodamine 6G (R6G) adsorbed on graphene. Graphene has been shown to quench the fluorescence of adsorbed molecules and quantum dots, and some previous studies have reported that the Raman scattering from molecules adsorbed on graphene is enhanced. We show that reflective contrast spectroscopy can be used to obtain the electronic absorption spectrum of R6G adsorbed on graphene, allowing us to estimate the surface concentration of the dye molecule. From these results we are able to calculate the absolute Raman scattering cross-section for R6G adsorbed on bilayer graphene. We find that there is no evidence of enhancement but instead that the cross-section is reduced by more than three-fold from its value in solution. We further show

that a model incorporating electromagnetic interference effects can reproduce the observed dependence of the R6G Raman intensity on the number of graphene layers.

The third and final chapter describes the preliminary results from studies of the dissimilatory metal-reducing bacterium *Geobacter sulfurreducens*. This anaerobic bacterium couples the oxidation of organic carbon sources to the reduction of iron oxides and other extracellular electron acceptors, a type of anaerobic respiration that necessitates an electron transport chain that can move electrons from the interior of the cell to the extracellular environment. The electron transport chain in *G. sulfurreducens* has not been completely characterized and two competing mechanisms for the charge transport have been proposed. The first holds that *G. sulfurreducens* produces type IV pili, protein filaments several nanometers in width, with intrinsic metallic-like conductivity. According to this mechanism, the conductive pili mediate electron transport to extracellular acceptors. The second proposed mechanism is that charge transport proceeds by electron hopping between the heme groups in the many *c*-type cytochromes produced by *G. sulfurreducens*. In this picture, the observed conductivity of the pili is due to hopping through associated cytochrome proteins. Our aim is to explore these alternative mechanisms for electron transport in *G. sulfurreducens* through electrical and optical studies. We report the work we have done thus far to culture and characterize *G. sulfurreducens*, and we show that preliminary micro-Raman studies of *G. sulfurreducens* cells confirm that we can detect the spectroscopic signature of *c*-type cytochrome proteins. Future directions for this ongoing work are briefly discussed.

Table of Contents

List of Figures

Chapter 1:

Chapter 2:

Chapter 3:

Acknowledgments

I have benefited from the help and encouragement of many people over the past five years, without which this thesis would not have been possible. Above all, I thank my advisor Professor Louis Brus for everything that he has done to teach and guide me. I have benefited immensely from the opportunity to work with such an insightful scientist and a genuinely kind person. If I take one thing from my time in the Brus group, I hope it is the lesson that the most important thing in science is to ask the right questions. I may not always succeed in that goal, but I will certainly try.

I feel particularly fortunate in my graduate committee. My first introduction to graphene came during a summer working in Professor Colin Nuckolls's lab, and I have always benefited from his suggestions and advice. I have had many helpful conversations with Professor Ruben Gonzalez over the years and have particularly appreciated his encouragement since embarking on a new research project in biology. I have already learned a great deal from Professor Lars Dietrich, our collaborator on the *Geobacter* project, and I am excited to continue this work in the coming year. I thank Professor Laura Kaufman for agreeing to serve on my thesis defense committee and I look forward to her comments and suggestions.

I also thank Dr. Mike Steigerwald for the insight and advice, scientific and otherwise, which he has shared with me on numerous occasions.

Working in three different fields means that I have three times as many people to thank. I thank Dr. Xiaomu Wu for helping me get started on the silver nanoparticle photoelectrochemistry project. Dr. Andrew Crowther gave me an excellent training in spectroscopy and practical optics, and I thank him for all his assistance with the

rhodamine 6G-graphene project. The work I have done so far with *Geobacter* would have been completely impossible without Professor Lars Dietrich and his lab. I have been helped many times by Dr. Matt Sekedat, Dr. Dave Recinos, Chinweike Okegbe, and Hassan Sakhtah. I have benefited greatly from the expertise and experience of Dr. Zhonghua Yu and I thank him for all of his assistance. I also thank Dr. Steffen Jockusch, Dr. Alon Gorodetsky, Dr. Anna Lee and Professor Thomas Mallouk, Kevin Watkins and Professor Bruce Parkinson, Dr. Kin Fai Mak, Professor Daniel Bond, and Dr. Nicolas Biais.

At one point or another, every member of the Brus group has helped me in some way, and I thank Dr. Sunmin Ryu, Dr. Haitao Liu, Dr. Stéphane Berciaud, Dr. Shu Li, Dr. Naeyoung Jung, Dr. Zheyuan Chen, Dr. Cyrielle Roquelet, Dr. Melinda Han, Yinsheng Guo, and Giselle Elbaz. I had the chance to work with two very bright and dedicated undergraduates in the Brus lab. Diana Lee studied the photochemical synthesis of decahedral silver nanoparticles and Asher Preska Steinberg conducted photoelectrochemical experiments with Ag nanoparticles supported on *n*-TiO_2 single crystals.

I also want to acknowledge the wonderful friends I've made in the chemistry department over the past five years, especially Manasi Bhate, Richard Darst, Joseph Moll, and Carl Smith. And of course I am grateful to all my friends and family for their encouragement and general willingness to listen to me talk about my research. My parents have always been supportive and have helped me in so many ways over the years. I hope that I can continue to make them proud. My maternal grandmother, an organic

chemist, was and remains an inspiration to me and I hope that she would have enjoyed this thesis.

Finally, I thank my wife Giselle Schuetz for her support throughout my Ph.D., but especially during this past summer—when I wasn't a lot of fun and she had to take on more than her fair share of everything other than thesis-writing. I also thank her for the careful proofreading of my completed thesis chapters. And more than anything, I thank her for her suggestion almost 10 years ago that we should start doing our Physics 15a problem sets together. That was easily the best decision of my life.

To Giselle

Chapter 1

Plasmon-Mediated Photoelectrochemistry of Adsorbed Molecules on Silver Nanoparticles

Although metal photochemistry is relatively uncommon, there is growing interest in the photo(electro)chemical properties of noble metal nanoparticles with strong localized surface plasmon resonances. One example of noble metal photochemistry is the photooxidation of citrate ions adsorbed on silver (Ag) nanoparticles at low incident light intensities. Here we report the wavelength-dependence of citrate photooxidation by Ag nanoparticles supported on indium tin oxide (ITO) in a photoelectrochemical cell. Both the photovoltage and photocurrent of the Ag nanoparticle electrode increase monotonically with increasing photon energy for the three types of nanoparticles studied: quasi-spherical nanoparticles fabricated by thermal or electron-beam evaporation, colloidal nanoprisms deposited from solution, and colloidal nanospheres deposited from solution. The electrode photoresponse does not closely track the plasmon absorbance of the Ag nanoparticles, especially for the colloidal nanoprisms, which have a maximum absorption in the near infrared. We also explore the role of the nanoparticle substrate in citrate photooxidation. The observed wavelength-dependence of the photooxidation rate can be explained by a theoretical model of hot carrier photochemistry. A similar spectral dependence of surface photochemistry on Ag colloids has been observed for other adsorbates and has been attributed to charge-transfer transitions.

1.1 Introduction to Plasma Oscillations

1.1.1 Bulk Plasmons in the Drude Model

Metals are distinguished by their mobile valence electrons, the behavior of which is central to metallic electrical, thermal, and optical properties. One consequence of these free charge carriers is that metals can support various kinds of plasma oscillations. Plasma oscillations are coherent oscillations of the conduction electrons in a metal; the corresponding quantization of a plasma oscillation is the plasmon. A simple picture of plasmons in a bulk metal can be obtained from the Drude model of electrical conduction.[1] The Drude model extends the kinetic theory of gases to metals, treating the conduction electrons as a mobile gas of particles that interact only through collisions. These collisions occur with a probability per unit time of $1/\tau$, where the quantity τ is called the relaxation time. After a collision, which is considered to occur instantaneously, the electron continues traveling with a new velocity, the magnitude of which is set by the local temperature in the spot of the collision and the direction of which is assumed to be random. Between collisions, electrons do not interact at all with other electrons or with the positively-charged atomic cores of the lattice. Any motion of the ionic cores is neglected.

From these assumptions, an equation of motion for the electron gas can be derived:

$$m\left(\frac{d^2\mathbf{r}(t)}{dt^2}+\frac{1}{\tau}\frac{d\mathbf{r}(t)}{dt}\right)=\mathbf{f}(t) \qquad 1.1$$

where $\mathbf{r}(t)$ is the electron displacement from equilibrium and $\mathbf{f}(t)$ is some force on the system, presumed to be acting equally on all electrons in the gas. The second quantity on the left side of the equation has the form of a frictional damping term that arises from electron scattering events. An incident electromagnetic wave can be treated to first approximation as a spatially uniform electric field oscillating in time, as the force due to the magnetic component is negligible. In this case, the equation of motion becomes:

$$m\left(\frac{d^2\mathbf{r}(t)}{dt^2}+\frac{1}{\tau}\frac{d\mathbf{r}(t)}{dt}\right)=-e\mathbf{E}(t) \tag{1.2}$$

where the charge of the electron is $-e$ and the electric field is $\mathbf{E}(t)$. If the electric field is assumed to be of the form:

$$\mathbf{E}(t)=\mathrm{Re}\left(\mathbf{E}_0 e^{-i\omega t}\right) \tag{1.3}$$

where ω is the angular frequency, then a solution to Equation 1.2 can be found in the form of:

$$\mathbf{r}(t)=\mathrm{Re}\left(\mathbf{r}_0 e^{-i\omega t}\right) \tag{1.4}$$

Substitution into Equation 1.2 yields for $\mathbf{r}_0$:

$$\mathbf{r}_0=\frac{e\mathbf{E}_0}{m\left(\omega^2+\frac{i\omega}{\tau}\right)} \tag{1.5}$$

The displacement of an electron from its equilibrium position generates a dipole moment:

$$\mathbf{p}(\mathbf{r},t)=-e\mathbf{r}(t) \tag{1.6}$$

The polarization density, $\mathbf{P}(\mathbf{r},t)$, of the electron gas is the dipole moment per unit volume. Multiplication by the total number of electrons in the gas, N, and division by the volume, V, gives $\mathbf{P}(\mathbf{r},t)$ as:

$$\mathbf{P}(\mathbf{r},t) = -ne\mathbf{r}(t) \tag{1.7}$$

where $n = N/V$ is the electron density. The dielectric function $\varepsilon(\omega)$ can be obtained from $\mathbf{P}(\mathbf{r},t)$ as:

$$\begin{aligned}\varepsilon(\omega) &= \frac{\mathbf{D}(\mathbf{r},t)}{\mathbf{E}(\mathbf{r},t)} \\ &= 1 + 4\pi\frac{\mathbf{P}(\mathbf{r},t)}{\mathbf{E}(\mathbf{r},t)} \\ &= 1 - \frac{4\pi ne^2}{m\left(\omega^2 + \frac{i\omega}{\tau}\right)} \\ &= 1 - \frac{\omega_p^2}{\omega^2 + \frac{i\omega}{\tau}}\end{aligned} \tag{1.8}$$

Here $\mathbf{D}(\mathbf{r},t)$ is the electric displacement and $\omega_p = \sqrt{(4\pi ne^2/m)}$ is the plasma frequency. (Please note that equations in this chapter are written in Gaussian electromagnetic units.)

The propagation of light in the electron gas depends on $\varepsilon(\omega)$. The wave equation for the electric field component of the electromagnetic wave is:

$$-\nabla^2\mathbf{E}(\mathbf{r},t) = \frac{\omega^2}{c^2}\varepsilon(\omega)\mathbf{E}(\mathbf{r},t) \tag{1.9}$$

where c is the speed of light. A solution to Equation 1.9 is given by:

$$\begin{aligned}\mathbf{E}(\mathbf{r},t) &= \mathbf{E}_0 e^{i(\mathbf{k}\cdot\mathbf{r}-\omega t)} \\ &= \mathbf{E}_0 e^{i(\sqrt{\varepsilon}\frac{\omega}{c}\mathbf{r}\cdot\hat{\mathbf{s}}-\omega t)}\end{aligned} \tag{1.10}$$

where $\mathbf{k}$ is the wave vector and $\hat{\mathbf{s}}$ is a unit vector in the direction of propagation of the wave. Thus $\varepsilon(\omega)$ determines the spatial propagation of light in the electron gas. Equation 1.8 for $\varepsilon(\omega)$ can be simplified further in the high-frequency limit, where $\omega\tau \gg 1$:

$$\varepsilon(\omega) = 1 - \frac{\omega_p^2}{\omega^2} \tag{1.11}$$

In this limit, $\varepsilon(\omega)$ is pure real, and two types of behavior are possible. For frequencies higher than ω_p, $\varepsilon(\omega)$ is positive and thus $\sqrt{(\varepsilon(\omega)}$ is also pure real. In this case, Equation 1.10 describes a wave propagating through the metal with no attenuation. For frequencies lower than ω_p, conversely, $\varepsilon(\omega)$ is negative and $\sqrt{(\varepsilon(\omega)}$ is pure imaginary. Here Equation 1.10 describes a wave decaying exponentially into the metal. For Drude metals, then, ω_p is the threshold frequency above which light travels through the material without attenuation—that is, above which metals become transparent. Most metals reflect visible light strongly because ω_p lies in the far ultraviolet portion of the spectrum.

There is, however, another significance to ω_p. As the name implies, it is the frequency at which a bulk metal sustains a plasma oscillation. This result can be derived formally by searching for oscillations in the metallic charge density $\rho(\omega)$ with a time dependence of $e^{-i\omega t}$, but the same conclusion can be reached using a simpler approach.[1,2] Figure 1.1 shows a bulk metal with the electron gas offset from the ionic background by a distance d in one direction. This displacement of the electron gas leaves surface charges of opposite sign but equal magnitude at the ends of the metal. If the density of conduction electrons is n per cm^3, the surface charge is given by $\sigma_q = \pm nde$, in units of $statC \cdot cm^{-2}$. The electric field between the surface charges, in the bulk of the metal, is given by $E = 4\pi\sigma_q = 4\pi nde$. The displaced electrons will feel a Coulombic restoring force from the ionic background, causing them to oscillate. If the total number of electrons in the gas is N such that the total mass is Nm, their displacement can be described by Hooke's law where M is mass and k is the spring constant:

$$M\ddot{x} = -kx \qquad 1.12$$

Substituting the total electron mass for M and the Columbic force eE for k gives:

$$\begin{aligned} Nm\ddot{d} &= -NeE \\ &= -Ne(4\pi nde) \end{aligned} \tag{1.13}$$

Finally, rearranging to find the oscillation frequency reveals that the gas oscillates at the plasma frequency ω_p:

$$\ddot{d} = -\frac{4\pi ne^2}{m} d = -\omega_p^2 d \tag{1.14}$$

Although the correct expression for the plasma frequency can be derived from this simple model, the schematic in Figure 1.1 should not be taken literally. The bulk plasma oscillation is not a mere displacement of the electron gas across the whole lattice but instead is a propagating longitudinal excitation of the electron gas, distinct from the transverse optical modes excited for $\omega \neq \omega_p$.[2]

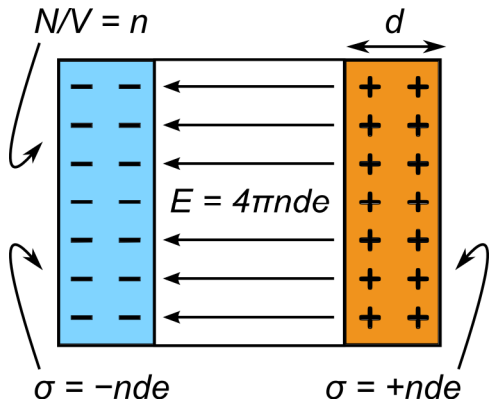

Figure 1.1 Schematic of a bulk plasma oscillation. The electron cloud is displaced from the positively-charged lattice by a distance d, generating surface charges of $\sigma = \pm nde$ and an electric field $E = 4\pi nde$.

1.1.2 Localized Surface Plasmons

For a metal particle with dimensions smaller than the wavelength of light, λ, non-propagating plasmon modes can be excited at lower energies than the energy of the bulk plasmon, $\hbar\omega_p$. These modes are called surface plasmon modes, or sometimes localized surface plasmon modes (LSPs) to distinguish them from the propagating surface plasmons (SPs) that exist at the interface between a metal surface and a dielectric medium.[3-5] In particles that are small compared to λ, the conduction electrons oscillate in phase across the particle. This oscillation produces polarization charges on the particle surface, exerting a restoring force on the electrons. As a result of this restoring force, the optical properties of the particle have a resonance at a characteristic frequency, which corresponds to the localized surface plasmon resonance frequency. Unlike the bulk plasmon and the propagating SP, this localized surface plasmon couples strongly to an incident electromagnetic wave.[5]

The problem of a metal particle of arbitrary shape interacting with an electromagnetic field does not have a general analytical solution, and thus there is no general expression for the localized surface plasmon resonance frequency. For spherical particles, however, Mie theory provides exact analytical expressions for the particle polarizability, α.[6,7] The resulting electric field can be determined from α, along with the particle cross-sections for interaction with the incident light. A simplified description of the behavior of small spherical particles, for which the particle radius $R \ll \lambda$, can be extracted from the quasistatic approximation.[7-10] In this model, the particle is described by the bulk frequency-dependent dielectric constant of the metal, $\varepsilon(\omega) = \varepsilon'(\omega) + i\varepsilon''(\omega)$. The particle is assumed to be embedded in a homogeneous medium of dielectric $\varepsilon_m(\omega)$.

(For simplicity, ω will be omitted in future equations, but it should be understood that ε is a function of frequency.) The geometry of this system is shown in Figure 1.2. Although frequency-dependent dielectric constants are used, the electric potential is solved in a frequency-independent manner, hence the name quasistatic approximation. In an electrostatic system with no free charge, the electric potential φ is determined by Laplace's equation:

$$\nabla^2 \varphi = 0 \tag{1.15}$$

and appropriate boundary conditions.[8] Here, the boundary conditions at the metal-medium interface require the continuity of the electric potential:

$$\varphi_1(\mathbf{r}) = \varphi_2(\mathbf{r}) \text{ at } r = R \tag{1.16}$$

and the normal component of the electric displacement $\mathbf{D}(\mathbf{r}) = \varepsilon \mathbf{E}(\mathbf{r})$:

$$\varepsilon \mathbf{E}_1(\mathbf{r}) = \varepsilon_m \mathbf{E}_2(\mathbf{r}) \text{ at } r = R \tag{1.17}$$

The electric potential inside and outside the sphere can be determined by applying the boundary conditions above to Laplace's equation:[8,9,11]

$$\begin{aligned} \varphi_1(\mathbf{r}) &= -\frac{3}{\varepsilon + 2\varepsilon_m} E_0 r \cos\theta \\ \varphi_2(\mathbf{r}) &= -E_0 r \cos\theta + \frac{\varepsilon - \varepsilon_m}{\varepsilon + 2\varepsilon_m} E_0 \frac{R^3}{r^2} \cos\theta \end{aligned} \tag{1.18}$$

The associated electric fields inside and outside the particle are:

$$\begin{aligned} \mathbf{E}_1(\mathbf{r}) &= \frac{3}{\varepsilon + 2\varepsilon_m} \mathbf{E}_0 \\ \mathbf{E}_2(\mathbf{r}) &= \mathbf{E}_0 + \frac{\varepsilon - \varepsilon_m}{\varepsilon + 2\varepsilon_m} R^3 \left(\frac{\cos\theta}{r^3} \hat{r} + \frac{\sin\theta}{r^3} \hat{\theta}\right) E_0 \end{aligned} \tag{1.19}$$

Thus the electric field inside the sphere is constant and oriented parallel to the incident field, while the electric field outside the sphere is a superposition of the incident field and

the field of a point dipole at the origin of the particle. The magnitude of the dipole scales as R^3, or as the sphere volume, and also depends on the factor $\varepsilon - \varepsilon_m/\varepsilon + 2\varepsilon_m$.

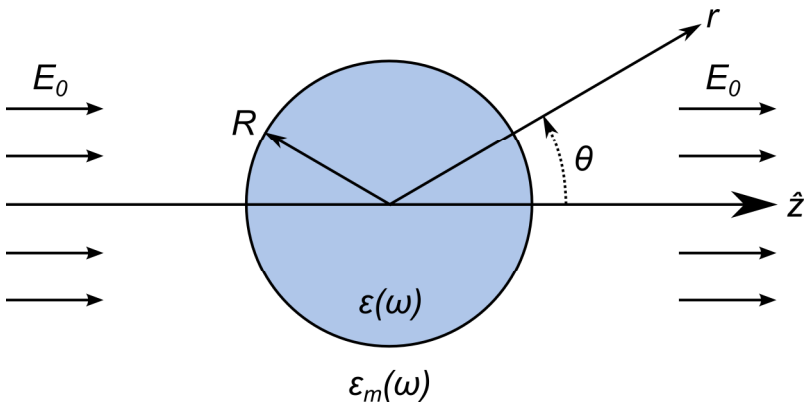

Figure 1.2 Schematic of a metal sphere of radius R and dielectric function $\varepsilon(\omega)$ in a uniform electric field. The electric field has magnitude E_0 directed along the z-axis. The dielectric function of the surrounding medium is $\varepsilon_m(\omega)$.

The internal polarization density of the particle $\mathbf{P}(\mathbf{r})$ can be determined from $\mathbf{E}_1(\mathbf{r})$:

$$\mathbf{P}(\mathbf{r}) = \frac{\varepsilon - \varepsilon_m}{4\pi}\mathbf{E} = \frac{3}{4\pi}\frac{\varepsilon - \varepsilon_m}{\varepsilon + 2\varepsilon_m}\mathbf{E}_0 \qquad 1.20$$

Here $\mathbf{P}$ is independent of $\mathbf{r}$, meaning that the sphere is uniformly polarized. The dipole moment $\mathbf{p}(\mathbf{r})$ is found by integrating the polarization density $\mathbf{P}(\mathbf{r})$ over the volume of the sphere:

$$\mathbf{p}(\mathbf{r}) = \frac{\varepsilon - \varepsilon_m}{\varepsilon + 2\varepsilon_m} R^3 \mathbf{E}_0 \qquad 1.21$$

Finally, the polarizability α is determined from the relationship $\mathbf{p} = \alpha \boldsymbol{E_0}$:

$$\alpha = \frac{\varepsilon - \varepsilon_m}{\varepsilon + 2\varepsilon_m} R^3 \qquad 1.22$$

The quantities $\mathbf{E}_1$, $\mathbf{E}_2$, $\mathbf{P}$, and $\mathbf{p}$ are all resonant when $\varepsilon + 2\varepsilon_m$ is minimized. For a non-conducting medium, ε_m is pure real and positive. Thus the resonance will occur at a frequency where the real part of the metal dielectric constant $\varepsilon' = -2\varepsilon_m$. A negative ε' is required to sustain a localized surface plasmon resonance in a non-conducting medium, which is why they are only observed for metallic (*i.e.*, conducting) particles. The frequency-dependence of the plasmon resonance enters through the dispersion in ε and ε_m; for a given metal and medium, the resonance condition will only be satisfied for a certain frequency range. That the surface plasmon resonance occurs at lower frequency than the bulk plasmon can be rationalized by setting $\varepsilon = -2\varepsilon_m$ rather than $\varepsilon = 0$ in Equation 1.11. Solving for ω gives:

$$\omega = \frac{\omega_p}{\sqrt{1 + 2\varepsilon_m}} \qquad 1.23$$

Equation 1.23 predicts that the surface plasmon resonance frequency will be a factor of $1/\sqrt{3}$ lower than the bulk plasmon frequency for a particle in vacuum ($\varepsilon_m = 1$).[5] Further, it indicates that the surface plasmon will be shifted to even lower frequency in a medium with $\varepsilon_m > 1$. This same prediction could also be made by considering the wavelength dependence of ε for a metal like Ag. Because ε' becomes more negative with increasing wavelength in the relevant part of the spectrum, the resonance for $\varepsilon_m > 1$ will be satisfied at longer wavelength.[8]

The magnitude of $(\varepsilon + 2\varepsilon_m)^{-1}$, or equivalently the strength of the resonance, depends on the imaginary part of the metal dielectric constant, ε''. A smaller ε'' translates to a larger value of $(\varepsilon + 2\varepsilon_m)^{-1}$ and thus a stronger resonance. In addition to the

contribution of the Drude term to ε'' (Equation 1.8), which accounts for intraband scattering processes, interband transitions also contribute to ε''. In metals like Au and Ag, the relevant interband transitions are excitations from the filled *d*-band to the partially-filled *sp*-band.[4] An additional frequency-dependent term, ε_{ib}, can be added to the Drude expression $\varepsilon(\omega)$ to account for interband transitions:[12]

$$\varepsilon(\omega) = \varepsilon_{ib}(\omega) + 1 - \frac{\omega_p^2}{\omega^2 + \frac{i\omega}{\tau}} \tag{1.24}$$

These factors explain why some metals—notably the noble metals and alkali metals—display a strong surface plasmon response, while others do not. For an Ag particle in vacuum, the resonance occurs at approximately 354 nm, where $\varepsilon = -2.00 + 0.28i$.[13] The small value of ε'' reflects both the high conductivity of Ag (hence a small Drude component) and the absence of interband transitions at this wavelength (and thus a small ε_{ib} component). Metals like Au and Cu also have high conductivities and thus small Drude contributions to ε'', but more significant interband transitions at their resonance wavelength.[12] The surface plasmon resonances of many transition metals are damped by relatively low conductivities.

From the polarizability α, the scattering and absorption cross-sections, σ_{scat} and σ_{abs} can be written as:[14]

$$\begin{aligned} \sigma_{scat} &= \frac{128\pi^5 \varepsilon_m^2}{3\lambda^4} |\alpha|^2 = \frac{128\pi^5 R^6 \varepsilon_m^2}{3\lambda^4} \left| \frac{\varepsilon - \varepsilon_m}{\varepsilon + 2\varepsilon_m} \right|^2 \\ \sigma_{abs} &= \frac{8\pi^2 \sqrt{\varepsilon_m}}{\lambda} \mathrm{Im}(\alpha) = \frac{8\pi^2 R^3 \sqrt{\varepsilon_m}}{\lambda} \mathrm{Im}\left(\frac{\varepsilon - \varepsilon_m}{\varepsilon + 2\varepsilon_m} \right) \end{aligned} \tag{1.25}$$

The absorption cross-section is dependent on the imaginary part of $(\varepsilon - \varepsilon_m)/(\varepsilon + 2\varepsilon_m)$, while the scattering cross-section depends on the magnitude of the same term. As a result

of this dependence, both cross-sections have a resonance at the same values of ε and ε_m, which occurs at the same frequency as the resonances in **E**, **P**, and **p** above. Notably, σ_{abs} scales as R^3—or as volume V—while σ_{scat} scales as V^2. Thus absorption dominates for small particles and scattering becomes more significant with increasing particle size. Scattering and absorption efficiencies are obtained by dividing the cross-sections (Equation 1.25) by the geometrical cross-sectional area of the particle, $A = \pi R^2$. Figure 1.3a shows the scattering and absorption efficiencies for spherical Ag particles of R = 10, 20, and 30 nm, with the Ag dielectric function taken from Johnson and Christy.[13] The dipolar plasmon resonance at λ = 368 nm appears in both the scattering and absorption efficiencies for all three particle sizes, although absorption is stronger for the R = 10 and 20 nm particles and scattering is stronger for the R = 30 nm particle. The scattering and absorption efficiencies at the plasmon resonance maximum are plotted as a function of radius in Figure 1.3b, showing that the cross-over occurs at $R \approx 23$ nm. The peak in extinction (scattering + absorption) efficiency shown in Figure 1.3a explains why plasmonic metal particles are strongly colored. For Ag particles with $R > \lambda$, in contrast, the extinction is relatively flat across the near UV and visible spectrum (*cf.* Figure 1a. in Reference 10), resulting in the familiar metallic gray color of bulk Ag.

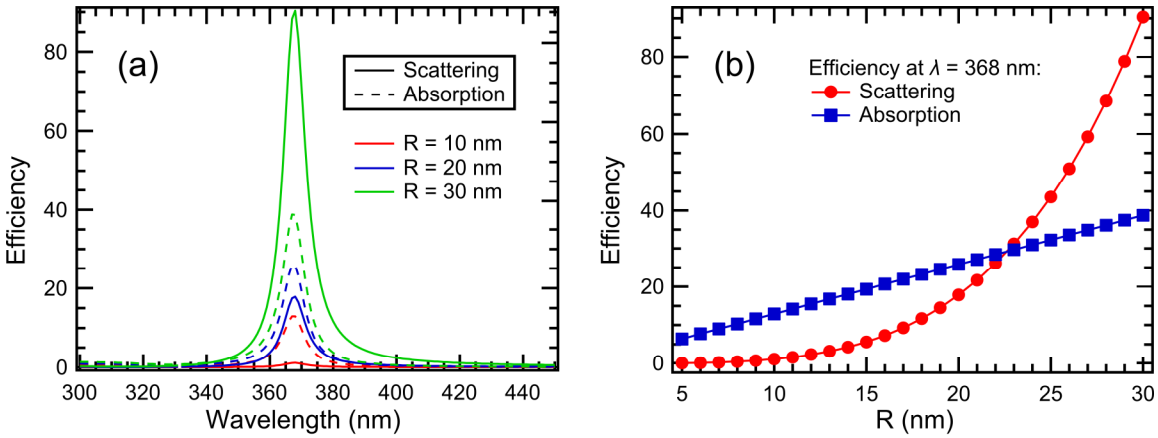

Figure 1.3 Dipolar plasmon scattering and absorption efficiency for spherical Ag particles calculated from Equation 1.25. (a) Efficiency for particles with radius R = 10, 20, and 30 nm. (b) Efficiency at the dipolar plasmon resonance maximum (λ = 368 nm) as a function of R.

For larger particles, higher-order plasmon multipoles can also be excited. These terms must be included in the solution for φ and the quantities derived from it. Quadrupolar modes are particularly significant, and quasistatic expressions for the quadrupole polarizability and cross-sections are available.[8] For higher order multipoles, the resonance condition approaches the frequency characteristic of the planar SP:[7]

$$\omega = \frac{\omega_p}{\sqrt{1+\varepsilon_m}} \qquad 1.26$$

Increasing particle size has additional consequences that cannot be treated in a quasistatic theory. Retardation effects arise for large particles due to a phase delay in the response at the two poles of the particle, shifting the plasmon resonance to lower energy. Radiative damping, a consequence of increased Rayleigh scattering, significantly broadens the plasmon resonance for large particles.

Mie theory only provides an exact analytical solution for spherical particles, although an extension of the theory has been developed for spheroids.[8] For particles of arbitrary size, however, computational approaches like the discrete dipole approximation (DDA), finite difference time domain (FDTD) method, and finite element method (FEM) can be used to calculate extinction spectra and local electric field intensities.[10] Spheroids and other non-spherically symmetric particles differ from the simple case discussed above because they can have more than one dipolar plasmon resonance, corresponding to electron oscillations along different axes of the particle.[8] Computational methods have proved valuable in identifying the components of the plasmon spectrum for particles of lower symmetry.

Where σ_{abs} is significant, excitation of a surface plasmon deposits energy in the metal particle. Dephasing of the coherent surface plasmon occurs on a 10 fs timescale.[15,16] The homogeneous surface plasmon linewidth is related to this dephasing time in the usual manner, with a shorter dephasing time resulting in a broader plasmon linewidth. After this loss of coherence, energy relaxation occurs within the particle in a series of stages. A similar relaxation process occurs even in cases where the coherent plasmon is not excited, as in ultrafast pump-probe experiments where the electrons are excited by an optical pulse. After plasmon decoherence, or after electron excitation by an optical pump pulse, the initially non-equilibrium electron distribution thermalizes by electron-electron scattering on a 100 fs timescale. At this stage, the electron distribution is in accordance with Fermi-Dirac statistics but characterized by a higher temperature than the temperature of the lattice. The excited electron gas subsequently cools by electron-phonon scattering, on a 1 ps timescale, raising the lattice temperature. In the

final stage of relaxation, the particle reaches thermal equilibrium with the environment through phonon-phonon scattering. This final equilibration occurs on a 100 ps timescale. In the case of a particle with $\sigma_{scat} \gg \sigma_{abs}$, most of the incident energy is reradiated to the far field via Rayleigh scattering, and less energy is deposited in the particle itself.[15,16]

1.2 Surface-Enhanced Raman Spectroscopy

The local electromagnetic field enhancement at the surface of plasmonic metal particles has a dramatic effect on the Raman scattering of nearby molecules: molecular Raman scattering cross-sections are enhanced by factors as large as 10^{14},[12] although some have argued that the upper limit is closer to 10^{12}.[17] The technique known as surface-enhanced Raman scattering (SERS) exploits this local electromagnetic field enhancement using plasmonic metal particles or roughened noble metal surfaces as a substrate for Raman spectroscopy. When a molecular electronic resonance overlaps spectrally with the plasmon resonance, the combined resonance Raman and SERS enhancements are large enough to allow the detection of single-molecule Raman scattering.[18] In the case of the dye molecule rhodamine 6G, the overall SERS cross-section is on the order of 10^{-13} – 10^{-14} cm^2 per molecule[19] or 10^{-15} cm^2 per mode,[20] a remarkable result when compared to typical Raman scattering cross-sections of 10^{-29} – 10^{-30} cm^2 per mode.[17,21] Since the first reports of SERS in the 1970s, significant progress has been made in understanding the details of the enhancement mechanism.[12,22-24] In the consensus model, SERS is the product of two enhancement mechanisms: an electromagnetic effect and a chemical effect. The former is responsible for the majority of the enhancement—up to 10^{10} or

perhaps 10^{11}—while the latter can provide an additional enhancement of approximately two or three orders of magnitude.[12]

The magnitude of the electromagnetic SERS effect reflects the fact that there are two stages of enhancement.[12] First, the incident light is concentrated near the particle surface by plasmon excitation and the electromagnetic field is enhanced by a factor *g*. This amplified incident light excites a Raman-active mode in the molecule, which then induces a corresponding oscillating dipole in the metal. The molecular Raman scattering at the Stokes-shifted frequency is thus magnified by an additional factor g' as the metal radiates to the far field. Neglecting complications due to the polarization of the light, the SERS enhancement *G* can be written as:

$$G = \left|\frac{\alpha_R}{\alpha_{R0}}\right| \left|gg'\right|^2 \qquad 1.27$$

where α_R is the polarizability of the molecule-metal system and α_{R0} is the polarizability of the free molecule. For low-frequency Raman modes, where the incident and scattered light are spectrally close, the factors *g* and g' will be similar and the overall Raman enhancement can be approximated as the field enhancement to the fourth power.[12] It is this magnification of both the incident and scattered light that translates a local field enhancement of 10 or 100 into a SERS enhancement many orders of magnitude larger.

Although this electromagnetic effect is the primary enhancement mechanism in SERS, there is evidence that other enhancement mechanisms with some degree of chemical specificity also contribute. One commonly cited example is the different SERS enhancements observed for CO and N_2; despite the similar molecular Raman scattering cross-sections, the SERS signal from CO is approximately 100-fold stronger.[14] Electrochemical SERS experiments provide confirmation of one type of chemical

enhancement mechanism, a photo-induced charge transfer between the metal and the molecule. For certain molecules adsorbed on SERS-active metal electrodes, the molecular Raman scattering intensity changes with the applied electrode potential. The direction of the charge transfer can be either metal-to-molecule or molecule-to-metal, depending on the relative positions of the molecular HOMO and LUMO levels and the metal Fermi level.[24] There may also be additional sources of enhancement involving ground state chemical interactions between molecule and metal, but these effects are not well understood.[22]

1.3 Plasmon-Enhanced Photochemistry and Photoelectrochemistry

Most photocatalysts are semiconductors, and metals are not typically thought to be photochemically active. Nonetheless, there have been reports of photochemical reactions in SERS experiments, where changes in the molecular Raman spectra are attributed to the photodestruction of the original species and the formation of degradation products with distinct Raman modes.[25-30] In some cases, the Raman signature of amorphous carbon appeared in the spectra. Early theoretical work by Nitzan and Brus found that molecular photochemistry could be enhanced in the near field of a plasmonic particle.[31,32] These studies considered two competing effects: an increase in molecular absorption due to the local electric field enhancement, favoring photochemistry, and Förster energy transfer from the excited molecule to the metal, competing with photochemistry of the molecular excited state. In the SERS studies where photodegradation was observed, however, the molecules did not absorb light at the incident laser wavelength. Instead, these reactions were attributed to charge-transfer

transitions between the metal and the molecule, which would occur at energies lower than the molecular HOMO-LUMO gap, followed by irreversible degradation of the molecular anion. As discussed in Chapter 1.1.2, photon absorption and plasmon decay in metal nanoparticles generates "hot" electrons and holes above and below the Fermi level respectively. In addition to SERS studies where photochemical reactions were observed, there is also evidence from high vacuum surface science studies[33-36] and from electrochemical studies[37,38] that these hot electrons and hot holes can mediate photochemical reactions of adsorbed molecules. Figure 1.4 illustrates the tunneling of a hot electron from a metal surface to an adsorbed molecule. Electron transfer can lead to vibrational excitation of the molecule, desorption, dissociation reactions, or other irreversible photochemical reactions.[35,36] The electron may return to the metal, possibly after having deposited some energy in the molecule, or it may be trapped on the molecule.

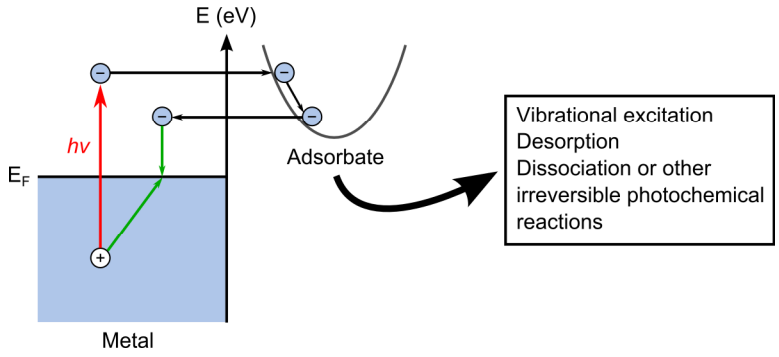

Figure 1.4 Schematic illustrating hot electron transfer from a photoexcited metal to an adsorbed molecule. The hot carriers in the metal relax to the Fermi level, as indicated by the green arrows.

Additional effects are possible in hybrid systems composed of plasmonic metal nanoparticles and semiconductors, either bulk or nanoscale. Several recent studies have demonstrated enhanced photochemistry of composite materials based on a semiconductor (commonly TiO_2) and Au or Ag nanoparticles. These reactions include the photooxidation of organic acids[39,40] and other small molecules,[41,42] the epoxidation of ethylene,[43] the photodegradation of dye molecules,[44-47] and the photoreduction of nitroaromatic compounds,[48] carbon dioxide,[49] and molecular oxygen.[50] There have also been numerous reports of improved performance upon addition of plasmonic metal nanoparticles to photoelectrochemical systems.[51-58] In many of these systems, questions remain about the detailed enhancement mechanism. The mechanisms proposed can be grouped broadly into four categories: i) improved interfacial charge-transfer kinetics due to the metal nanoparticle; ii) charging of the metal nanoparticles, leading to a shift in the semiconductor Fermi level to higher energies; iii) local electric field enhancement by the metal nanoparticle, concentrating light absorption by the semiconductor in a thin active area near the solution interface; and iv) direct transfer of photoexcited carriers from the metal to the semiconductor. (The four types of mechanisms are illustrated in Figure 1.5.) These effects are not mutually exclusive, and several might be operative in a single system.

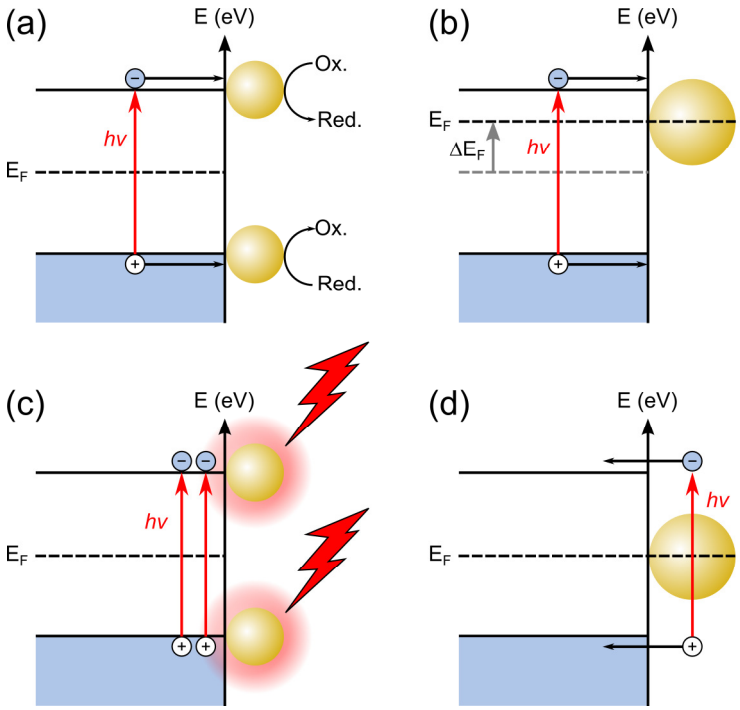

Figure 1.5 Enhancement mechanisms in metal nanoparticle-semiconductor photocatalytic and photoelectrochemical systems. (a) Improved interfacial charge-transfer kinetics due to the metal nanoparticle. (b) Charging of the metal nanoparticle and corresponding shift in the semiconductor Fermi level to higher energy. (c) Enhancement of incident light by the metal nanoparticle leading to increased absorption near the semiconductor-solution interface. (d) Direct transfer of photoexcited carriers from the metal to the semiconductor.

The first two effects do not rely on the plasmonic properties of noble metal nanoparticles. Metal nanoparticle-semiconductor co-catalyst systems display improved charge-transfer kinetics because the metal particle can lower the activation energy, and thus the overpotential, for certain types of chemical reactions (Figure 1.5a).[59] The second effect, metal nanoparticle charging, has been described in depth by Prashant Kamat and co-workers in a series of papers (Figure 1.5b).[51,52,58,60,61] Chandrasekharan and Kamat

reported a 3-fold increase in the photocurrent of a mesoscopic TiO_2 anode modified with Au nanoparticles, as well as an increase of approximately 150 mV in the magnitude of the open-circuit potential.[51] These effects were subsequently confirmed for TiO_2 films modified with Au, Pt, and Ir particles.[52] The increase in photocurrent was attributed to improved interfacial charge-transfer kinetics at the metal surface. The shift in open-circuit potential was understood as Fermi level equilibration between the semiconductor and the metal. It has been demonstrated that noble metal nanoparticles can accumulate a significant excess negative charge in solution, balanced by a corresponding positive charge on the solution side of the electrical double layer.[62-64] The Fermi levels of noble metals like Au and Ag lie below the conduction band edge of TiO_2. As a result, electrons excited across the TiO_2 band gap accumulate in the metal particle. In the presence of a reducing agent, like ethanol, to scavenge holes left in the TiO_2 valence band, the Fermi level of the metal-TiO_2 composite shifts to higher energies (or, equivalently, to more negative potentials) as an excess of electrons builds up in the system. Although some of this negative charge resides on the semiconductor, the metal has a higher capacitance and thus retains most of the excess electrons. Additional studies quantified this Fermi level shift for Au-TiO_2 composites.[60,61] Similar photoinduced charging of Ag-TiO_2 core-shell particles was also reported, with the excess electron density on the Ag core leading to a shift in the plasmon resonance to higher energy.[65]

Unlike these effects explored by Kamat and others, mechanisms iii) and iv) are dependent on the plasmonic properties of metal nanoparticles. Mechanism iii) is operative in systems where metal nanoparticles are deposited on the surface of semiconductor particles or films (Figure 1.5c). One significant factor in the overall

efficiency of a photocatalytic process is the recombination rate of photogenerated electron-hole pairs in the catalyst. Electrons and holes that recombine before they can travel to the surface and participate in a chemical reaction will lower the photocatalytic yield. Photons absorbed deep within the semiconductor produce electron-hole pairs that must travel further to react, while photons absorbed near the surface are more likely to participate in chemical reactions at the interface. Plasmonic metal nanoparticles, by concentrating the local electromagnetic field, increase light absorption by semiconductors in the vicinity of the particle—that is, near the surface of the semiconductor. This effect was invoked by Liu *et al.* to explain the enhancement in photocatalytic water splitting by anodic TiO_2 modified with Au nanoparticles[55] and by Ingram and Linic in similar experiments involving water splitting by composites of Au or Ag nanoparticles and nitrogen-doped TiO_2.[56]

The distinguishing feature of mechanism iv) is that light absorption occurs in the metal nanoparticle, not in the semiconductor (Figure 1.5d). In this model, the hot electrons generated by surface plasmon excitation of the metal are injected into the semiconductor conduction band, while the hole is scavenged by a reducing agent in the solution. Of the enhancement mechanisms discussed above, this one remains the most controversial. In 2005, Tian and Tatsuma reported a peak incident photon to current conversion efficiency (IPCE) of 26% for a mesoscopic TiO_2 film modified with Au nanoparticles under visible light excitation.[53] They proposed that hot electrons tunneled from the Au to the TiO_2, and that a Schottky barrier at the metal-semiconductor interface prevented back-transfer of the electron to empty states in the metal. Support for this model has come from ultrafast transient absorption studies conducted by Tachiya and

colleagues, where the plasmon resonance of Au nanoparticles was excited by a visible light pump pulse and the response of conduction electrons in the TiO_2 was monitored by an infrared probe pulse.[66,67] They found that electron injection into TiO_2 occurred on a timescale of approximately 50 fs with yields of 20 – 50% depending on TiO_2 particle size. Other groups have invoked this mechanism to explain the behavior of composite photocatalysts.[39,45] Nishijima *et al.* reported IPCEs of up to 8% for Au nanoparticle arrays fabricated on n-type single-crystal TiO_2 electrodes in a photoelectrochemical cell and attributed the photocurrent to direct injection of electrons from the metal into the TiO_2 conduction band.[57] Some researchers have failed to find evidence of this effect in their systems, however, including Subramanian *et al.*[52] and Liu *et al.*[55]

This mechanism is analogous to the sensitization of mesoscopic TiO_2 by an excited dye molecule in dye sensitized solar cells (DSSCs),[68-72] but there are significant differences between the two cases. In the DSSC, visible light is absorbed by dye molecules adsorbed on the semiconductor surface, promoting electrons to the first molecular excited state. These excited electrons have sufficient energy to tunnel into the TiO_2 conduction band on a femtosecond timescale, leaving the dye molecule with a residual positive charge. If the dye molecule is reduced by the redox couple in the electrolyte before back-transfer occurs from the TiO_2 conduction band, the excess electron remains in the TiO_2 and can be collected at the contact. Back-transfer from the TiO_2 is suppressed by several factors, including the large energetic gap between the conduction band edge and the ground electronic state of the dye molecule. Although back-transfer to the dye molecule is highly exergonic, the kinetics are slow because the reaction is in the inverted region predicted by Marcus theory.[73] As a result, the timescale

for dye regeneration by the redox couple, on the order of 10 ns, is significantly shorter than the microsecond to millisecond timescale for electron back-transfer.[68] In the case of a metal nanoparticle, however, empty electronic states in the metal are available at the energy of the semiconductor conduction band edge. The electron back-transfer rate from semiconductor to metal is thus expected to be high, and relaxation of the hot electron in the metal will occur on the 10 fs to 1 ps timescale discussed in Chapter 0.

This argument suggests that charge-transfer yields between a photoexcited metal nanoparticle and a semiconductor will be low unless back-transfer is suppressed by some mechanism. In the case of a bulk semiconductor, a Schottky barrier at the metal-semiconductor interface may play this role (Figure 1.6a). When a semiconductor and metal come into contact, charge flows across the interface until the Fermi levels on both sides of the junction are equal. If the Fermi level of the metal is initially lower than that of the semiconductor, electrons are transferred from the semiconductor to the metal. At equilibrium, the electron concentration in the semiconductor is lower near the interface. As a result, the conduction and valence bands bend upward in this region, which is known as the space charge region. The Schottky barrier height (Φ) in this situation is the energy difference between the metal Fermi level and the semiconductor conduction band edge.[2] If excited electrons from the metal have enough energy to surmount the Schottky barrier and enter the semiconductor, the electric field in the space charge region will sweep them away from the interface, suppressing back-transfer into the metal (Figure 1.6b). A similar phenomenon occurs when a semiconductor electrode comes into contact with an electrolyte solution.[74,75] A few recent studies have exploited Schottky barrier physics in solid state devices to collect hot carriers excited in plasmonic metal

nanoparticles. Knight *et al.* reported charge injection from Au nanoparticles into bulk *n*-type Si according to this mechanism, albeit with a quantum yield of only 0.01%.[76] Mubeen *et al.* reported sensitization of 200 nm thick TiO_2 by Au nanoparticles.[72] For nanoscale semiconductors, however, the situation is more complicated. Typical space charge region widths are on the order of 5 to 200 nm, depending on the doping level and the potential difference between the surface and the bulk of the semiconductor.[74] In semiconductor particles much smaller than this length, a significant space charge region will not form, and back-transfer of electrons to the metal may not be suppressed (Figure 1.6c).

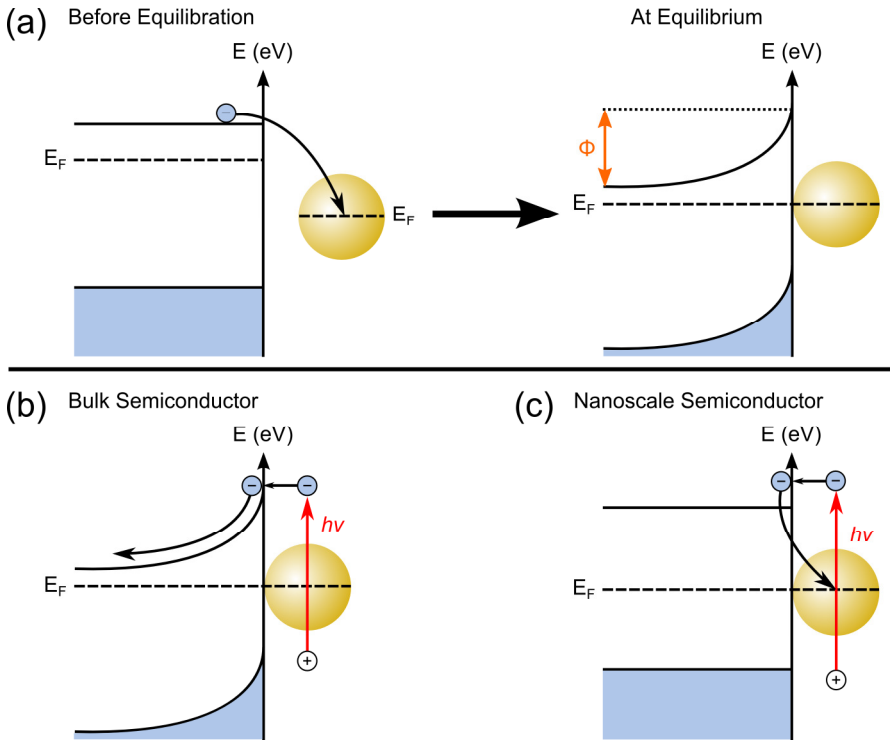

Figure 1.6 (a) Schottky barrier formation between a metal particle and a semiconductor. (b) Electron injection into a bulk semiconductor by a metal particle. The electron is swept away from the interface by band bending in the space charge region. (c) Electron injection into a nanoscale semiconductor by a metal particle. There is no space charge region to accelerate the electron away from the interface and thus the electron is more likely to return to the metal particle.

Insight into the mechanism of photocatalysis or the operation of a photoelectrochemical cell can be obtained by studying the action spectrum of a system. In an action spectrum, some measurement of the photoresponse of the system—the photocurrent, rate of photoproduct formation, or photoconductance, for example—is plotted against wavelength. Comparing this wavelength-dependent response to the absorption spectrum of the different components of the system can help determine which

material is responsible for light absorption or whether there are other sources of enhancement. If the plasmonic properties of metal nanoparticles play a role in the photoresponse of a system, the action spectrum would be expected to show some correspondence to the plasmon resonance spectrum. In one case, Chandrasekharan *et al.* found no changes in the profile of the photocurrent action spectrum of a nanostructured TiO_2 anode upon modification with Au nanoparticles. From this result, they concluded that light absorption by the Au nanoparticles did not contribute to charge separation in the photoelectrochemical cell.[51] Conversely, Nishijima *et al.* found good agreement between the IPCE action spectrum of a single-crystal TiO_2 anode modified with Au nanorods and the nanorod extinction spectrum, and they attributed the anode photoresponse to light absorption by the nanorods followed by injection of energetic electrons into TiO_2.[57]

1.4 Plasmon-Mediated Photooxidation of Citrate

This chapter will focus on a particular plasmon-mediated photochemical reaction, the photooxidation of citrate by Ag nanoparticles. In 2001, Chad Mirkin and colleagues reported a novel photoconversion reaction in which citrate photooxidation played a key role.[77] They observed that small spherical Ag nanoparticles (Ag seeds) were converted under low intensity visible illumination to larger triangular nanoplates, which they termed nanoprisms. Follow-up work by Jin *et al.*[78] and separate reports by Maillard *et al.*[79] and Callegari *et al.*[80] confirmed the essential features of this reaction. Light, the capping agent sodium citrate, and either oxygen or a source of Ag^+ were all required for nanoprism growth. Maillard *et al.* first proposed that citrate was acting both as a capping ligand and as a reducing agent for Ag^+ in solution. Other stabilizing ligands, like bis(*p*-

sulfonatophenyl) phenylphosphine dihydrate dipotassium salt (BSPP) or polyvinylpyrrolidone, were found not to be necessary for the photoconversion reaction.[81] These early studies also pointed to the role of excitation wavelength in controlling the size and shape of the resulting Ag nanoparticles. In a striking example of size control in a photochemical nanoparticle synthesis, Jin *et al.* showed that the nanoprism edge length could be gradually tuned from 40 to 120 nm as the primary excitation wavelength was varied from 450 to 750 nm.[78]

This unusual photoconversion reaction has been extensively studied in the decade since the original report, and a more detailed mechanism has been developed.[82-84] A photovoltage mechanism for the photoconversion reaction has been proposed by Redmond *et al.*[82] and Wu *et al.*[83] In this model, Ag seed particles in the colloid absorb incident light and photooxidize adsorbed citrate. Seed particles of different shapes have different plasmon resonance spectra, and thus some particles in the initial colloid absorb light more strongly at the excitation wavelength than will others. The rate of citrate photooxidation is higher for those particles that absorb light more strongly. As the seeds oxidize citrate, they develop a negative charge—or equivalently, a negative photovoltage—which is larger on particles with higher rates of citrate oxidation. Meanwhile, in the presence of oxygen, a small equilibrium concentration of Ag^+ builds up in solution as Ag seed particles are etched. Seed particles that have developed a negative photovoltage discharge excess electrons by reducing Ag^+ at their surface. As the reaction proceeds, some seed particles continue to reduce Ag^+ and grow at the expense of others in a quasi-Ostwald ripening process. This photovoltage mechanism for particle growth can also explain the wavelength-dependent control of particle size

reported by Jin *et al.*[78] The dominant plasmon resonance of nanoprisms, the in-plane dipolar mode, moves to longer wavelength with increasing nanoprism edge length. As nanoprisms in the colloid grow large enough that their plasmon resonance shifts to longer wavelength than the excitation light, they absorb less strongly and consequently their rate of citrate photooxidation slows. Particles in the colloid with plasmon modes at shorter wavelength than the excitation light continue to photooxidize citrate and reduce Ag^+ at a faster rate until they, too, grow out of resonance with the light. This self-limiting mechanism would narrow the size distribution of the nanoprism colloid and could explain the wavelength control demonstrated by Jin *et al.*[78]

As discussed in the previous section, the ability of Ag and Au nanoparticles to accumulate excess charge and maintain a cathodic polarization has been well established.[62] Redmond *et al.* took advantage of this fact to measure directly the negative photovoltage on Ag nanoparticles on an indium tin oxide (ITO) electrode in a photoelectrochemical cell.[82,85] Supporting the photovoltage model for nanoprism growth described above, this Ag nanoparticle-ITO electrode produced a negative photovoltage and an anodic (oxidation) photocurrent in the presence of citrate. Further studies by Wu *et al.* explored a similar system involving Au nanoparticles.[86] This chapter describes photoelectrochemical experiments aimed at understanding the mechanism of the plasmon-mediated photooxidation of citrate by Ag nanoparticle electrodes. We report the photocurrent and photovoltage action spectra of citrate photooxidation for three different types of Ag nanoparticles supported on ITO. Additionally we explore the role of the substrate in charge separation in this photoelectrochemical cell by measuring the response of Ag nanoparticles fabricated on fluorine tin oxide (FTO) and single-crystal *n*-

type TiO_2. In all cases we find similar action spectra and quantum yields for citrate photooxidation, with the quantum yields increasing at shorter wavelengths. We do not observe a correspondence between the citrate photooxidation quantum yield and the plasmon resonance of the Ag nanoparticles.

1.5 Experimental

1.5.1 Materials

Sodium borohydride (≥ 98.5%), poly(vinyl pyrrolidone) (average $M_W \sim 29{,}000$), and poly(allylamine hydrochloride) (average $M_W \sim 56{,}000$) were obtained from Aldrich. Silver nitrate (≥ 99.8%) (Riedel-de Haën), trisodium citrate dihydrate (≥ 99.5%), sodium hydroxide (≥ 97%), hydrogen peroxide (30 wt%) were purchased from Sigma-Aldrich. Potassium nitrate (≥ 99.999%) was supplied by Strem Chemicals. Deionized water (resistivity 17.8 – 18.2 MΩ·cm) was used to prepare solutions and in all cleaning procedures.

Indium tin oxide (ITO) with sheet resistance of 5 – 15 Ω/sq. was purchased from Delta Technologies, Ltd (CB-50IN). ITO with sheet resistance of 15 – 25 Ω/sq. was also obtained from Sigma-Aldrich. Fluorine tin oxide (FTO) with sheet resistance of 6 – 9 Ω/sq. was purchased from Pilkington (TEC-8). Single-crystal *n*-type TiO_2 substrates were provided by Bruce Parkinson (University of Wyoming).[87,88] A rutile (110) TiO_2 crystal with doping density on the order of 1×10^{20} electrons/cm^3 was used in this study.

1.5.2 Colloidal Nanoparticle Synthesis

Colloidal Ag nanoprisms were synthesized by a thermal method.[89] Briefly, 12.5 mL of 0.1 mM $AgNO_3$, 0.75 mL of 30 mM citrate, 0.75 mL of 0.7 mM PVP (average M_W ~ 29,000 g/mol), and 30 μL of H_2O_2 (30 wt%) were combined in a 50 mL Erlenmeyer flask and stirred vigorously. Then 100 μL of ice-cold 100 mM $NaBH_4$ was injected and the colloid was allowed to stir for 20 – 30 min until a series of color changes occurred.

Colloidal Ag nanospheres were synthesized following a modified Lee-Meisel procedure.[90] A solution of 18 mg $AgNO_3$ in 100 mL water was brought to a boil in a 100 mL round-bottom flask equipped with a condenser, then 2 mL of a 2 wt% solution of citrate was added. The solution refluxed for an additional 2 h.

1.5.3 Nanoparticle Electrode Fabrication

Indium tin oxide (ITO) slides of sheet resistance 5 – 15 Ω/sq. (Delta Technologies, Ltd.) were cleaned by sonication in ethanol and water for 15 min each and used as a substrate for the nanoparticle electrodes. In control experiments, ITO obtained from Sigma-Aldrich (15 – 25 Ω/sq.) and fluorine tin oxide (FTO) of sheet resistance 6 – 9 Ω/sq. (Pilkington TEC-8) were also used. The single-crystal *n*-TiO_2 electrode was cleaned after each experiment in several steps. First the electrode was wiped with a Kimwipe or lens tissue wetted with ethanol. The electrode was then sonicated in ethanol followed by water and dried with N_2 gas. To remove any residual Ag, the electrode was gently polished with 0.05 μm alumina polish and polishing pads (Bioanalytical Systems, Inc.). Finally, the electrode was rinsed thoroughly with water from a wash bottle and sonicated for 5 min to remove alumina particles.

To form quasi-spherical Ag nanoparticles, a thin Ag film (nominal thickness 2 – 4 nm) was deposited on the ITO substrate by thermal (Edwards BOC/Auto 306) or e-beam (Semicore SC2000) evaporation, followed by annealing in air at 120 °C for 30 min.

Colloidal Ag nanoparticles were deposited on ITO by immersion. First, the ITO surface was coated with a thin film of poly(allylamine hydrochloride) (PAH) to increase the density of adsorbed Ag particles.[91] To deposit the PAH film, a clean ITO slide was soaked for 30 min in 1 M KOH and then immersed for 30 min in an aqueous 0.2 mg/mL PAH solution. After rinsing with water, the slide was immersed in the Ag nanoparticle colloid overnight.

1.5.4 Characterization

Ag nanoparticle colloids and electrodes were imaged by TEM (JEOL JEM-100CX) and SEM (Hitachi 4700) respectively. Evaporated Ag nanoparticle electrodes were characterized by XPS (PHI 5500 ESCA (XPS)/ISS). UV-vis spectroscopy (Hewlett-Packard 8453) was used to record the spectra of nanoparticle colloids and electrodes.

The doping density and flat-band potential of the *n*-TiO_2 electrode were determined by Mott-Schottky analysis using a PARSTAT 2263 potentiostat. A small oscillating AC voltage (10 mV, 500 Hz) was applied to the working electrode and the impedance was measured as a function of applied DC voltage. Measurements were performed in a three-electrode cell with a Pt wire counter electrode and an Ag/AgCl reference electrode (Bioanalytical Systems, Inc.). The electrolyte was 100 mM $NaClO_4$ or 500 μM trisodium citrate/100 mM KNO_3, sparged with N_2 or Ar gas for 20 minutes

before use. The impedance is a complex quantity, $Z = Z' + iZ''$, and the capacitance C is related to the imaginary part, Z'', by:

$$C = \frac{1}{2\pi\nu Z''} \tag{1.28}$$

where v is the frequency of the AC voltage.[74] Under depletion conditions for an n-type semiconductor, when the electron density is lower in the space charge region than in the bulk of the material, the capacitance of the space charge region is much smaller than the capacitance of the Helmholtz double layer on the solution side of the interface. In this case, the Helmholtz capacitance can be neglected and the measured electrode capacitance can be taken as the capacitance of the space charge region alone. The doping density can be determined from the Mott-Schottky equation:

$$\frac{1}{C_{sc}^2} = \frac{2}{\varepsilon\varepsilon_0 ne}(E - E_{FB} - \frac{k_B T}{e}) \tag{1.29}$$

where C_{sc} is the capacitance per unit area of the TiO_2 space charge region in F/cm^2, k_B is the Boltzmann constant in J/K, T is temperature, ε is the TiO_2 dielectric constant, ε_0 is the vacuum permittivity in units of F/cm, n is the carrier density in electrons/cm^3, e is the electron charge in coulombs, E is the applied electrode potential, and E_{FB} is the flat-band potential.[75] The flat-band potential can be determined from the x-intercept of the line obtained when $1/C_{sc}^2$ is plotted against E. The exposed area of the TiO_2 electrode was approximately 0.12 cm^2 and the value $\varepsilon = 110$ was used for the TiO_2 dielectric constant. Measurements were also performed at two additional frequencies, 200 Hz and 1 kHz.

1.5.5 Photoelectrochemical Measurements

The evaporated or colloidal Ag nanoparticle electrode served as the working electrode in a 3-electrode photoelectrochemical cell, with a Pt wire counter electrode and

an Au wire quasi-reference electrode. Before electrochemical measurements, the electrode is "ripened" by immersion in the electrolyte solution for at least 20 min during N_2 or Ar purging. The standard electrolyte contains 500 μM trisodium citrate and 100 mM KNO_3. Electrolyte solutions were bubbled with N_2 or Ar for at least 20 min prior to use, and Ar gas was bubbled slowly through the electrolyte during electrochemical measurements.

A 300 W tungsten halogen lamp was used as the light source for photoelectrochemical measurements. Interference filters (transmission FWHM = 10 nm) and neutral density filters were used to select the excitation wavelength and the light intensity. The power was measured with a Coherent LM-2 VIS power meter (active area = 0.5 cm^2) and converted to irradiance. The light spot illuminated an area of approximately 1.44 cm^2 on the ITO working electrode, although a somewhat larger area of the electrode was in contact with the electrolyte solution. The counter and reference electrodes were shielded from direct light.

Two types of photoelectrochemical measurements were performed using a PARSTAT 2263 potentiostat. The photovoltage was measured under open-circuit conditions, and was calculated as $V_{OC,\,light} - V_{OC,\,dark}$. Photovoltages were typically measured in cycles starting at the highest wavelength to be used and moving to lower wavelengths. To account for the small positive shift usually seen in $V_{OC,dark}$ after each cycle, the photovoltage was calculated in two ways: using the same value of V_{dark} for each wavelength point in a cycle (shown as circles in the photovoltage graphs below) or by using a linear extrapolation of the potential shift to calculate a "true" V_{dark} at each wavelength point (shown as squares). Photocurrents were measured in

chronoamperometric mode with the potential held at $V_{OC,dark}$. Photocurrents were calculated by taking the average of $I_{light} - I_{dark}$ over three on/off cycles of 10 s each. The potentiostat's internal 5.00 Hz filter was applied during current measurements to eliminate high-frequency noise. Unless otherwise stated, neutral density filters were used to equalize the incident photon flux at each wavelength for all photovoltage and photocurrent measurements. For *n*-TiO_2 electrodes, the photocurrent was typically calculated by taking the average of $I_{light} - I_{dark}$ over two on/off cycles, with the light on for 30 s and off for 20 s. The photocurrent was measured at three different light intensities for each wavelength and the quantum yield was calculated from a linear fit to the photocurrent vs. irradiance plot.

1.6 Results

1.6.1 Nanoparticle Electrodes Characterization

Ag nanoparticles fabricated on ITO by evaporation and annealing were quasi-spherical with an average radius of 5 – 10 nm and a particle density of approximately 9.7 $\times 10^2$ particles/μm^2 (Figure 1.7d). The electrode UV-vis spectrum shows a primary peak at 495 nm from the LSPR absorbance of the particles (Figure 1.7a). The peak is red-shifted from the expected position for spherical Ag nanoparticles in air due to particle-particle interactions and the higher dielectric constant of the ITO.[8,92] When the electrode is immersed in the electrolyte, the plasmon peak red-shifts by about 10 nm. XPS measurements indicate little change in the oxidation state of the Ag after annealing in air (Figure 1.8). On FTO, the evaporated Ag nanoparticles are 10 – 15 nm in radius, roughly

2 – 3 times larger than the average particle size on ITO (Figure 1.9b). The particle density on FTO, approximately 3.1×10^2 particles/μm^2 (not accounting for the FTO surface roughness), is about 3 times lower.

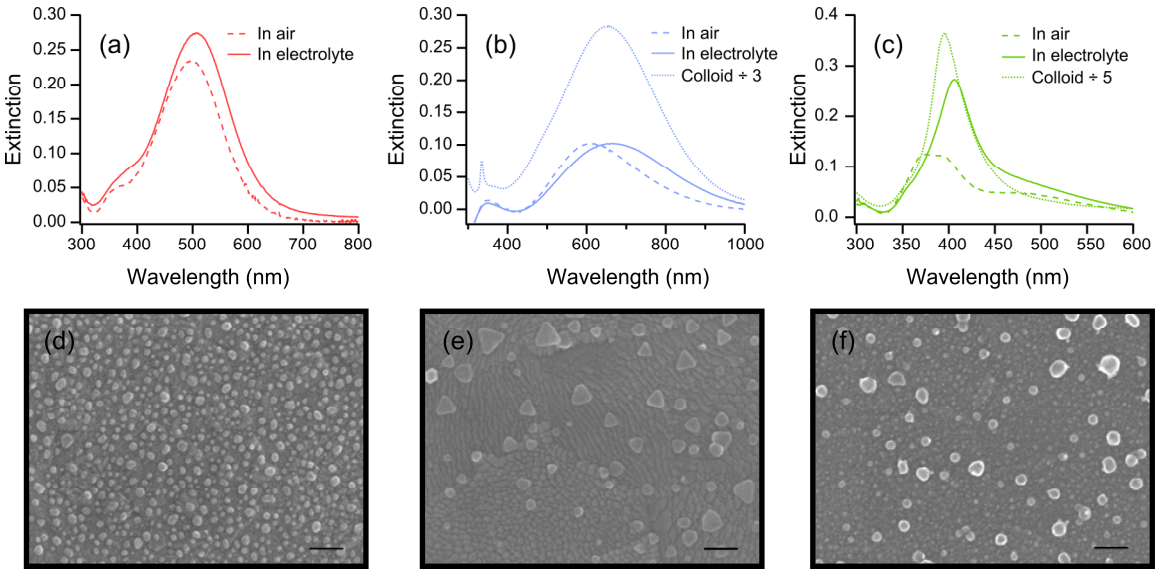

Figure 1.7 UV-vis extinction spectra (a – c) and SEM images (d – f) of typical evaporated Ag nanoparticle, colloidal Ag nanoprism, and colloidal Ag nanosphere electrodes. The electrodes were immersed in the 100 mM KNO_3/500 μM electrolyte solution when the spectra were recored. The dashed lines show the extinction spectrum of the dry electrode in air. The dotted lines in (b) and (c) show the extinction spectra of the nanoparticle colloids before use (divided by 3 and 5 respectively). All scale bars are 100 nm.

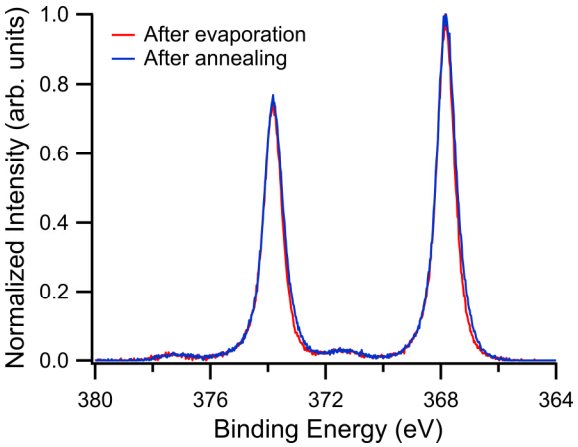

Figure 1.8 Comparison of the Ag 3d peaks of thermally evaporated Ag nanoparticle electrodes as-deposited (red) and annealed (blue) for 30 min at 120 °C in air. XPS spectra were recorded using Al Kα radiation (1486.6 eV) at a pass energy of 23.50 eV and 0.025 eV per step.

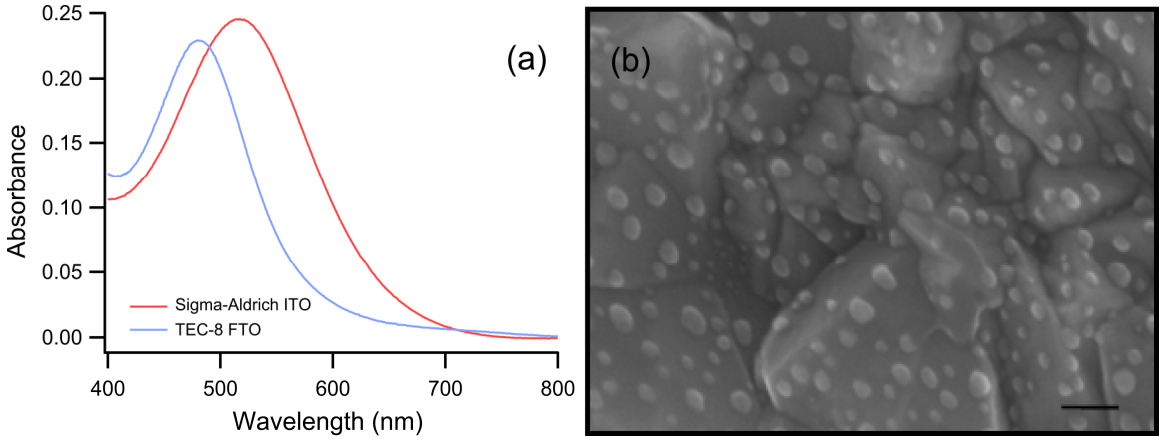

Figure 1.9 (a) UV-vis extinction spectra of evaporated Ag nanoparticles on Sigma-Aldrich ITO (15 – 25 Ω/sq.) (red) and Pilkington TEC-8 FTO (6 – 9 Ω/sq.) (blue). (b) SEM image of the FTO electrode showing the rougher surface of FTO and the larger and more widely dispersed Ag nanoparticles. The scale bar in (b) is 100 nm.

Colloidal Ag nanoprisms were larger, with edge lengths ranging from 30 – 70 nm and thickness on the order of 10 nm (Figure 1.7e). The particle density of the colloidal Ag nanoprism electrode was approximately 1.0×10^2 particles/μm^2, smaller than that of the evaporated particle electrode. The anisotropic Ag nanoprisms support both in-plane and out-of-plane dipolar and quadrupolar plasmon modes, which have been previously assigned.[77] The plasmon peaks are less distinct for the nanoprisms on ITO, but the in-plane dipole resonance can still be observed at 610 nm in air, or 665 nm in the electrolyte (Figure 1.7b).

The Ag colloid synthesized by reflux in citrate was dominated by quasi-spherical particles, with an average radius of 10 – 20 nm, although some rods and other shapes were also observed (Figure 1.7f). The electrode particle density, approximately 1.3×10^2 particles/μm^2, is low enough that the particles do not couple strongly and the plasmon peak measured in the electrolyte solution, at 405 nm, is closer to the position expected for an isolated spherical Ag particle (Figure 1.7c).

Figure 1.10 shows the Mott-Schottky plot obtained for a bare TiO_2 electrode in 500 μM trisodium citrate/100 mM KNO_3 electrolyte solution. A linear fit to the data is also plotted. A doping density of 8.1×10^{19} cm^{-3} and flat-band potential of − 0.909 V vs. Ag/AgCl can be calculated from the linear fit using Equation 1.29. Measurements at 200 Hz and 1 kHz gave similar results, with values for the doping density within 5 – 10% of the values determined at 500 Hz. The flat-band potential was more positive by approximately 40 mV at 200 Hz and more negative by approximately 10 mV at 1 kHz. In the 100 mM $NaClO_4$ electrolyte the doping density measured at 500 Hz was 5 – 10% lower and the flat-band potential was more positive by approximately 60 mV.

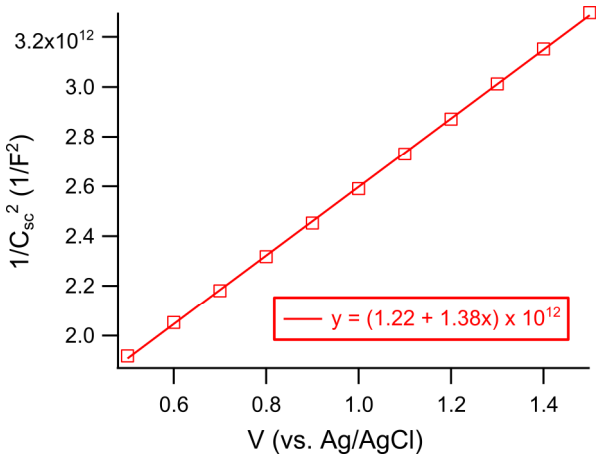

Figure 1.10 Mott-Schottky plot for single-crystal *n*-TiO_2 in 500 μM trisodium citrate/100 mM KNO_3 electrolyte solution and ν = 500 Hz.

1.6.2 Evaporated Ag Nanoparticle Electrode

Figure 1.11a shows the photocurrent response of an evaporated Ag nanoparticle electrode under irradiation at 500 nm in solutions containing 500 μM citrate and 500 μM tricarballylate. As previously reported, there is a reproducible anodic photocurrent of approximately 50 nA/cm^2 in the presence of citrate. The photocurrent is on the order of 1.5 nA/cm^2 in the tricarballylate solution, comparable to the value measured in 100 mM KNO_3 alone. The change in the electrode open-circuit potential under the same conditions is shown in Figure 1.11b. In the presence of citrate, the open-circuit potential shifts − 105 mV on irradiation. The photovoltage in tricarballylate is roughly − 2.5 mV, and there is almost no response when only the supporting electrolyte, KNO_3, is present.

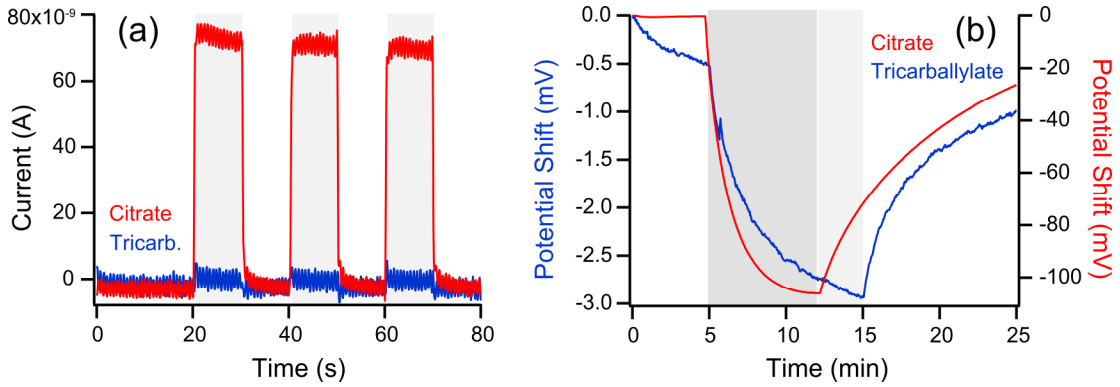

Figure 1.11 Current vs. time (a) and open-circuit potential vs. time (b) of an evaporated Ag nanoparticle electrode under irradiation at 500 nm (irradiance = 3.5 mW/cm^2). The electrolyte contained 100 mM KNO_3 and either 500 μM sodium citrate (red) or sodium tricarballylate (blue). The shaded rectangles indicate when the light was on.

The dependence of both photocurrent and photovoltage on light intensity was previously investigated for an evaporated Ag nanoparticle electrode in the presence of citrate.[85] The photocurrent was found to be linear with light intensity, suggesting that the photooxidation of citrate is a one-photon process. From the slope of the photocurrent vs. irradiance curve (Figure 1.12a), a quantum yield at 500 nm of 3.8×10^{-5} e^-/incident photon can be calculated. Taking into account the absorption of the electrode when immersed in the electrolyte solution, this value translates to a quantum yield of 1.1×10^{-4} e^-/absorbed photon, in good agreement with the previous report. As shown in Figure 1.12b, the photovoltage magnitude is found to increase linearly with the logarithm of the light intensity. This behavior is a consequence of the linear relationship between photocurrent and light intensity and can be derived from the Butler-Volmer equation for electrode kinetics.

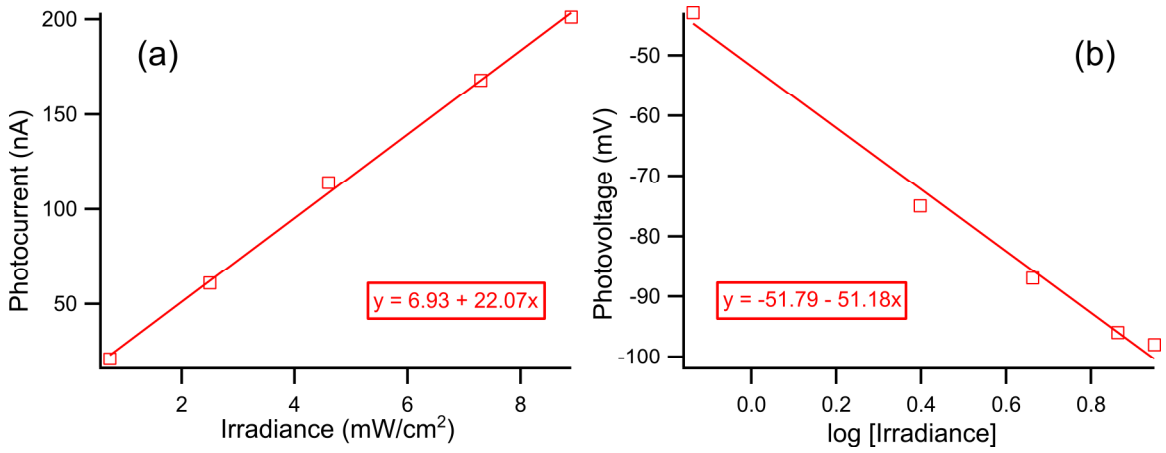

Figure 1.12 Photocurrent vs. irradiance (a) and photovoltage vs. log [irradiance] (b) of an evaporated Ag nanoparticle electrode under irradiation at 500 nm. Linear fits to the data are also plotted.

The photocurrent action spectrum for an evaporated Ag nanoparticle electrode is shown in Figure 1.13a. The electrode absorbance, measured in the electrolyte solution to account for a slight red-shift, in the corresponding wavelength range is also plotted. The photocurrent increases by approximately 25-fold going from 650 nm to 460 nm, without any sign of saturation. Notably, the photocurrent does not appear to track the electrode plasmon resonance, which peaks near 500 nm. The photovoltage magnitude, Figure 1.13b, also increases monotonically with decreasing wavelength. In contrast to the photocurrent, however, it does not rise as steeply below 560 nm.

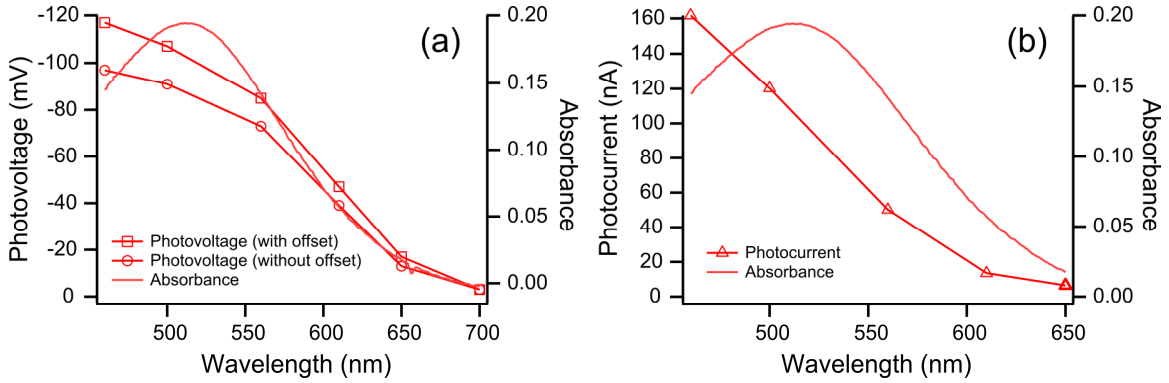

Figure 1.13 Photocurrent action spectrum (a) and photovoltage action spectrum (b) of an evaporated Ag nanoparticle electrode. The electrode UV-vis spectrum is plotted against the right axis. The photon flux at each wavelength was normalized to approximately 1.1 $\times 10^{16}$ photons/cm^2·s. In (b) the photovoltage is calculated with (squares) or without (circles) a linear offset to account for a shift in the open-circuit potential before and after the scan, as described in Chapter 1.5.5.

1.6.3 Colloidal Ag Nanoparticle Electrodes

The photovoltage action spectra of the colloidal Ag nanoprism and nanosphere electrodes are shown in Figure 1.14a and b respectively. The maximum photovoltage for the colloidal nanoparticle electrodes is weaker by a factor of two to three in comparison to the evaporated nanoparticle electrode, but the spectral response is similar. For both electrodes, despite their different absorbance spectra, the photovoltage rises with decreasing wavelength without any sign of leveling off. Like the photovoltage, the photocurrent measured with these electrodes is lower, on the order of 5 – 10 nA/cm^2 at most under typical experimental conditions. We note that the photocurrent and photovoltage depend on light intensity in the expected manner, as discussed above.

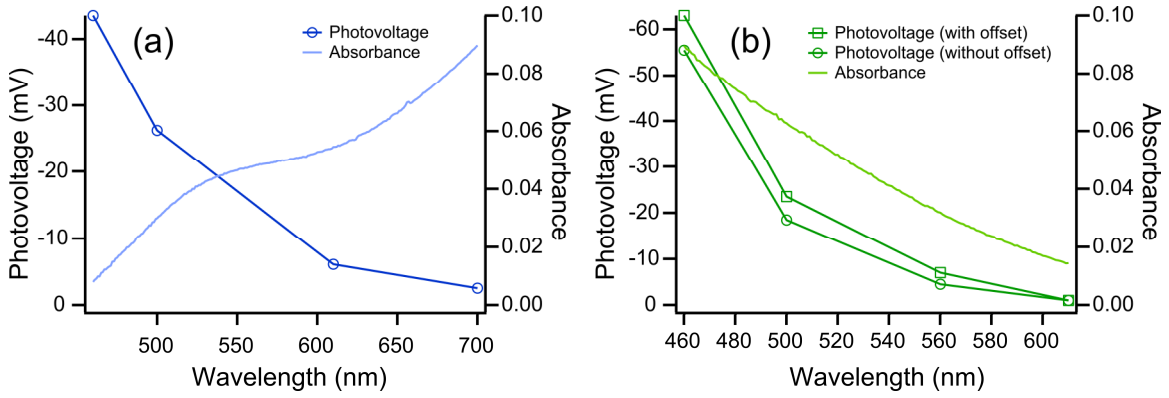

Figure 1.14 Photovoltage action spectra of a colloidal Ag nanoprism electrode (a) and a colloidal Ag nanosphere electrode (b). The electrode UV-vis spectrum is plotted against the right axis. The photon flux at each wavelength was normalized to approximately 1.2 × 10^{16} photons/cm^2·s. In (b) the photovoltage is calculated with (squares) or without (circles) a linear offset to account for a shift in the open-circuit potential before and after the scan, as described in Chapter 1.5.5.

1.6.4 Substrate Effects

Several control experiments were conducted to assess the effect of the ITO substrate on the Ag nanoparticle electrode photoresponse. First, the photoresponse of a bare ITO substrate was measured in the presence of citrate. Although an anodic photocurrent was observed at lower wavelengths, it was extremely weak; at 460 nm, the shortest wavelength used in this study, the photocurrent was less than 1 nA/cm^2 (Figure 1.15). Further, the photocurrent is essentially the same in the presence or absence of citrate. The photovoltage response of the bare substrate was also weak. Figure 1.16 shows the open-circuit potential vs. time measured for a bare ITO electrode under irradiation at 460 nm and 500 nm (curve *i*). After 20 min irradiation, the potential has

dropped by approximately 13.5 mV without reaching a steady-state value. When 5 μM $AgNO_3$ is added to the electrolyte solution, however, the system reaches a steady-state photovoltage of 14 mV (curve *ii*).

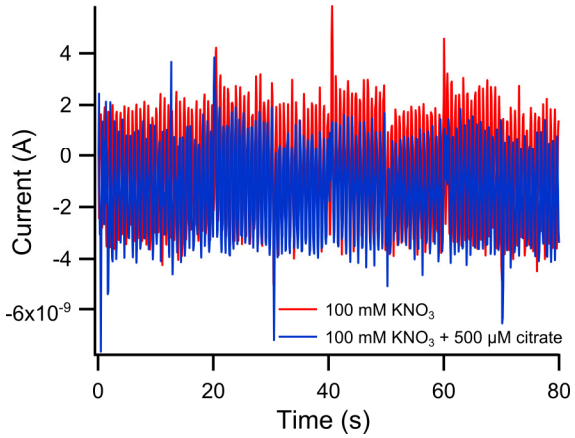

Figure 1.15 Current vs. time of unmodified ITO electrodes (Delta Technologies, 5 – 15 Ω/sq.) under irradiation at 460 nm (irradiance = approximately 6.7 mW/cm^2) in an electrolyte solution containing 100 mM KNO_3 and either 0 μM (red) or 500 μM sodium citrate (blue).

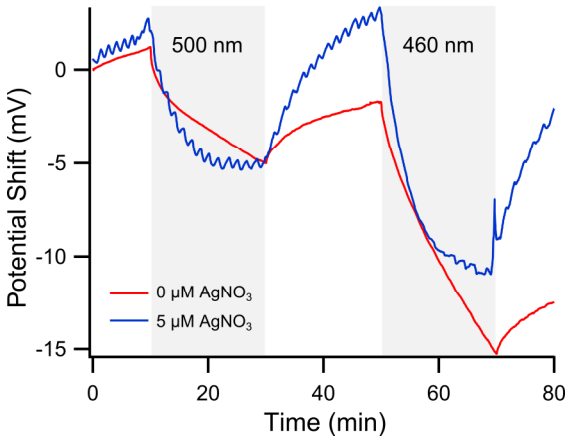

Figure 1.16 Shift from dark open-circuit potential of an unmodified ITO electrode (Delta Technologies, 5 – 15 Ω/sq.) in an electrolyte solution containing 100 mM KNO_3, 500 μM sodium citrate, and either 0 μM (red) or 5 μM $AgNO_3$ (blue). Irradiation was at 500 nm (irradiance approximately 6.7 mW/cm^2) and 460 nm (irradiance approximately 11.5 mW/cm^2) as indicated.

For additional confirmation that the measured photoresponse was independent of the substrate used, photocurrent and photovoltage action spectra were obtained for evaporated Ag nanoparticles fabricated on ITO supplied by Sigma-Aldrich and on TEC-8 FTO. The Ag nanoparticle photocurrent and photovoltage action spectra are similar for particles on the different substrates (Figure 1.17a and b), although the nanoparticle plasmon resonance is blue-shifted on FTO (Figure 1.9a) and this is reflected in the spectral photoresponse. The quantum yield per absorbed photon is essentially the same on the two ITO substrates, although it is lower by a factor of two on FTO.

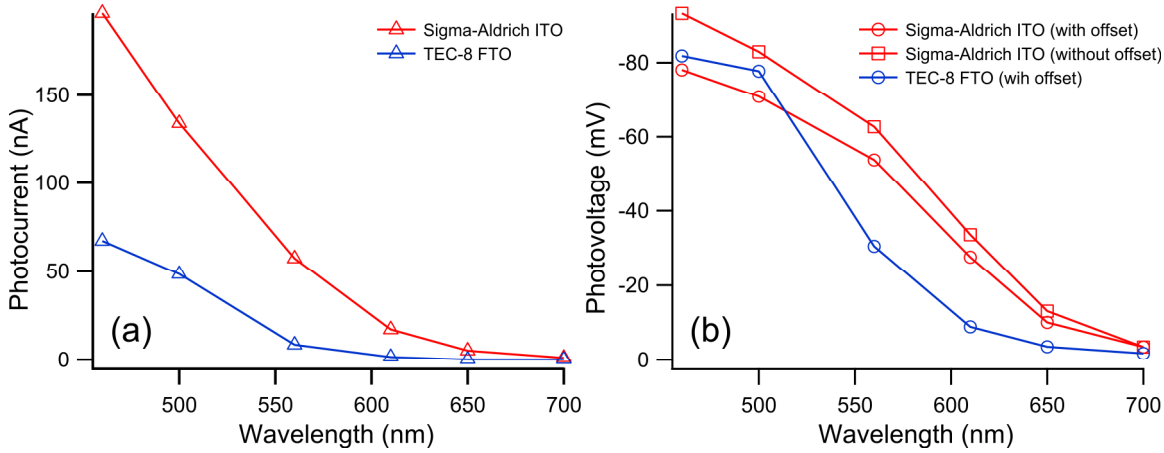

Figure 1.17 (a) Photocurrent action spectrum of evaporated Ag nanoparticle electrodes on Sigma-Aldrich ITO (red) and Pilkington TEC-8 FTO (blue). (b) Photovoltage action spectrum calculated with (squares) or without (circles) a linear offset to account for a shift in the open-circuit potential before and after the scan, as described in Chapter 1.5.5. The photon flux at each wavelength was normalized to approximately $1.1 - 1.2 \times 10^{16}$ photons/cm^2·s.

Finally, the photoresponse was measured for evaporated Ag nanoparticles on a single-crystal *n*-TiO_2 electrode. Figure 1.18a shows a typical photocurrent trace at a wavelength of 500 nm and irradiance of 6.8 mW/cm^2. We observe a consistent decay in the photocurrent at the start of each illumination cycle. The photocurrent approaches a steady-state value after approximately 30 s. This transient decay has been observed in other nanoparticle-TiO_2 systems and has been attributed to charging of an organic surfactant layer[52] or to the release of trapped charge at the TiO_2 surface.[55] Although the photocurrent magnitude in Figure 1.18a is low, it should be noted that the electrode area is approximately 12-fold smaller than the illuminated area of the Ag nanoparticle-ITO electrodes. The photocurrent action spectrum for the same Ag nanoparticle-TiO_2

electrode is plotted in Figure 1.18b. The spectral profile of the Ag nanoparticle response on the TiO_2 substrate is similar to the response on ITO and FTO, with an increase in photocurrent at short wavelengths. The quantum yield at 500 nm, approximately 1.7×10^{-5} e^-/incident photon, is the same order of magnitude as the value measured for the evaporated Ag nanoparticle-ITO electrode. We observed significant variability in the photoresponse of the Ag-nanoparticle TiO_2 electrodes, with the quantum yield per incident photon an order of magnitude smaller in some cases. The heavily-doped TiO_2 crystal is dark blue in color due to the absorption of Ti^{3+} ions produced in the doping process.[60] For this reason it was not possible to measure the UV-vis absorbance spectrum of the nanoparticles deposited on TiO_2 or to calculate the quantum yield per absorbed photon. Photovoltage measurements for Ag nanoparticle-TiO_2 electrodes were not very reproducible and the value of $V_{OC, dark}$ was somewhat unstable. Preliminary measurements, however, indicated that the Ag nanoparticle-TiO_2 electrode photovoltage response was weaker than that of the evaporated Ag nanoparticle-ITO electrode.

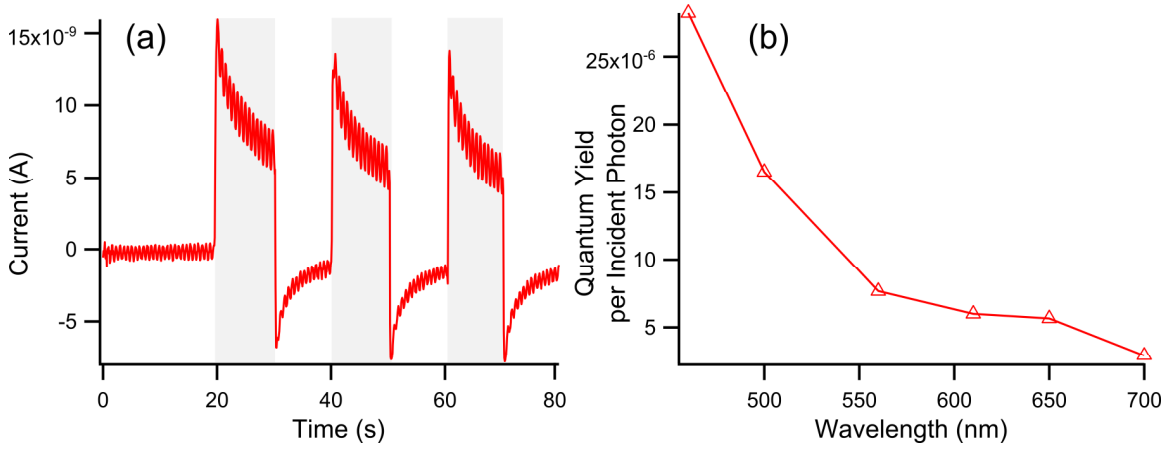

Figure 1.18 (a) Current vs. time of an evaporated Ag nanoparticle-TiO_2 electrode under irradiation at 500 nm (irradiance = 6.8 mW/cm^2) in a 500 μM sodium citrate/100 mM KNO_3 electrolyte solution. The shaded rectangles indicate when the light was on. (b) Quantum yield action spectrum for the same electrode.

1.7 Discussion

1.7.1 Citrate Photooxidation

As previously proposed by our group and others, adsorbed citrate is photooxidized by Ag nanoparticles excited at low light intensities with visible light.[79,82-84] The oxidation and resultant decarboxylation of organic acids is known in electrochemistry as the Kolbe reaction.[93] The Kolbe reaction can proceed as a one-electron or two-electron oxidation, but the first steps are the same:

$$\begin{aligned} \text{R-CO}_2^- &\rightarrow \text{R-CO}_2^{\bullet} + e^- \\ \text{R-CO}_2^{\bullet} &\rightarrow \text{R}^{\bullet} + \text{CO}_2 \end{aligned} \qquad 1.30$$

When the reaction follows the one-electron pathway, the radical species dimerizes to give the product R_2:

$$2R^{\bullet} \rightarrow R_2 \qquad 1.31$$

In the two-electron pathway, a second oxidation step occurs, forming a carbocation; nucleophilic attack yields the product R−Nu:

$$\begin{aligned} R^{\bullet} &\rightarrow R^{+} + e^{-} \\ R^{+} + Nu^{-} &\rightarrow R\text{-}Nu \end{aligned} \qquad 1.32$$

Work by Kraeutler and Bard has established that the Kolbe reaction can be carried out using *n*-type TiO_2 single crystals and powders as photocatalysts.[94-96] In some cases, this photo-Kolbe reaction yields a different mix of products from the purely electrochemical oxidation. This work identified the importance of the irreversibility of the Kolbe decarboxylation step (Equation 1.30) in preventing back-transfer of the electron to the semiconductor.

Our group has proposed that citrate photooxidation occurs as a two-electron photo-Kolbe reaction with the hydroxyl group acting as an internal nucleophile. In this mechanism, citrate donates two electrons to the Ag particle and decomposes to 1,3-acetonedicarboxylate and carbon dioxide according to the reaction:

$$\text{Citrate} \rightarrow \text{1,3-Acetonedicarboxylate} + CO_2 + H^{+} + 2e^{-} \qquad 1.33$$

The hydroxyl group oxygen donates a lone pair of electrons to the central carbon to form a carbon-oxygen double bond, accompanied by the heterolytic cleavage of the carbon-carbon bond between the central carbon and the short-armed carboxylate group. The proposed mechanism is illustrated in Figure 1.19a. In support of this picture, Wu *et al.* used ^1H nuclear magnetic resonance (NMR) spectroscopy to confirm that citrate is consumed during the course of the photochemical conversion of spherical Ag nanoparticles to large Ag nanoprisms.[83] Xue *et al.* reached the same conclusion and also

identified the decomposition products of citrate, 1,3-acetonedicarboxylate and acetoacetate, by ^{1}H NMR.[84] We note that although citrate can be oxidized by Ag^{+} at elevated temperatures, the reaction is extremely slow at room temperature.

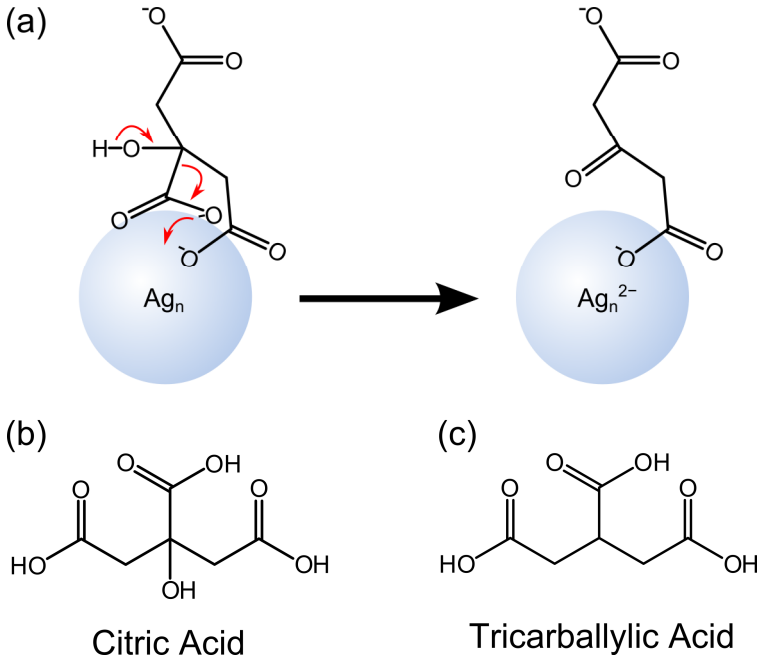

Figure 1.19 (a) Proposed photooxidation mechanism of citrate adsorbed on Ag. (b) Molecular structure of citric acid. (c) Molecular structure of tricarballylic acid.

Citrate itself does not absorb visible light, but Ag nanoparticles have an enhanced absorption (and scattering) cross-section at visible wavelengths due to their localized surface plasmon resonance. As previously noted, the coherent plasmon is not excited by our narrow-band irradiation; instead, light absorption generates non-thermalized ("hot") electrons and holes in the Ag particles. The excited metallic carriers can transiently localize on chemisorbed molecules and then return to the metal; in some cases this reversible interaction can cause a significant broadening of the plasmon linewidth.[97] If

the transient localization leads to an irreversible chemical reaction, however, the excited carrier can be trapped on the molecule.[23] In the case of citrate chemisorbed on Ag, transient localization of a hot hole on the citrate molecule initiates the irreversible decarboxylation process discussed above (Figure 1.20a).

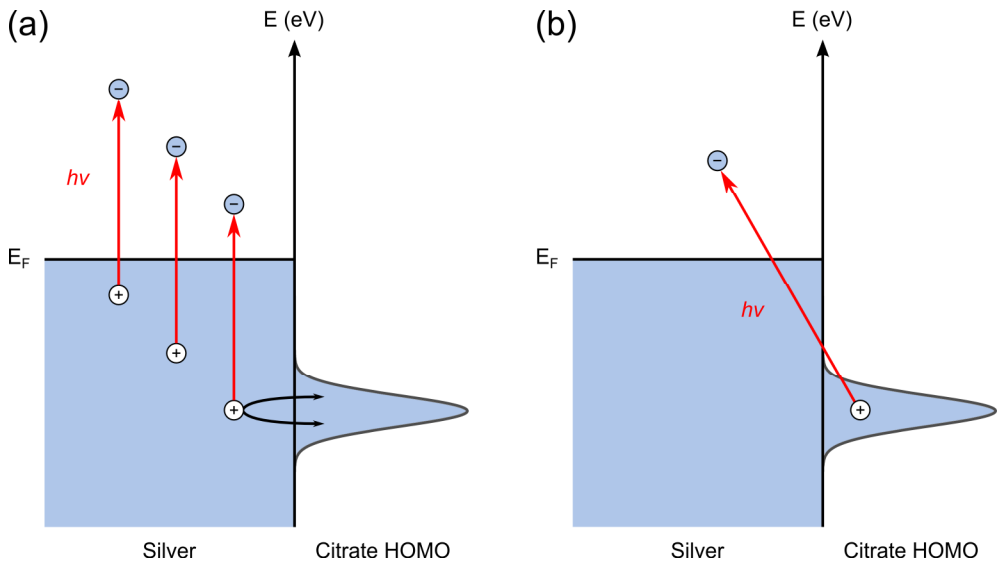

Figure 1.20 Models for citrate photooxidation by Ag nanoparticles. (a) Hot hole transfer to citrate. (b) Direct photoinduced molecule-to-metal charge transfer.

In this study, we have demonstrated that the photocurrent and photovoltage measured for an Ag nanoparticle electrode in the presence of tricarballylate are at least an order of magnitude lower than in the presence of citrate. (The structures of citric acid and tricarballylic acid are shown for comparison in Figure 1.19b and c.) Experimental[90] and theoretical[98] studies have found that citrate binds to the silver surface through its two methylene carboxylate groups, suggesting that tricarballylate is capable of adsorbing in the same manner. Nonetheless, tricarballylate lacks an α-hydroxyl group and would be unable to decarboxylate following the mechanism above. We might still expect

tricarballylate to be photooxidized in a one-electron process; indeed, Kraeutler and Bard found that the most common photo-Kolbe product for a range of saturated organic acids was the alkane formed by dimerization (Equation 1.31).[96] The dimerization route in the electrochemical Kolbe process is known to be favored at high current densities,[93] and thus it may not proceed as readily at the relatively low current densities that we measure for our Ag nanoparticle photoanodes. Further, if the rate of decarboxylation following the one-electron oxidation of tricarballylate is slower than the corresponding rate for citrate, the oxidation reaction may not be competitive with the rate of hot hole return to the particle.

As discussed in Chapter 1.3, other types of photochemical reactions have been found to occur in SERS studies of molecules adsorbed on colloidal Ag particles. Moskovits and colleagues, for example, reported the photodegradation of phthalazine and identified Raman peaks from the decomposition product.[26,30] They observed a linear relationship between the incident light intensity and the reaction rate, indicative of a photochemical process. We found a negligible photoresponse for an aqueous solution of 1 mM phthalazine/100 mM KNO_3 at an evaporated Ag nanoparticle-ITO electrode, with photocurrent densities comparable to those in 100 mM KNO_3 alone. In the studies by Moskovits and coworkers, 10s of mW of incident laser power was focused to a much smaller spot than the white light illumination in our experiments. Further, the contribution of different molecular species to the SERS signals need not be proportional to concentration, and they suggested that the photoproduct likely experiences a larger SERS enhancement than phthalazine itself.[26] It may be that phthalazine

photodegradation did occur in our experiments, but that the reaction quantum yield was too low for us to resolve in our photoelectrochemical setup.

1.7.2 Spectral Photoresponse of Ag Nanoparticle Electrodes

There are two contributions to the wavelength-dependent photoresponse of the Ag nanoparticle electrodes. First, the electrode will absorb a great fraction of incident photons at wavelengths near its plasmon resonance. Second, we expect that the hot holes generated by higher-energy photons will be deeper below the Ag Fermi level and thus more strongly oxidizing toward adsorbed citrate. This effect should result in an increase in the photocurrent and photovoltage with decreasing wavelength. Theoretical support for this second prediction can be obtained from a modification of Gerischer-Marcus theory. Gerischer-Marcus theory describes the kinetics of heterogeneous charge transfer between a metal or semiconductor electrode and molecules in solution.[74] The theory provides an expression for the rate of oxidation of a species R:

$$k_b = \nu \int_{-\infty}^{\infty} \varepsilon_{ox}(\mathbf{E}) W_R(\lambda, \mathbf{E})[1 - f(\mathbf{E})]\rho(\mathbf{E}) d\mathbf{E} \qquad 1.34$$

where R forms a redox couple with an oxidized species in solution, O. In the expression above, k_b is the oxidation rate, **E** is the energy of states participating in the charge transfer, λ is the reorganization energy of the species R, $\rho(\mathbf{E})$ is the density of states of the metal at energy **E**, and $\varepsilon_{ox}(\mathbf{E})$ is a proportionality function relating the probability of electron transfer at energy **E** to the density of occupied molecular states at that energy. The interpretation of the frequency factor ν varies, but often ν is taken to the frequency of attempts by the system to cross the activation energy barrier of the reaction. The term

$f(\mathbf{E})$ is the Fermi function describing the probability of occupancy of a state of energy **E** by an electron in the metal:

$$f(\mathbf{E}) = \frac{1}{1 + e^{\frac{\mathbf{E}-\mathbf{E}_F}{k_B T}}} \tag{1.35}$$

Here k_B is the Boltzmann constant, T is temperature, and $\mathbf{E}_F$ is the Fermi level of the solid. From this expression, it is clear that the Fermi level corresponds to the energy at which an electronic state in the metal has a 50% probability of being occupied. The function $W_R(\lambda, \mathbf{E})$ in Equation 1.34 is a probability distribution function for the occupied molecular states. It has the form of a Gaussian function centered at $\mathbf{E}^0 - \lambda$:

$$W_R(\lambda, \mathbf{E}) = \frac{1}{\sqrt{4\pi\lambda k_B T}} e^{\frac{-(\mathbf{E}-\mathbf{E}^0+\lambda)^2}{4\lambda k_B T}} \tag{1.36}$$

where $\mathbf{E}^0$ is the standard potential of the molecular redox couple converted to an energy scale measured relative to the vacuum energy. The density of molecular states at energy **E** in species R is:

$$D_R(\lambda, \mathbf{E}) = N_A C_R(0,t) W_R(\lambda, \mathbf{E}) \tag{1.37}$$

where N_A is Avogadro's number and $C_R(0, t)$ is the surface concentration of species R at time t. Similar expressions for $D_O(\lambda, \mathbf{E})$ and $W_O(\lambda, \mathbf{E})$ can be derived for the species O. Figure 1.21 illustrates the metal-molecule system and important parameters in Gerischer-Marcus theory.

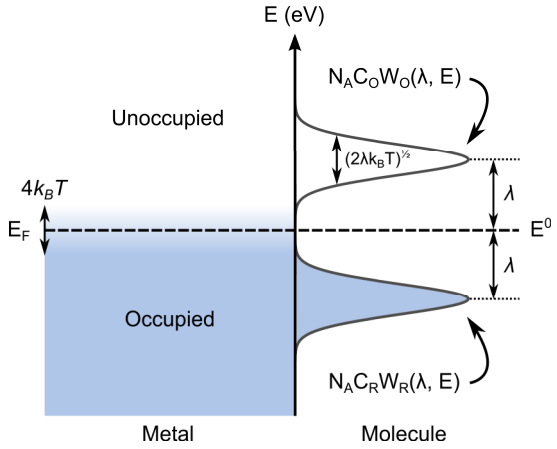

Figure 1.21 Schematic illustrating parameters relevant to charge transfer between a metal electrode and solution redox couple O/R in Gerischer-Marcus theory.

Equation 1.34 gives the total oxidation rate as an integral of the local oxidation rate (*i.e.*, the rate at a given energy **E**) over all values of **E**. The product of $[1 - f(\mathbf{E})]$ term and $\rho(\mathbf{E})$ gives the density of unoccupied metallic states at energy **E** that can accept an electron. Then the local oxidation rate at energy **E** is proportional to the density of available states in the metal at that energy, the proportionality factor $\varepsilon_{ox}(\mathbf{E})$, and the distribution function of occupied molecular states, $W_R(\lambda, \mathbf{E})$. For the energy level alignment shown in Figure 1.21, there are no unoccupied energy levels on the metal overlapping filled states on the molecule. The reverse also holds, and thus there will be essentially no net charge transfer across the interface. If a positive potential is applied to the metal electrode, however, the Fermi level will be lowered. When the Fermi level has been lowered enough that unoccupied states on the metal overlap occupied states on the molecule, an anodic current will flow; that is, the molecule will be oxidized.

Equation 1.34 and the discussion in the previous paragraph describe the charge-transfer behavior for a system without hot electrons and holes. Electronic states in the

metal are completely filled below and completely empty above the Fermi level except for in a thin transition region approximately $4k_BT$ in width centered on $\mathbf{E}_F$. (At room temperature, $4k_BT$ is approximately 100 meV.) Hot electrons and holes correspond to occupied states above and unoccupied states below the Fermi level; these states are available to participate in charge-transfer reactions. Modestov and coworkers explored the hot carrier photoelectrochemistry of graphite in a series of articles[99-102] and adapted the standard Gerischer-Marcus model to account for these hot carrier processes.[100] Several changes must be made to Equation 1.34 to describe a hot hole photooxidation. First, the relevant density of available metallic states for the oxidation reaction is no longer $[1 - f(\mathbf{E})]\rho(\mathbf{E})$. Instead, it is determined by the hot electron concentration at the metal-solution interface, which will depend on the incident photon flux, the absorption of the metal, and the timescale for hot hole relaxation in comparison to the timescale for transit to the interface. Second, the effect of incident photon energy on the average energy of the hot holes must be accounted for in some way. Modestov *et al.* assumed that the photon energy was equally divided between the hot electrons and hot holes generated by light absorption in graphite.[100] From these modifications, they derived an expression for the reaction rate with an exponential dependence on photon energy and a linear dependence on the photon flux L and the absorption coefficient α:

$$k \propto L\alpha e^{\frac{\beta h\nu}{2}} \qquad 1.38$$

The factor β accounts for the average energy loss of the hot carriers at the surface, and $\beta < 1$ is required. Consistent with the prediction of Equation 1.38, Modestov *et al.* found that the graphite photocurrent quantum yield increased exponentially with photon energy, with some deviation observed at the upper end of the photon energy range.[100] The origin

of the photocurrent in graphite is not the same as in our Ag nanoparticle-citrate system, and thus the full charge transfer equation derived by Modestov and coworkers would require additional modification to be adapted to our results. Despite these distinctions, from this model we can expect a strong photon-energy dependence to the rate of hot carrier photoelectrochemical processes.

As seen in Figure 1.13 and Figure 1.14, the photoresponse for the three types of Ag nanoparticle electrodes appears to be dominated by photon energy. This behavior holds even for the colloidal Ag nanoprisms, which absorb weakly at shorter wavelengths. The explanation for the differences in the photovoltage and photocurrent action spectra of the evaporated Ag nanoparticle electrode at low wavelengths is not clear. Perhaps another electrode discharge pathway (*i.e.*, another reduction process) becomes available at higher shifts from rest potential, leading to a slower increase in the photovoltage even as the rate of citrate photooxidation continues to rise. The colloidal Ag nanoparticle electrodes might not show the same effect because they do not shift as far from their dark open-circuit potential under irradiation.

It should be noted that direct photoinduced charge-transfer transitions are also possible in metal-molecule systems, as illustrated in Figure 1.20b,[34] and the rate of these transitions might have a similar wavelength-dependence. In their SERS studies of phthalazine adsorbed on Ag colloids, Moskovits and coworkers found that the rate constant for the photochemical degradation of phthalazine did not track the surface plasmon resonance of the colloid.[26] The reaction rate increased as the incident laser wavelength changed from 568.2 nm to 457.9 nm even though the SERS enhancement—and thus, presumably, the enhancement in the local electromagnetic field—peaked near

530.9 nm. Like citrate, phthalazine does not absorb visible light. The wavelength-dependence of the reaction rate was attributed to two effects: a metal-to-molecule charge-transfer transition, the cross-section of which would increase going into the UV, and the plasmonic electromagnetic field enhancement, shown to be greatest in the visible portion of the spectrum.

1.7.3 Quantum Yields of Ag Nanoparticle Electrodes

Figure 1.22 compares the calculated quantum yield per absorbed photon for the three types of Ag nanoparticle electrodes studied here. In general, even when accounting for electrode absorbance, the colloidal nanoparticle electrodes have a lower quantum yield than the evaporated nanoparticle electrode. We had expected that the more highly-crystalline colloidal nanoparticles would have higher quantum yields because hot-carrier relaxation at grain boundaries would be less significant. One possible explanation is that the polymer film (see Chapter 1.5.3) impedes the charge transfer between the colloidal particles and the ITO. As a control experiment, an evaporated Ag nanoparticle electrode was fabricated on a PAH-coated ITO substrate. There were no significant changes in the magnitude or spectral shape of the photoresponse for that electrode in comparison to Ag nanoparticle-ITO electrodes. Another possible explanation for the weak photoresponse of the colloidal particles is that the surfactant layer acts as an insulating barrier between the particle and the substrate.

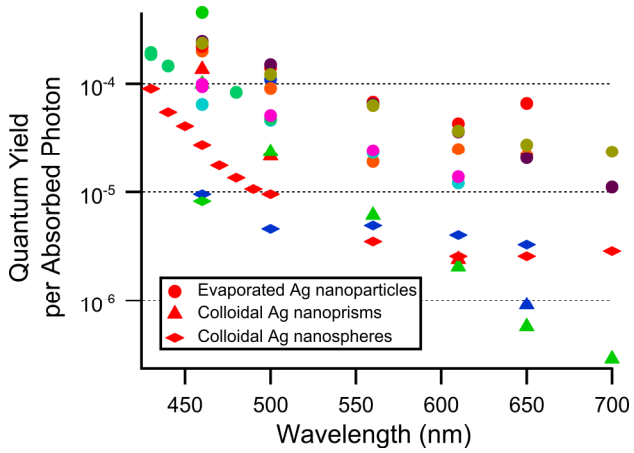

Figure 1.22 Quantum yield per absorbed photon plotted for 15 different Ag nanoparticle electrodes of 3 types: evaporated Ag nanoparticle electrodes (circles), colloidal Ag nanoprism electrodes (triangles), and colloidal Ag nanospheres (diamonds).

It should be noted that Redmond *et al.*[82] estimated a citrate photooxidation quantum yield of 0.5% per absorbed photon for colloidal Ag particles at 488 nm, which translates to a 1% quantum yield in terms of electrons per absorbed photon. The values that we measure for Ag nanoparticles on a semiconductor substrate are two to three orders of magnitude lower. In the case of colloidal Ag particles, electrons generated by citrate photooxidation accumulate on the particle until a sufficient cathodic voltage is built up to allow reduction Ag^{+}. For the Ag nanoparticle electrodes, however, photogenerated electrons must travel into the semiconductor support and from there to the external circuit to contribute to the measured photocurrent. This difference in the two experiments is probably a significant factor in explaining the discrepancy in the quantum yields.

1.7.4 Role of the Substrate and Enhancement Mechanisms

Finally, we address the possibility that the electrode substrates might be playing a role in the observed photoresponse. ITO is a degenerately doped *n*-type semiconductor with properties that are known to be extremely sensitive to the details of the fabrication process. In principle, ITO can undergo photoelectrochemistry even at photon energies below the band gap energy of 3.5 – 4.3 eV because of a high density of states in the band gap.[103] TiO_2 is a well-known photocatalyst with a band gap of 3.0 eV in the rutile form.[104] Nonetheless, we conclude from several experimental results that what we are measuring is the photoresponse of the Ag nanoparticles.

First, we measure an extremely weak photocurrent (< 1 nA/cm^2) on a bare ITO electrode under our experimental conditions. Similarly, Redmond *et al.* reported that the charge-transfer rate for the reduction of water or Ag^+ on bare ITO was one to two orders of magnitude lower than the rate on a thin Ag film.[85] These results suggest that the Ag nanoparticles are responsible for the majority of the charge transfer in our experiments. This conclusion is consistent with enhancement mechanism i) discussed in Chapter 1.3. We are unable to measure a difference in the charge-transfer rate for the oxidation of citrate in the presence of Ag nanoparticles because citrate is oxidized at potentials positive of Ag.[105] We also note that the ITO potential does appear to shift negative, albeit slowly, in the presence of the supporting electrolyte and citrate, but that the shift is suppressed when a micromolar concentration of Ag^+ is present in the electrolyte. In the presence of Ag particles, even under a blanket of inert gas, we expect some small equilibrium concentration of Ag^+ to result from oxidative etching of the particles. This small concentration should suppress the potential shift due to the ITO.

Even if the charge transfer and storage occurs on the Ag nanoparticles, it could be that ITO absorbs the light and then transfers a hole to the Ag particles, which subsequently oxidize citrate. In a series of articles, Kamat *et al.* showed that the deposition of Au nanoparticles on TiO_2 increased the photocurrent upon band-gap excitation of the TiO_2.[51,52,60] In our case, however, the photocurrent response is not uniformly enhanced when Ag nanoparticles are deposited on ITO. Instead, the Ag nanoparticle electrode photoresponse is significant only when citrate is added to the electrolyte. The photocurrent measured in KNO_3 alone is approximately an order of magnitude larger for the Ag NP-ITO electrode than for the bare ITO electrode, but in the presence of citrate the Ag NP-ITO electrode photocurrent is over 100-fold larger than that of the bare ITO electrode. As noted previously, the bare ITO photoresponse is essentially the same with or without citrate added to the 100 mM KNO_3 supporting electrolyte (Figure 1.15). Kamat and coworkers attributed some of the improved photoelectrochemical performance of Au nanoparticle-TiO_2 electrodes to mechanism ii) from Chapter 1.3, a shift of the semiconductor Fermi level to more positive potentials under illumination. Unlike TiO_2, however, ITO is degenerately doped; the Fermi level is already close to the conduction band. It is not clear that mechanism ii) would be significant in such a system.

As shown in Figure 1.17, the Ag nanoparticle electrode photoresponse is essentially the same when ITO from different suppliers is used and also broadly similar when FTO is used as the substrate. We are not sure of the reason for the lower quantum yields measured on FTO, but it is worth noting that they are still within the range of experimental variation. In addition to sources of experimental uncertainty, such as small

changes in the light intensity or irreproducibility in the positioning of the power meter, we note that the calculation of quantum yields using only one data point introduces some additional error.

In terms of the four photoelectrochemical enhancement mechanisms discussed in Chapter 1.3, we are proposing a variant of mechanism iv), where photoexcited carriers generated in the nanoparticle are responsible for the charge separation. We had expected that the space charge region at the interface between the Ag nanoparticles and single-crystal *n*-TiO_2 would assist in sweeping photoexcited electrons away from the particles; from the similar quantum yields that we measured for Ag nanoparticle on *n*-TiO_2 electrodes, this does not appear to be the case. Nonetheless, our results are still consistent with a mechanism where the irreversible photooxidation of citrate by hot holes is responsible for the charge separation. In our experiments we may not be able to distinguish between a mechanism where photoexcited hot electrons are transferred to the semiconductor and a mechanism where the accumulation of electrons from citrate photooxidation charges the nanoparticle, raising the Fermi level and allowing transfer of thermalized electrons to the semiconductor.

Further, we note that even if charge separation in this system occurs through the photooxidation of citrate by Ag nanoparticles, as we have proposed, the presence of the substrate might still affect the observed action spectrum. As discussed in Chapter 1.7.3, the presence of the semiconductor substrate requires electrons to tunnel off the Ag nanoparticles to contribute to the electrode photoresponse. If the citrate photooxidation rate tracked the nanoparticle plasmon resonance spectrum but the rate of electron transfer

to the substrate was limiting, the overall action spectrum would primarily reflect the rate of electron transfer to the substrate.

1.8 Conclusion

We have measured the wavelength-dependence of citrate photooxidation by Ag nanoparticles on semiconductor substrates in a photoelectrochemical cell. We observe similar action spectra for three different types of Ag nanoparticles with different localized surface plasmon resonance positions, and we also find that the response is broadly similar for different types of semiconductor substrates. From these results, we conclude that photon energy is the dominant factor in the citrate photooxidation reaction rate. These findings are compatible with a photochemical mechanism involving the transfer of photoexcited hot holes to adsorbed citrate. Other workers have reported a strong photon energy-dependence to hot-carrier photo(electro)chemistry in different systems; theoretical support for this behavior can be derived from a modified Gerischer-Marcus theory. The remarkable optical properties of metal nanoparticles continue to be of great fundamental and applied scientific interest, and the plasmon-mediated photochemistry of hot carriers remains a promising but still imperfectly-understood phenomenon.

1.9 References

(1) Ashcroft, N. W.; Mermin, N. D. *Solid state physics*; Holt: New York,, 1976.

(2) Kittel, C. *Introduction to solid state physics*; 8th ed.; Wiley: Hoboken, NJ, 2005.

(3) Barnes, W. L.; Dereux, A.; Ebbesen, T. W. *Nature* **2003**, *424*, 824.

(4) Maier, S. A.; Atwater, H. A. *Journal of Applied Physics* **2005**, *98*.

(5) Maier, S. A. *Plasmonics : fundamentals and applications*; Springer: New York, 2007.

(6) Kreibig, U.; Vollmer, M. *Optical properties of metal clusters*; Springer: Berlin ; New York, 1995.

(7) Myroshnychenko, V.; Rodriguez-Fernandez, J.; Pastoriza-Santos, I.; Funston, A. M.; Novo, C.; Mulvaney, P.; Liz-Marzan, L. M.; de Abajo, F. J. G. *Chemical Society Reviews* **2008**, *37*, 1792.

(8) Kelly, K. L.; Coronado, E.; Zhao, L. L.; Schatz, G. C. *Journal of Physical Chemistry B* **2003**, *107*, 668

(9) Willets, K. A.; Van Duyne, R. P. *Annu Rev Phys Chem* **2007**, *58*, 267.

(10) Zhao, J.; Pinchuk, A. O.; Mcmahon, J. M.; Li, S. Z.; Ausman, L. K.; Atkinson, A. L.; Schatz, G. C. *Accounts of Chemical Research* **2008**, *41*, 1710.

(11) Jackson, J. D. *Classical electrodynamics*; 3rd ed.; Wiley: New York, 1999.

(12) Moskovits, M. *J Raman Spectrosc* **2005**, *36*, 485.

(13) Johnson, P. B.; Christy, R. W. *Phys Rev B* **1972**, *6*, 4370.

(14) Jiang, J.; Bosnick, K.; Maillard, M.; Brus, L. *Journal of Physical Chemistry B* **2003**, *107*, 9964.

(15) Link, S.; El-Sayed, M. A. *The Journal of Physical Chemistry B* **1999**, *103*, 8410.

(16) Link, S.; Ei-Sayed, M. A. *Annu Rev Phys Chem* **2003**, *54*, 331.

(17) Le Ru, E. C.; Blackie, E.; Meyer, M.; Etchegoin, P. G. *The Journal of Physical Chemistry C* **2007**, *111*, 13794.

(18) Nie, S. M.; Emery, S. R. *Science* **1997**, *275*, 1102.

(19) Bosnick, K. A.; Jiang; Brus, L. E. *The Journal of Physical Chemistry B* **2002**, *106*, 8096.

(20) Michaels, A. M.; Jiang; Brus, L. *The Journal of Physical Chemistry B* **2000**, *104*, 11965.

(21) Michaels, A. M.; Nirmal, M.; Brus, L. E. *Journal of the American Chemical Society* **1999**, *121*, 9932.

(22) Jensen, L.; Aikens, C. M.; Schatz, G. C. *Chemical Society Reviews* **2008**, *37*, 1061.

(23) Brus, L. *Accounts of Chemical Research* **2008**, *41*, 1742

(24) Lombardi, J. R.; Birke, R. L. *Accounts of Chemical Research* **2009**, *42*, 734.

(25) Suh, J. S.; Moskovits, M.; Shakhesemampour, J. *Journal of Physical Chemistry* **1993**, *97*, 1678.

(26) Suh, J. S.; Jang, N. H.; Jeong, D. H.; Moskovits, M. *Journal of Physical Chemistry* **1996**, *100*, 805.

(27) Bjerneld, E. J.; Svedberg, F.; Johansson, P.; Kall, M. *J Phys Chem A* **2004**, *108*, 4187.

(28) Alaverdyan, Y.; Johansson, P.; Kall, M. *Phys Chem Chem Phys* **2006**, *8*, 1445.

(29) Huang, Y. F.; Zhu, H. P.; Liu, G. K.; Wu, D. Y.; Ren, B.; Tian, Z. Q. *Journal of the American Chemical Society* **2010**, *132*, 9244.

(30) Vlckova, B.; Gu, X. J.; Moskovits, M. *Journal of Physical Chemistry B* **1997**, *101*, 1588.

(31) Nitzan, A.; Brus, L. E. *J Chem Phys* **1981**, *74*, 5321.

(32) Nitzan, A.; Brus, L. E. *J Chem Phys* **1981**, *75*, 2205.

(33) Hasselbrink, E. *Appl Surf Sci* **1994**, *80*, 34.

(34) Lindstrom, C. D.; Zhu, X. Y. *Chem Rev* **2006**, *106*, 4281.

(35) Watanabe, K.; Menzel, D.; Nilius, N.; Freund, H. J. *Chem Rev* **2006**, *106*, 4301.

(36) Zhu, X. Y. *Annu Rev Phys Chem* **1994**, *45*, 113.

(37) Diesing, D.; Kritzler, G.; Otto, A.; Wandelt, K., Thurgate, S., Eds.; Springer Berlin / Heidelberg: 2003; Vol. 85, p 367.

(38) Fedurco, M.; Shklover, V.; Augustynski, J. *Journal of Physical Chemistry B* **1997**, *101*, 5158.

(39) Kowalska, E.; Abe, R.; Ohtani, B. *Chem Commun* **2009**, 241.

(40) Naya, S.; Inoue, A.; Tada, H. *Journal of the American Chemical Society* **2010**, *132*, 6292.

(41) Hung, W. H.; Aykol, M.; Valley, D.; Hou, W. B.; Cronin, S. B. *Nano Letters* **2010**, *10*, 1314.

(42) Chen, X.; Zhu, H. Y.; Zhao, J. C.; Zheng, Z. T.; Gao, X. P. *Angew Chem Int Edit* **2008**, *47*, 5353.

(43) Christopher, P.; Xin, H. L.; Linic, S. *Nat Chem* **2011**, *3*, 467.

(44) Christopher, P.; Ingram, D. B.; Linic, S. *Journal of Physical Chemistry C* **2010**, *114*, 9173.

(45) Sauthier, G.; del Pino, A. P.; Figueras, A.; Gyorgy, E. *J Am Ceram Soc* **2011**, *94*, 3780.

(46) Hou, W. B.; Liu, Z. W.; Pavaskar, P.; Hung, W. H.; Cronin, S. B. *J Catal* **2011**, *277*, 149.

(47) Awazu, K.; Fujimaki, M.; Rockstuhl, C.; Tominaga, J.; Murakami, H.; Ohki, Y.; Yoshida, N.; Watanabe, T. *Journal of the American Chemical Society* **2008**, *130*, 1676.

(48) Zhu, H. Y.; Ke, X. B.; Yang, X. Z.; Sarina, S.; Liu, H. W. *Angew Chem Int Edit* **2010**, *49*, 9657.

(49) Hou, W. B.; Hung, W. H.; Pavaskar, P.; Goeppert, A.; Aykol, M.; Cronin, S. B. *Acs Catal* **2011**, *1*, 929.

(50) Teranishi, M.; Naya, S.; Tada, H. *Journal of the American Chemical Society* **2010**, *132*, 7850.

(51) Chandrasekharan, N.; Kamat, P. V. *Journal of Physical Chemistry B* **2000**, *104*, 10851

(52) Subramanian, V.; Wolf, E.; Kamat, P. V. *Journal of Physical Chemistry B* **2001**, *105*, 11439

(53) Tian, Y.; Tatsuma, T. *Journal of the American Chemical Society* **2005**, *127*, 7632.

(54) Zhao, G.; Kozuka, H.; Yoko, T. *Thin Solid Films* **1996**, *277*, 147.

(55) Liu, Z. W.; Hou, W. B.; Pavaskar, P.; Aykol, M.; Cronin, S. B. *Nano Letters* **2011**, *11*, 1111.

(56) Ingram, D. B.; Linic, S. *Journal of the American Chemical Society* **2011**, *133*, 5202.

(57) Nishijima, Y.; Ueno, K.; Yokota, Y.; Murakoshi, K.; Misawa, H. *J Phys Chem Lett* **2010**, *1*, 2031.

(58) Choi, H.; Chen, W. T.; Kamat, P. V. *Acs Nano* **2012**, *6*, 4418.

(59) Linic, S.; Christopher, P.; Ingram, D. B. *Nat Mater* **2011**, *10*, 911.

(60) Jakob, M.; Levanon, H.; Kamat, P. V. *Nano Letters* **2003**, *3*, 353

(61) Subramanian, V.; Wolf, E. E.; Kamat, P. V. *Journal of the American Chemical Society* **2004**, *126*, 4943.

(62) Henglein, A.; Lilie, J. *Journal of the American Chemical Society* **1981**, *103*, 1059.

(63) Ung, T.; Giersig, M.; Dunstan, D.; Mulvaney, P. *Langmuir* **1997**, *13*, 1773.

(64) Wood, A.; Giersig, M.; Mulvaney, P. *Journal of Physical Chemistry B* **2001**, *105*, 8810.

(65) Hirakawa, T.; Kamat, P. V. *Langmuir* **2004**, *20*, 5645.

(66) Furube, A.; Du, L.; Hara, K.; Katoh, R.; Tachiya, M. *Journal of the American Chemical Society* **2007**, *129*, 14852.

(67) Du, L. C.; Furube, A.; Yamamoto, K.; Hara, K.; Katoh, R.; Tachiya, M. *Journal of Physical Chemistry C* **2009**, *113*, 6454.

(68) Hagfeldt, A.; Gratzel, M. *Accounts of Chemical Research* **2000**, *33*, 269.

(69) Gratzel, M. *J Photoch Photobio A* **2004**, *164*, 3.

(70) Gratzel, M. *Inorganic Chemistry* **2005**, *44*, 6841.

(71) Peter, L. M. *Journal of Physical Chemistry C* **2007**, *111*, 6601.

(72) Prezhdo, O. V.; Duncant, W. R.; Prezhdo, V. V. *Accounts of Chemical Research* **2008**, *41*, 339.

(73) Marcus, R. A. *Angewandte Chemie-International Edition in English* **1993**, *32*, 1111.

(74) Bard, A. J.; Faulkner, L. R. *Electrochemical methods : fundamentals and applications*; 2nd ed.; Wiley: New York, 2001.

(75) Nozik, A. J.; Memming, R. *The Journal of Physical Chemistry* **1996**, *100*, 13061.

(76) Knight, M. W.; Sobhani, H.; Nordlander, P.; Halas, N. J. *Science* **2011**, *332*, 702.

(77) Jin, R.; Cao, Y.; Mirkin, C. A.; Kelly, K. L.; Schatz, G. C.; Zheng, J. G. *Science* **2001**, *294*, 1901

(78) Jin, R. C.; Cao, Y. C.; Hao, E. C.; Metraux, G. S.; Schatz, G. C.; Mirkin, C. A. *Nature* **2003**, *425*, 487.

(79) Maillard, M.; Huang, P.; Brus, L. *Nano Letters* **2003**, *3*, 1611

(80) Callegari, A.; Tonti, D.; Chergui, M. *Nano Letters* **2003**, *3*, 1565.

(81) Pastoriza-Santos, I.; Liz-Marzan, L. M. *J Mater Chem* **2008**, *18*, 1724.

(82) Redmond, P. L.; Wu, X.; Brus, L. *Journal of Physical Chemistry C* **2007**, *111*, 8942

(83) Wu, X.; Redmond, P. L.; Liu, H.; Chen, Y.; Steigerwald, M.; Brus, L. *Journal of the American Chemical Society* **2008**, *130*, 9500

(84) Xue, C.; Métraux, G. S.; Millstone, J. E.; Mirkin, C. A. *Journal of the American Chemical Society* **2008**, *130*, 8337

(85) Redmond, P. L.; Brus, L. E. *Journal of Physical Chemistry C* **2007**, *111*, 14849

(86) Wu, X. M.; Thrall, E. S.; Liu, H. T.; Steigerwald, M.; Brus, L. *Journal of Physical Chemistry C* **2010**, *114*, 12896.

(87) Lu, Y.; Jaeckel, B.; Parkinson, B. A. *Langmuir* **2006**, *22*, 4472.

(88) Lu, Y. F.; Choi, D. J.; Nelson, J.; Yang, O. B.; Parkinson, B. A. *J Electrochem Soc* **2006**, *153*, E131.

(89) Métraux, G. S.; Mirkin, C. A. *Advanced Materials* **2005**, *17*, 412

(90) Lee, P. C.; Meisel, D. *Journal of Physical Chemistry* **1982**, *86*, 3391

(91) Erol, M.; Han, Y.; Stanley, S. K.; Stafford, C. M.; Du, H.; Sukhishvili, S. *Journal of the American Chemical Society* **2009**, *131*, 7480

(92) Quinten, M.; Kreibig, U.; Schönauer, D.; Genzel, L. *Surface Science* **1985**, *156*, 741

(93) Lund, H.; Hammerich, O. *Organic electrochemistry*; 4th ed.; M. Dekker: New York, 2001.

(94) Kraeutler, B.; Bard, A. J. *Journal of the American Chemical Society* **1977**, *99*, 7729.

(95) Kraeutler, B.; Bard, A. J. *Journal of the American Chemical Society* **1978**, *100*, 2239.

(96) Kraeutler, B.; Bard, A. J. *Journal of the American Chemical Society* **1978**, *100*, 5985.

(97) Gutiérrez, M.; Henglein, A. *Journal of Physical Chemistry* **1993**, *97*, 11368.

(98) Kilin, D. S.; Prezhdo, O. V.; Xia, Y. *Chemical Physics Letters* **2008**, *458*, 113

(99) Modestov, A. D.; Gun, J.; Lev, O. *Surface Science* **1998**, *417*, 311.

(100) Modestov, A. D.; Gun, J.; Lev, O. *J Electroanal Chem* **1999**, *476*, 118.

(101) Modestov, A. D.; Gun, J.; Lev, O. *Langmuir* **2000**, *16*, 4678.

(102) Modestov, A. D.; Gun, J.; Lev, O. *J Electroanal Chem* **2000**, *491*, 39.

(103) van den Meerakker, J. E. A. M.; Meulenkamp, E. A.; Scholten, M. *Journal of Applied Physics* **1993**, *74*, 3282

(104) Sambur, J. B.; Novet, T.; Parkinson, B. A. *Science* **2010**, *330*, 63.

(105) Chailapakul, O.; Popa, E.; Tai, H.; Sarada, B. V.; Tryk, D. A.; Fujishima, A. *Electrochem Commun* **2000**, *2*, 422.

Chapter 2

R6G on Graphene: High Raman Detection Sensitivity, Yet Decreased Raman Cross-Section[1]

Several recent studies have demonstrated the use of single- and few-layer graphene as a substrate for the enhancement of Raman scattering by adsorbed molecules, in a method termed graphene-enhanced Raman spectroscopy (GERS). Here we determine the resonance Raman scattering cross-section for the dye molecule rhodamine 6G (R6G) adsorbed on bilayer graphene. For the 1650 cm^{-1} R6G mode, we obtain a cross-section of 5.1×10^{-24} $cm^2 \cdot molecule^{-1}$, a greater than three-fold reduction from the previously reported solution value. We show that the absorption spectrum of adsorbed R6G can be measured using micro-optical contrast spectroscopy, and we find that detuning of the molecular resonance explains the decreased Raman scattering cross-section. We find no evidence for a graphene Raman enhancement process. We also study the graphene thickness dependence of the adsorbed R6G Raman signal and show that a model incorporating electromagnetic interference effects can qualitatively explain the decrease in signal with increasing graphene thickness.

[1] Portions of the material presented in this chapter were previously published in Thrall, Elizabeth S.; Crowther, Andrew C.; Yu, Zhonghua; Brus, Louis E. *Nano Lett*. **2012**, *12*, 1571.

2.1 Introduction to Graphene

The discovery of graphene in 2004 marked the start of a new era in the study of carbon materials.[1,2] Graphene is a single atomic layer of the carbon allotrope graphite, composed of sp^2 hybridized carbon atoms in a hexagonal lattice. Stacking 2D graphene layers, which interact weakly through van der Waals forces, gives 3D graphite. Yet graphene can also be thought of as the building block for lower dimensional sp^2 carbon materials: 0D fullerenes and 1D carbon nanotubes. Rolling up a graphene sheet along different axes gives carbon nanotubes of different chiralities, while fullerenes can be (conceptually) formed by folding irregular strips of graphene into balls composed of pentagonal, hexagonal, and heptagonal carbon rings. Although graphene had been studied theoretically for decades[3] and although thin graphitic films were known,[1] it was believed that purely 2D materials were thermodynamically unstable, subject to strong thermally-excited vibrations that would disrupt the crystal lattice.[2]

Remarkably, single graphene layers can be isolated by micromechanical exfoliation and deposited on a surface. In micromechanical exfoliation, alternatively called the "Scotch tape method," graphite flakes are repeatedly peeled apart by tape, which is then pressed on a substrate to transfer material. The majority of the flakes transferred to the substrate are thick graphite pieces, but single- and few-layer graphene pieces may also be present. Despite being only a single atomic layer thick, graphene flakes deposited on substrates like quartz or Si with a 300 nm SiO_2 coating are visible in an optical microscope. Single- and few-layer graphene flakes with lateral dimensions of microns or tens of microns can be prepared and identified in this manner.

This simple method for preparing graphene on various substrates has allowed researchers to study its unusual physical and chemical properties. The graphene unit cell (Figure 2.1a) is composed of two atoms, representing two equivalent carbon sublattices, A and B. This honeycomb structure is not a simple 2D Bravais lattice but is instead a triangular lattice with a two-atom basis. The C-C bond length between A and B atoms is 0.142 nm. For comparison, the interlayer distance in Bernal-stacked graphite (with ABA out-of-plane ordering) is 0.335 nm, more than twice the in-plane C-C separation. The hexagonal graphene Brillouin zone is shown in Figure 2.1b, with the high-symmetry Γ, K, and M points indicated. Graphene is a zero-overlap semimetal; the valence (π) and conduction (π*) bands meet at the K and K′ points in the Brillouin zone.

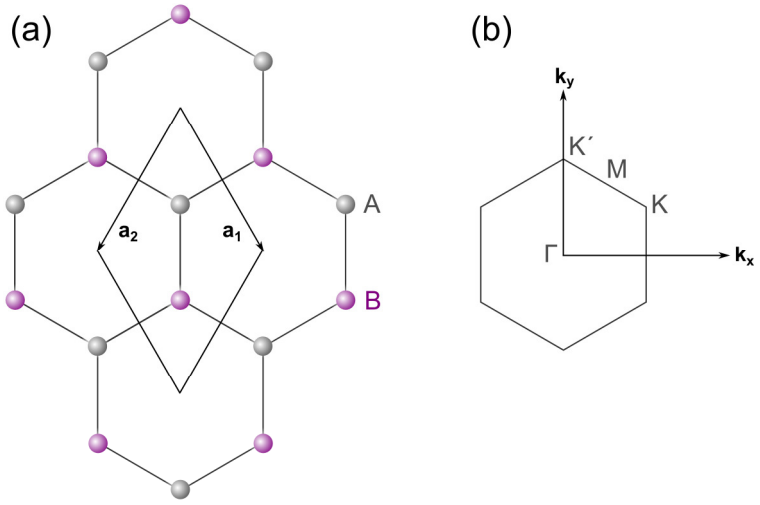

Figure 2.1 (a) Graphene unit cell unit vectors $\mathbf{a}_1$ and $\mathbf{a}_2$ and carbon sublattices A and B. (b) First graphene Brillouin zone with reciprocal lattice vectors $\mathbf{b}_1$ and $\mathbf{b}_2$. The zone-center Γ point, the K and K´ points, and the M point are also shown.

The graphene band structure can be calculated using the tight binding method, which results in the energy dispersion:

$$E_{\pm}(\mathbf{k}) = \pm t\sqrt{3 + f(\mathbf{k})} - t'f(\mathbf{k}) \qquad 2.1$$

where E_+ and E_- are the conduction and valence bands.[3] The parameters t and t' are the nearest-neighbor and next nearest-neighbor hopping energies, corresponding to the energy for electron hopping between A and B sublattices and within one sublattice, respectively. The function $f(\mathbf{k})$ is given by:

$$f(\mathbf{k}) = 2\cos(\sqrt{3}k_y a) + 4\cos(\frac{\sqrt{3}}{2}k_y a)\cos(\frac{3}{2}k_x a) \qquad 2.2$$

where a is the C-C distance. The electronic dispersion is plotted in Figure 2.2 for the values t = 2.7 eV, t' = − 0.54 eV, and a = 1.42 Å, taken from Reference 3.

The Fermi level lies at the K point in undoped graphene. For low energies around this point, the energy bands are conical and the electron dispersion is linear:

$$E(\mathbf{k}) = \hbar \upsilon_F |\mathbf{k}| \qquad 2.3$$

where $\hbar$ is the reduced Planck's constant, v_F is the Fermi velocity, and the wave vector $\mathbf{k}$ is measured relative to the K point wave vector, $\mathbf{K}$. The dispersion is independent of the electron mass m. In a typical semiconductor, the band energy depends on $\mathbf{k}$ and the carrier mass as:

$$E(\mathbf{k}) = \frac{\hbar^2 |\mathbf{k}|^2}{2m} \qquad 2.4$$

The energy dispersion in Equation 2.3 is analogous to the dispersion relation for light, but with the speed of light replaced by the Fermi velocity. It is characteristic of massless relativistic quantum mechanical particles that obey the Dirac equation rather than the

Schrödinger equation. In graphene, the behavior of electrons near the K point can be described in terms of such massless Dirac fermions. For this reason, the K point in graphene is referred to as the Dirac point. Many of the exotic electronic properties of graphene arise in part from this unusual dispersion.[2] In addition to the richness of its fundamental physics, however, graphene also possesses electronic properties that are promising for future applications: an ambipolar field effect, ultra-high carrier mobilities of greater than 200,000 $cm^2 \cdot V^{-1} \cdot s^{-1}$,[4] and ballistic transport over micrometer distances even at room temperature.[5]

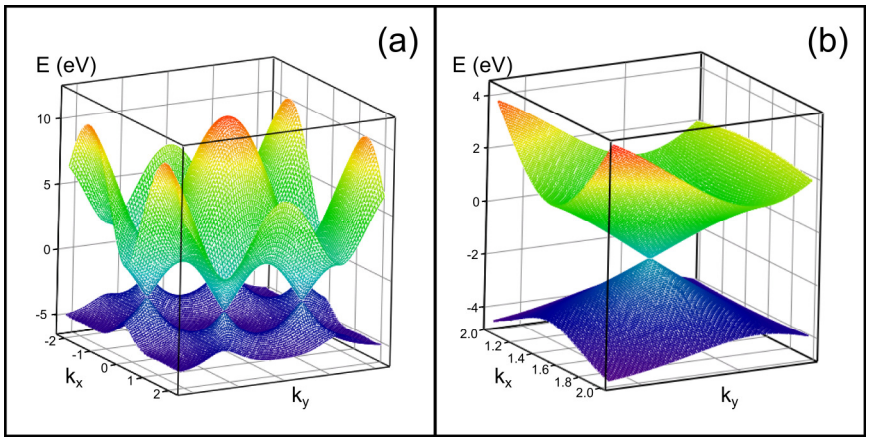

Figure 2.2 (a) Graphene band structure calculated using the tight binding Hamiltonian.[3] (b) Graphene band structure in the region of the K point.

2.2 Spectroscopy of Graphene

2.2.1 Raman Spectroscopy

Raman scattering is the inelastic scattering of light from a material, in which a photon incident on the material scatters from it at a different frequency. The change in

frequency of the photon reflects either a gain or, more commonly, a loss of energy when the photon excites vibrational, rotational, or electronic modes of the system. It was quickly recognized after the discovery of graphene that Raman spectroscopy, as a non-destructive spectroscopic method amenable to the study of micron-sized materials in a microscope, was a valuable tool for characterization.[6] Raman spectroscopy of graphitic materials is a rich subject, and the spectra of graphite, graphene, carbon nanotubes, and fullerenes share similar features.[7-9] The absence of a band gap in graphene and several other sp^2 carbon systems means that Raman excitation at any wavelength is resonant, which both enhances the Raman intensity and, as discussed by Ferrari, couples the electronic properties of the materials to their vibrational Raman modes.[7] Vibrations of atoms in the graphene lattice can be described in terms of the phonon modes of the system. The graphene phonon dispersion, the relationship between phonon frequency and wave vector, has been calculated using density functional perturbation theory, and it shows good agreement with the experimental graphite phonon dispersion obtained from inelastic x-ray scattering.[7] As a crystal with a two-atom basis, graphene supports six different phonon branches, three acoustic and three optical. Of the three acoustic phonons, two are transverse to the direction of propagation of the vibration and one is longitudinal; the same holds for the optical phonon modes.

In a typical graphene or graphite Raman spectrum, two features are present: the G band at approximately 1580 cm^{-1} and the 2D band near 2700 cm^{-1}. The G band is stronger than the 2D band for all but single-layer graphene, where it is weaker, and for bilayer graphene, where it is comparable in intensity. The G band corresponds to carbon-carbon stretching in the plane of the graphene; in terms of the graphene phonon

dispersion, it represents the in-plane transverse optical (iTO) and longitudinal optical (LO) phonons which are degenerate at the Brillouin zone center, the Γ point. These zone-center phonons have E_{2g} symmetry and wave vector $\mathbf{q} = \mathbf{0}$ and thus can be excited in a first-order Raman scattering process, which has the selection rule $\mathbf{q} = \mathbf{0}$.[7,8] The 2D band, alternatively called the G′ band because it is the second-strongest feature in the graphite Raman spectrum, has a shape that is dependent on the number on graphene layers. For single-layer graphene, the 2D band is a symmetric peak that can be fit to a single Lorentzian function. For thicker graphene pieces and for graphite, the 2D band is broad and asymmetric. The 2D peak is the overtone of the D peak, at approximately 1350 cm^{-1}, which is only seen at flake edges or when defects are present. The D peak is a ring-breathing mode of the graphene lattice. The D and 2D peaks both arise from iTO phonons at the K point in the graphene Brillouin zone. Normally these phonons of $\mathbf{q} \approx \mathbf{K}$ would not be Raman active. In the case of the D peak, electron-phonon scattering excites a phonon of $\mathbf{q} \approx \mathbf{K}$ with a frequency of ω_D. This momentum is balanced by an additional scattering event from a defect or flake edge, transferring momentum of $\mathbf{q} \approx -\mathbf{K}$ to the electron. For the 2D band, the additional scattering event is a second electron-phonon scattering, where a phonon of momentum $\mathbf{q} \approx -\mathbf{K}$ is excited. No defect is required to activate this scattering process. Second-order Raman scattering bands are generally weak, but the strong intensity of the D and 2D bands is explained by the involvement of two real electronic states (rather than virtual states), in what is termed a double resonance Raman process. These processes are illustrated in Figure 2.3a. The D and 2D bands are linearly dispersive with excitation energy; ω_D increases with a slope of approximately 50 cm^{-1} per eV.[7] This dispersion is due to the role of electron-phonon scattering in the D

and 2D bands and the energy conservation requirement for double resonance to occur, and it mirrors the linear dispersion in the iTO phonon band at the K point.

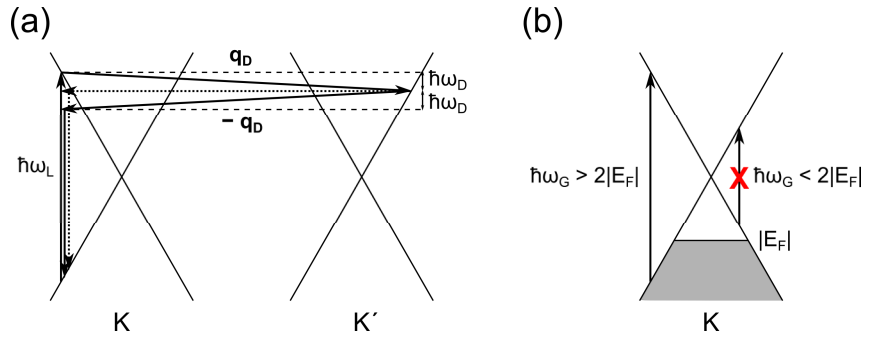

Figure 2.3 (a) Double resonance Raman processes for the graphene D and 2D bands. After an electron-phonon scattering event (solid line from K to K′), scattering from a defect (dotted line from K′ to K) conserves momentum in D band excitation, while a second electron-phonon scattering event (solid line from K′ to K) conserves momentum in 2D band excitation. The incident laser photon energy is $\hbar\omega_L$. (b) Pauli blocking in doped graphene.

The Raman peaks of graphene are highly informative. As mentioned above, the shape of the 2D peak distinguishes single-layer from bilayer graphene, and the D peak is a signature of defects in the sp^2 carbon lattice. The G peak reports on electronic doping of graphene; ω_G shifts and the peak full width at half-maximum (FWHM) decreases with electron or hole doping. These effects are both a result of electron-phonon coupling. G peak phonons have an energy $\hbar\omega_G \approx 0.2$ eV. Graphene has no band gap, and thus a G peak phonon can be annihilated by exciting an electron-hole pair with energy approximately equal to $\hbar\omega_G$. When the electron and hole recombine, a phonon is emitted with a slightly different energy, $\Delta\hbar\omega_G$. An expression for this energy difference can be

derived using second-order perturbation theory. Importantly, $\Delta\hbar\omega_G$ is a function of the Fermi level of graphene; as the Fermi level shifts from the Dirac point, the excitation of electron-hole pairs of energy < $2|E_F|$ is forbidden by the Pauli exclusion principle (Figure 2.3b). Because the expression for $\Delta\hbar\omega_G$ involves a sum over all possible electronic transitions, a change in the allowed transitions leads to a change in $\Delta\hbar\omega_G$. For low doping, where $|E_F| < 0.1$ eV, the G peak shifts to lower frequencies, but this can only be resolved at low temperatures. For higher doping levels, the G peak upshifts. This shift in the G peak frequency as a function of doping has been calibrated in field-effect transistor graphene devices, where E_F can be tuned over a range of values. The decrease in the G peak FWHM with increasing doping is also a consequence of electron-phonon coupling. Pauli blocking of electron-hole pair excitations increases the lifetime of G peak phonons, and thus the G peak FWHM decreases monotonically with increasing doping.

2.2.2 Reflective Contrast Spectroscopy

Reflective contrast spectroscopy is proving to be another valuable optical technique for graphene characterization. Unlike Raman spectroscopy, which is most reliable for the identification of single-layer and bilayer graphene, contrast spectroscopy is a robust method for distinguishing flakes of up to 10 layers or more. As a probe of absorbance, reflective contrast spectroscopy can also provide fundamental information about the electronic and optical properties of single- and few-layer graphene.[10-14]

The optical response of thin films on a dielectric substrate can be characterized by measurement of the fractional change of reflectance, δ_R:

$$\delta_R = \frac{R_f - R_s}{R_s} \qquad 2.5$$

where R_f and R_s are the film and substrate reflectance, respectively. In what follows we refer to the quantity δ_R as the contrast. A special relationship can be derived for a thin film of thickness $d \ll \lambda_0$, where λ_0 is the free space wavelength of light, supported on a transparent substrate. In this case, the contrast is directly related to the film absorbance A by:

$$\delta_R = \frac{4}{n_s^{\,2} - 1} A \tag{2.6}$$

where n_s is the refractive index of the substrate.[12,15] The absorbance A in Equation 2.6 is proportional to the real part of the thin film optical sheet conductivity, $\sigma_{2D}^{(1)}$:

$$A = \frac{4\pi}{c} \sigma_{2D}^{(1)} \tag{2.7}$$

where c is the speed of light in vacuum.[12] In the case of graphene, where coupling between layers is relatively weak, the optical sheet conductivity σ_{2D} can be treated as the product of the 3D optical conductivity, σ_{3D}, and the film thickness, d. Then the real parts of σ_{2D} and σ_{3D} are related by:

$$\sigma_{2D}^{(1)} = \sigma_{3D}^{(1)} d \tag{2.8}$$

The real part of the optical conductivity, in turn, is related to the imaginary part of the dielectric constant, ε_2:

$$\sigma_{3D}^{(1)} = \frac{\omega}{4\pi} \varepsilon_2 \tag{2.9}$$

where $\varepsilon = \varepsilon_1 - i\varepsilon_2$ and ω is the angular frequency of the incident photon.[16] Combining Equations 2.7 through 2.9 gives a relationship for the film absorbance in terms of the imaginary part of the dielectric constant, the frequency of the light, the thickness of the film, and the speed of light:

$$A = \frac{\omega d}{c}\varepsilon_2 \qquad 2.10$$

It should be noted that the absorbance A in this discussion is not the same as the quantity that appears in the Beer-Lambert law:

$$A' = \frac{4\pi k}{\lambda_0} d \qquad 2.11$$

where k is the imaginary part of the complex index of refraction, $\tilde{n} = n - ik$.[16] Substitution of $\varepsilon_2 = 2nk$ and $\omega = 2\pi c/\lambda_0$ into Equation 2.10 gives:

$$A = \frac{4\pi k}{\lambda_0} nd \qquad 2.12$$

Thus the absorbance related to δ_R is a factor of n larger than the absorbance in the Beer-Lambert law. This difference arises from the geometries of the two cases. The Beer-Lambert law applies to a bulk homogeneous medium with $d \gg \lambda_0$, where the electric field of the incident light wave is not affected by changes in the dielectric constant at an interface between two materials. In this case, absorbance is related only to the imaginary part of the index of refraction, k. For a thin film on a substrate, however, the incident light wave is modified by the dielectric constant of the material, and the real part of the index of refraction, n, enters the expression for absorbance.

The reflective contrast of graphene on a quartz substrate has been reported for photon energies from 0.2 – 5.3 eV.[12,14] In the near-IR spectral region, corresponding to photon energies from 0.5 – 1.2 eV, the contrast of single-layer graphene is nearly frequency-independent and has a value of $\delta_R \approx 0.09$. This contrast corresponds to a universal sheet conductivity $\sigma_{2D}^{(1)}$ given by the expression:

$$\sigma_{2D}^{(1)} = \frac{\pi G_0}{4} \text{ where } G_0 = \frac{2e^2}{h} \qquad 2.13$$

where G_0 is the quantum of conductance, e is the electron charge, and h is Planck's constant. This frequency-independent conductivity is a property of massless Dirac fermions, and universal values for the graphene transmittance T and reflectance R can be derived from it:

$$T = \frac{1}{(1+\pi\alpha)^2} \qquad 2.14a$$

$$R = \frac{1}{4}\pi^2\alpha^2 T \qquad 2.14b$$

where $\alpha = e^2/\hbar c$ is the fine structure constant.[17] From these expressions, the graphene absorbance $A = 1 - (R + T)$ can be calculated. Neglecting R, which is small for a single graphene layer, and expanding T in a Taylor series gives $A \approx 1 - T \approx \pi\alpha \approx 0.023$. From this analysis comes the often-quoted absorbance of a single layer of graphene, approximately 2.3% of the incident light. This absorbance in the visible spectral range has been directly measured for suspended graphene in transmission geometry. For lower photon energies, the graphene contrast (or conductivity) deviates from its universal value due to the effects of doping and intraband scattering processes; in the 0.2 – 0.5 eV spectral region, the contrast increases with frequency.[12] In the UV-visible spectral region, likewise, the graphene contrast rises smoothly with increasing photon energy until it reaches a maximum at approximately 4.6 eV. This resonance is assigned to transitions near the M point in the graphene Brillouin zone, where there is a saddle-point singularity in the band structure.[14]

The equations above and later in this chapter are written in Gaussian electromagnetic units. The quantities σ_{2D} and c are in meters·second^{-1}, σ_{3D} and ω are in second^{-1}, and d is in meters. A, δ_R, n, and ε are unitless.

2.3 GERS and Fluorescence Quenching

As a two-dimensional material, graphene is extremely sensitive to its environment. Indeed, molecular adsorption has been shown to change the electronic and optical properties of single- and few-layer graphene. Although many studies have focused on using molecular adsorption to tune the properties of graphene, the interaction with graphene likewise affects molecular properties. Xie *et al.* reported fluorescence quenching for the dye molecules rhodamine 6G (R6G) and protoporphyrin IX adsorbed on graphene, with the fluorescence quenched by a factor of approximately 1,000.[18] Chen *et al.* demonstrated fluorescence quenching of CdSe/ZnS core-shell quantum dots (QDs) deposited on single- and few-layer graphene and estimated a Förster energy transfer rate of 4 ns^{-1} for QDs on single-layer graphene.[19] Förster energy transfer to metals or semimetals, like graphene, occurs by the excitation of electron-hole pairs, and the broad absorption spectrum of graphene means that energy transfer can occur resonantly across a wide spectral range. The rate of Förster energy transfer between two molecules has a distance dependence of d^{-6}, reflecting the dipole-dipole interaction. For single-layer graphene, however, a dependence of d^{-4} has been predicted for all but short dipole-graphene distances.[20,21] Thus quenching of excited dipoles a significant distance from graphene, up to 30 nm, may be possible. Fluorescence quenching by charge transfer to

graphene is also possible, although no evidence in support of that mechanism was found in the case of QDs.[19]

Recently there have been several reports of enhanced Raman scattering from dye molecules adsorbed on graphene or graphene oxide.[22-28] Ling *et al.* reported an enhancement in the Raman signals of several dyes, including R6G, adsorbed on graphene in comparison to Si/SiO_2.[21] The observed R6G Raman peaks are about as intense as the prominent graphene G peak at 1580 cm^{-1}. The Raman enhancement factor for phthalocyanine on single-layer graphene ranged from 2 – 17, depending on the vibrational mode, and was lower for few-layer or multilayer graphene. This enhancement was attributed to charge transfer between graphene and the adsorbates. Qiu *et al.* reported a similar thickness-dependence in the Raman intensity of crystal violet (CV) deposited on graphene by solution soaking.[25] These authors proposed that a chemical effect, rather than an electromagnetic effect, explained the observed Raman enhancement and graphene thickness dependence, but a detailed mechanism was not determined. (See Chapter 1.2 for a discussion of SERS enhancement mechanisms.)

Here we use optical contrast spectroscopy to observe the electronic absorption of R6G adsorbed on graphene, which itself is supported on a quartz substrate. In this study, we find that the R6G absorbance is shifted to lower energy by its interaction with graphene. We also observe the spectral signature of R6G aggregates that form at higher concentration. By combining the quantitative contrast measurements with Raman spectroscopy, we estimate that the Raman scattering cross-section of adsorbed R6G is reduced by a factor of three from its solution phase value. In this case, there is no evidence for a GERS enhancement. Although there have been a few studies of the

absorption of molecules adsorbed on graphene or graphene oxide in solution-phase suspensions or solution-deposited films,[29-31] and one recent qualitative report of the contrast of R6G adsorbed on single-layer graphene,[32] this is to our knowledge the first report of optical contrast spectroscopy as a quantitative tool to characterize molecular adsorbates on exfoliated graphene flakes.

2.4 Experimental Methods

In all experiments, graphene was deposited onto quartz substrates (SPI Supplies) from Kish graphite (Covalent Materials, grade B) using the Scotch tape micromechanical exfoliation method. Briefly, quartz substrates were cleaned by immersion in piranha solution (a 3:1 mix of 96% H_2SO_4 and 30% H_2O_2) for several hours, then rinsed thoroughly with deionized water (resistivity 17.8 – 18.2 MΩ·cm) and dried with N_2. A Kish graphite flake was placed on a piece of Scotch tape and repeatedly peeled until a dense film of light grey flakes was visible on the tape. Quartz substrates were then pressed on the tape and rubbed gently with Teflon tweezers for approximately ten minutes to transfer material from the tape. The tape was removed and the substrates were inspected in an optical microscope to identify graphene flakes.

Rhodamine 6G·HCl (99%) was obtained from Sigma-Aldrich and used without further purification. Graphene samples were immersed in aqueous R6G solutions with concentrations from 10^{-7} M to 10^{-3} M for 30 min, rinsed with deionized water from a wash bottle for 30 s to remove loosely-bound molecules, and then dried with N_2 gas.

Optical contrast spectroscopy was performed in a backscattering geometry in an inverted microscope (Nikon TE300) with a 40× (0.60 NA) objective using 100 W quartz-

tungsten-halogen lamp (Oriel) light focused to a spot of approximately 2 μm in diameter at the sample. Before entering the microscope, the lamp light was passed through a 100 μm pinhole, collimated by an achromatic lens (f = 300 mm), and then cut back by an iris to minimize chromatic aberrations. Light exiting the microscope was dispersed by a 0.27 m monochromator (Spex 270M) with a reflective ruled grating (150 grooves/mm) and imaged on a 512 × 512 pixel liquid N_2-cooled CCD detector (Princeton Instruments). The reflectance was measured at a spot on the sample and at a nearby spot on the substrate and the contrast was calculated according to Equation 2.5. For each measurement, spectra were taken at three separate grating positions and stitched together to give an effective spectral range of about 400 – 850 nm. Background spectra at each grating position were recorded by blocking the light before it entered the microscope. Background spectra were recorded for every measurement. For scans at the long-wavelength grating position, a 650 nm long-pass filter was inserted before the spectrometer to prevent the second-order diffraction of short-wavelength light. A holmium perchlorate solution (Sigma-Aldrich) was used for wavelength calibration, and the spectral resolution was approximately 1 nm.

To obtain the contrast spectrum of R6G on the quartz substrate, a bare quartz reference slide was positioned adjacent to the sample. The reference spot was approximately 800 μm away from the measured spot on the sample. This procedure introduces more error than using a nearby reference spot, but it can be used to reproduce the contrast spectrum of a bare graphene flake with a variation of approximately 10 – 20%.

Raman spectroscopy was performed in a backscattering geometry with 2.0 mW of 514.5 nm Ar^+ laser (Coherent Innova 300) excitation focused to a spot size of approximately 1 μm^2 at the sample. The same objective, monochromator, and detector were used as for the contrast measurements, but with a 1200 grooves/mm grating. Hg(Ar) and Ne pen lamps (Oriel) were used for wavenumber calibration. The lamp peaks were fit to Gaussian functions to determine the spectral resolution.

2.5 Data Analysis and Computational Methods

2.5.1 Reflective Contrast Spectroscopy

For the graphene-R6G system, we make the simplifying assumption that the overall sheet conductivity can be treated as the sum of the conductivities of the graphene flake and the R6G film. Then we can write Equation 2.7 as:

$$A = A_G + A_{R6G} = \frac{4\pi}{c}(\sigma^{(1)}_{2D,G} + \sigma^{(1)}_{2D,R6G}) \tag{2.15}$$

Or, from Equation 2.10:

$$A = \frac{\omega}{c}(d_G\varepsilon_{2,G} + d_{R6G}\varepsilon_{2,R6G}) \tag{2.16}$$

Likewise, we can rewrite Equation 2.6 in terms of the contrast of graphene and R6G, $\delta_{R,G}$ and $\delta_{R,R6G}$:

$$\delta_R = \delta_{R,G} + \delta_{R,R6G} = \frac{4}{n_s^{\,2} - 1}(A_G + A_{R6G}) \tag{2.17}$$

where n_s is the index of refraction of the substrate. Finally, we obtain the relationship for the absorbance and contrast of R6G alone:

$$A_{R6G} = \frac{\omega d}{c}\varepsilon_{2,R6G} = \frac{n_s^{\,2} - 1}{4}\delta_{R,R6G} \qquad 2.18$$

2.5.2 Interference Model for Graphene and R6G Raman Intensities

The graphene G peak Raman intensity as a function of number of layers, *N*, is calculated following methods adapted from Yoon *et al.*[33] by Jung *et al.*[34] We adapt the equations for graphene on a quartz substrate, without (Figure 2.4a) or with (Figure 2.4b) a thin film of R6G above the graphene.

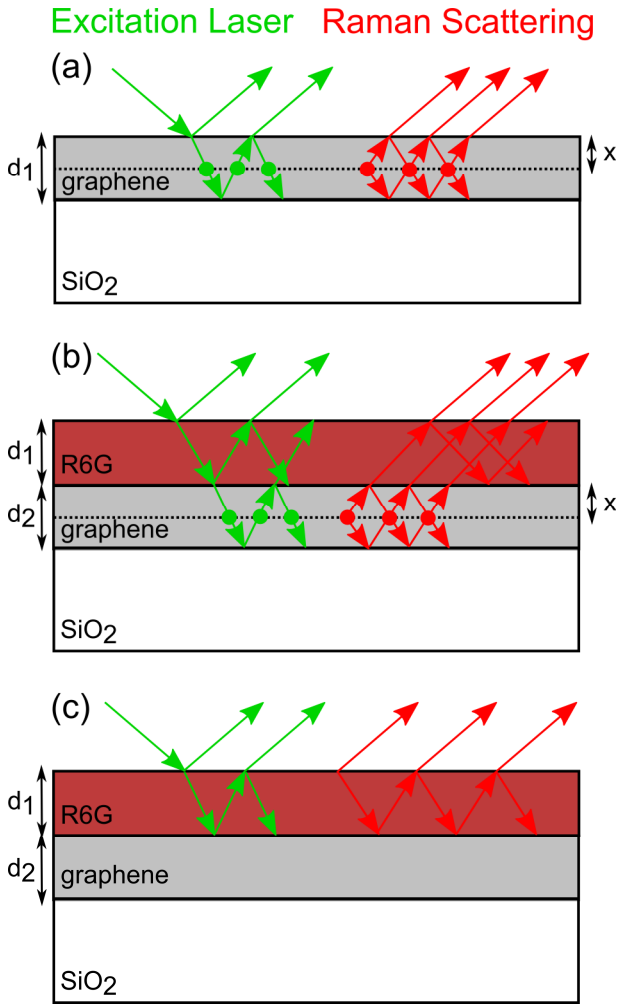

Figure 2.4 Schematic of the multiple reflection interference effects in multilayer films of graphene and R6G on a quartz substrate. The green arrows represent the excitation laser light and the red arrows represent the Raman-scattered light. (a) Interference effects contributing to the graphene G peak Raman intensity for graphene on quartz. (b) Same as (a) but with an adsorbed R6G layer. (c) Interference effects contributing to the Raman intensity of R6G adsorbed on graphene. Note that the excitation laser light is shown at non-normal incidence for clarity, but all calculations assume normal incidence.

The Raman intensity relative to the intrinsic Raman scattering cross-section is given by:

$$I(N) = \int_0^{d(N)} \left| F_{ab}(x,N) F_{sc}(x,N) \right|^2 dx \qquad 2.19$$

where $d(N) = 0.335N$ is the thickness of the graphene layer. $F_{ab}(x, N)$ and $F_{sc}(x, N)$ are the enhancement factors for the incident laser and the Raman scattered light respectively at a depth x in the graphene film, which are integrated over the film thickness to give the total signal.

For graphene without R6G, the enhancement factors are given by:

$$F_{ab}(x,N) = t_{01} \frac{e^{-i\beta x} + r_{12} e^{-i(2\beta_1 - \beta_x)}}{1 + r_{01} r_{12} e^{-2i\beta_1}} \qquad 2.20a$$

$$F_{sc}(x,N) = t_{10} \frac{e^{-i\beta x} + r_{12} e^{-i(2\beta_1 - \beta_x)}}{1 + r_{01} r_{12} e^{-2i\beta_1}} \qquad 2.20b$$

where $r_{yz} = \frac{n_y - n_z}{n_y + n_z}$ and $t_{yz} = \frac{2n_y}{n_y + n_z}$ for $|y - z| = 1$, $\beta_y = \frac{2\pi n_y d_y}{\lambda_0}$, $\beta_x = \frac{2\pi n_1 x}{\lambda_0}$, and λ_0 is the vacuum wavelength of the incident or scattered light.

For graphene with R6G, the enhancement factors are:

$$F_{ab}(x,N) = \frac{t_{01} t_{12} e^{-i\beta_1}}{1 + r_{01} r_{12} e^{-2i\beta_1}} \frac{e^{-i\beta x} + r_{23} e^{-i(2\beta_2 - \beta_x)}}{1 + r_{23} \left(\frac{r_{12} + r_{01} e^{-2i\beta_1}}{1 + r_{01} r_{12} e^{-2i\beta_1}} \right) e^{-2i\beta_2}} \qquad 2.21a$$

$$F_{sc}(x,N) = \frac{t_{10} t_{21} e^{-i\beta_1}}{1 + r_{01} r_{12} e^{-2i\beta_1}} \frac{e^{-i\beta x} + r_{23} e^{-i(2\beta_2 - \beta_x)}}{1 + r_{23} \left(\frac{r_{12} + r_{01} e^{-2i\beta_1}}{1 + r_{01} r_{12} e^{-2i\beta_1}} \right) e^{-2i\beta_2}} \qquad 2.21b$$

where $\beta_x = \frac{2\pi n_2 x}{\lambda_0}$.

To calculate the adsorbed R6G Raman intensity as a function of number of graphene layers, we again model the enhancement of the incident and Raman scattered light by reflection at the multilayer film interface (Figure 2.4c). In this case, however, we do not integrate the Raman signal over the R6G layer because the film thickness is small and fixed and there will be little variation in the Raman intensity. Instead, we calculate the enhancement at the R6G film surface. The Raman signal intensity is then:

$$I(N) = F_{ab}(N)F_{sc}(N) \tag{2.22}$$

with enhancement factors given by:

$$F_{ab}(N) = \left|1 + r_{03}(N)\right|^2 \tag{2.23a}$$

$$F_{sc}(N) = \left|1 + r_{03}(N)\right|^2 \tag{2.23b}$$

Here, $r_{03}(N)$ is the reflection coefficient for the multilayer film:

$$r_{03}(N) = \frac{r_{01}e^{i\beta_1}(e^{i\beta_2(N)} + r_{12}r_{23}e^{-i\beta_2(N)}) + e^{-i\beta_1}(r_{12}e^{i\beta_2(N)} + r_{23}e^{-i\beta_2(N)})}{e^{i\beta_1}(e^{i\beta_2(N)} + r_{12}r_{23}e^{-i\beta_2(N)}) + r_{01}e^{-i\beta_1}(r_{12}e^{i\beta_2(N)} + r_{23}e^{-i\beta_2(N)})} \tag{2.24}$$

In all calculations, we assume normal incidence of the excitation laser beam on the multilayer film. Calculation parameters are shown in Table 2.1.

Graphene G Peak			**Graphene G Peak with R6G**			**R6G on Graphene**		
d_1 (nm)	0.335·N	graphene	d_1 (nm)	0.5	R6G	d_1 (nm)	0.5	R6G
—	—	—	d_2 (nm)	0.335·N	graphene	d_2 (nm)	0.335·N	graphene
	Incident	Scattered		Incident	Scattered		Incident	Scattered
λ (nm)	514.531	560.124	λ (nm)	514.531	560.124	λ (nm)	514.531	562.266
n_0 (vac)	1	1	n_0 (vac)	1	1	n_0 (vac)	1	1
$\tilde{n}_1$ (gr)	$2.711 - 1.350i$	$2.730 - 1.386i$	$\tilde{n}_1$ (R6G)	$1.909 - 0.617i$	$2.047 - 0.603i$	$\tilde{n}_1$ (R6G)	$1.909 - 0.617i$	$2.000 - 0.547i$
n_2 (SiO_2)	1.46	1.46	$\tilde{n}_2$ (gr)	$2.711 - 1.350i$	$2.730 - 1.386i$	$\tilde{n}_2$ (gr)	$2.711 - 1.350i$	$2.731 - 1.388i$
—	—	—	n_3 (SiO_2)	1.46	1.46	n_3 (SiO_2)	1.46	1.46

Table 2.1 Parameters used in Raman interference model calculations.

2.5.3 Estimate of R6G Photobleaching

Two independent estimates of the R6G photobleaching were made. In a typical Raman measurement, three consecutive integrations of five minutes each were performed at the same spot. The total intensity (Raman plus fluorescence) was assumed to decay exponentially, and the signal was fit to a function of the form:

$$I = A + Be^{-\frac{t}{\tau}} \tag{2.25}$$

where t is time, τ is the time constant of the exponential decay, and A and B are constants. From this calculation, we estimated that the instantaneous signal at time t = 15 min was approximately 6-fold smaller than the signal at t = 0. Using the values obtained for τ, A, and B, we integrated this exponentially decaying signal over 15 minutes and compared it to the signal that would be obtained over the same time period if the t = 0 intensity did

not decay. From this calculation, we estimated that the photobleaching reduced the total intensity by a factor of approximately 3.5.

As an independent check of this estimate, we monitored the total Raman and fluorescence signal at 5 s intervals and fit the resulting decay to an exponential function. The time constant τ obtained by this method was in reasonable agreement with the value calculated following the procedure above.

2.6 Results and Discussion

Figure 2.5a shows the optical contrast spectrum of a bilayer graphene flake on a quartz substrate before and after exposure to R6G. The contrast of pristine graphene rises monotonically with decreasing wavelength, but it is otherwise featureless over the 425 – 800 nm spectral range of the measurement.[14] After the flake is immersed in a 100 nM R6G solution, a peak appears at approximately 538 nm. A contrast difference spectrum can be generated by subtracting the pristine graphene contrast (Figure 2.5b). The UV-vis spectrum of a 10 μM aqueous solution of R6G is shown for comparison in Figure 2.6a, plotted against photon energy (in eV). R6G has a strong absorbance peak at 2.35 eV (529 nm) arising from the $S_0 \rightarrow S_1$ electronic transition, with a vibronic shoulder on the high-energy side of the main peak. The vibronic shoulder can be fit to a single broad Gaussian centered at 2.47 eV (503 nm), but it is believed to reflect transitions involving multiple vibrational modes of the molecule.[35] The contrast difference spectrum shown in Figure 2.5b is plotted against photon energy in Figure 2.6b. Although the spectrum of adsorbed R6G is shifted to lower energy, it has a similar shape to the solution absorbance spectrum. An additional minor Gaussian component is present on the low energy end of

the spectrum. Further insight can be obtained by depositing R6G from a more concentrated solution. Figure 2.6c shows the contrast difference spectrum of a bilayer graphene flake exposed to a 1 mM R6G solution. The absorbance maximum is shifted to 2.18 eV (568 nm) and the integrated peak area increases by 49%, reflecting a higher surface concentration of the dye.

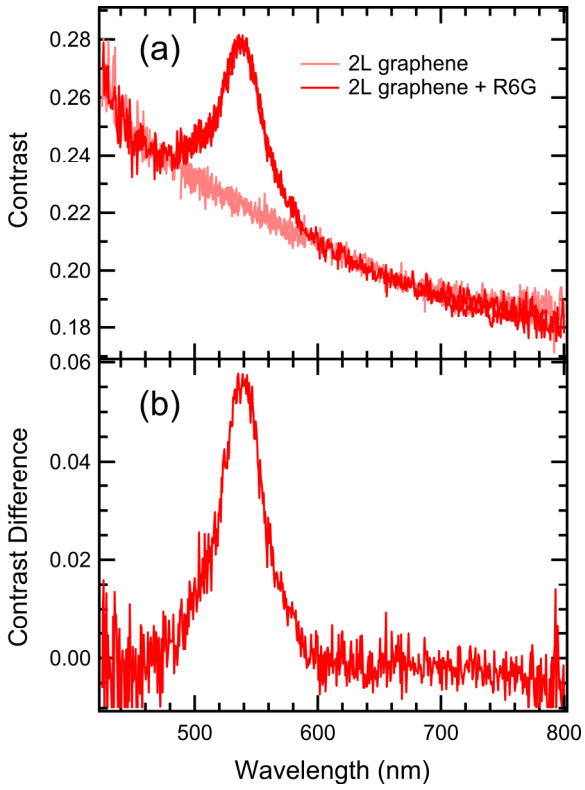

Figure 2.5 (a) Contrast spectrum of a bilayer graphene flake before (pink line) and after (red line) immersion in a 100 nM aqueous solution of R6G. (b) Contrast difference spectrum of the data shown in (a).

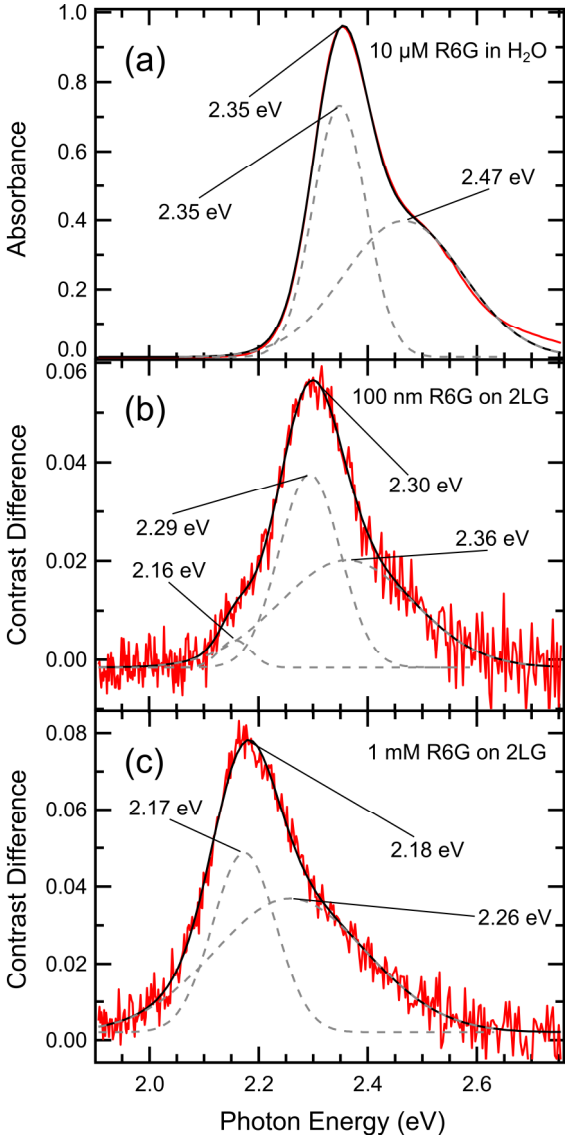

Figure 2.6 (a) Absorbance spectrum (red line) of a 10 μM aqueous solution of R6G. The spectrum is fit to a sum (black line) of individual Gaussian peaks (grey dashed lines). (b) Contrast difference spectrum (red line) of a bilayer graphene flake after immersion in a 100 nM aqueous solution of R6G, and corresponding fits. (c) Contrast difference spectrum of a bilayer graphene flake after immersion in a 1 mM aqueous solution of R6G, and corresponding fits.

The spectral shift may be explained by the formation of molecular aggregates, which have been studied extensively for R6G in solution, on surfaces, and intercalated in porous materials.[36-39] Molecular exciton theory qualitatively describes the spectral changes resulting from dye aggregation.[40] The dimer absorption can shift to higher or lower energy, depending on the relative orientation of the monomers, or band-splitting may occur, leading to transitions at both higher and lower energy. Two special cases are head-to-tail dimers (J-aggregates) and parallel dimers (H-aggregates), with lower and higher transition energies, respectively. The molecular structure of R6G is shown in Figure 2.7a, and schematics of the H- and J-aggregates are shown in Figure 2.7b and Figure 2.7c. The planes of the xanthene ring and the carboxyphenyl ring are oriented at an angle of approximately 90°.[41,42] If the molecule adsorbs with the xanthene ring parallel to the graphene surface, consistent with results from Raman spectroscopy (see below), we would expect J-aggregate formation and a shift in the main absorbance peak to lower energy.

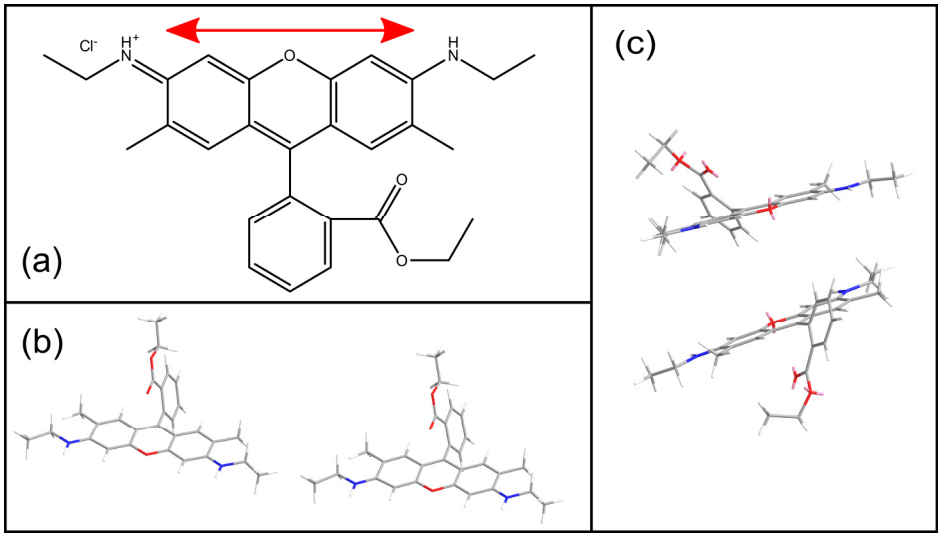

Figure 2.7 (a) Molecular structure of R6G. The $S_0 \rightarrow S_1$ transition dipole moment, along the long axis of the xanthene ring, is indicated by the red arrow. Schematics of the orientation of R6G monomers in (b) a J-aggregate (head-to-tail dipole moments) and (c) an H-aggregate (parallel dipole moments).

Although we cannot make an unequivocal assignment of the different R6G species contributing to the contrast spectra, we note some similarities to the absorbance spectra reported by Zhao *et al.* for R6G adsorbed on Ag films.[39] From deconvolutions of the R6G absorbance spectra, they assigned a peak at 539 nm (2.30 eV) to monomeric R6G and a peak at 570 nm (2.18 eV) to J-aggregates, in good agreement with the fits shown in Figure 2.6b and Figure 2.6c. Additionally, an electronic interaction between R6G and graphene might explain the overall shift in the spectra to lower energies. Studies of R6G solvatochromism have shown that the absorbance maximum in different solvents can shift by 10 nm or more from the position in aqueous solution.[43,44] A conformational change of R6G upon graphene adsorption might also shift the molecular absorbance. Zhao *et al.* used TD-DFT to calculate the effect of a change in the dihedral

angle between the xanthene and phenyl ring planes on the $S_0 \rightarrow S_1$ transition energy of R6G in vacuum.[39] From their calculations, a dihedral angle decrease of 10° would cause the transition to shift to longer wavelengths by approximately 10 nm. Regardless of what causes the overall spectral shift to lower energies, the interpretation of Zhao *et al.* would assign the peak at approximately 2.17 eV in the R6G contrast spectra in Figure 2.6b and Figure 2.6c to J-aggregates, and the higher energy components to monomer-like adsorbed R6G as well as the $S_0 \rightarrow S_1$ vibronic tail.

In addition to providing qualitative information about the state of the adsorbed R6G, the contrast spectra allow us to calculate the thickness of the adsorbed R6G films. A more detailed discussion of these relationships is given in Chapter 2.5.1. We use the final result from that analysis, Equation 2.18:

$$A_{R6G} = \frac{\omega d}{c}\varepsilon_2 = \frac{n_s^{\,2} - 1}{4}\delta_{R,R6G} \qquad 2.18$$

to estimate the absorbance and contrast of a monolayer of R6G. The optical constants of R6G films on glass substrates have been determined from reflectance and transmission measurements.[45,46] Penzkofer *et al.*[46] reported values of $\tilde{n} = n - ik$ for an R6G film deposited by spin-coating on fused silica. The structure in their refractive index spectra indicated the presence of R6G aggregates. Using the R6G refractive index reported by Penzkofer *et al.*, we can calculate the imaginary part of the dielectric constant, $\varepsilon_2 = 2nk$. At 540 nm, $\tilde{n} = 2.03 - 0.690i$ and thus $\varepsilon_2 = 2.80$. Iyi *et al.* used a semiempirical molecular dynamics program to calculate the dimensions of R6G.[47] They found an effective molecular thickness of $d = 0.5 - 0.85$ nm, in comparison to the long-axis length of 1.4 nm. For $d = 0.5$ nm, Equation 2.18 yields $A = 1.6\%$. This absorbance can be converted to a contrast value, again using Equation 2.18. With the index of refraction of

SiO_2 as $n_s = 1.46$,[48] we find $\delta_R = 0.058$ for a monolayer of R6G at 540 nm. From this calculation, we estimate that the R6G coverage for the bilayer graphene flake shown in Figure 2.6b is approximately one monolayer.

We can follow a similar analysis for the R6G film deposited from 1 mM solution (Figure 2.6c). Again using refractive index data from Penzkofer *et al.*, $\tilde{n} = 2.01 - 0.687i$ at 568 nm and $\varepsilon_2 = 2.76$. If we take the thickness of a monolayer of R6G J-aggregates to be 0.5 nm, we find $A = 1.5\%$ and $\delta_R = 0.054$. We conclude that the R6G film in Figure 2.6c represents 1 – 2 monolayers. A summary of the parameters used in these calculations is given in Table 2.2.

[R6G] (M)	**ω (s^{-1})**	**ñ**	**ε_2**	**d (nm)**	**A (%)**	**δ_R (calc.)**	**δ_R (exp.)**
1×10^{-7}	3.49×10^{15}	$2.03 - 0.690i$	2.80	0.5	1.6	0.058	0.058
1×10^{-3}	3.32×10^{15}	$2.01 - 0.687i$	2.76	0.5	1.5	0.054	0.076

Table 2.2 Parameters used in R6G absorbance calculations. *[R6G]* is the solution concentration used to prepare the sample, ω is the photon energy, $\tilde{n}$ is the index of refraction, ε_2 is the complex part of the dielectric constant, d is the film thickness, A is the calculated absorbance, and δ_R is the contrast. Refractive index data are from Penzkofer, *et al.*[46]

In determining the concentration of adsorbed R6G on graphene, we have implicitly assumed that there is no R6G on the substrate. Any reflectance from R6G

adsorbed on the substrate would lead us to underestimate the R6G concentration on graphene. To validate this assumption, we measured the concentration of R6G on the quartz substrate relative to a bare quartz slide, as described in Chapter 2.4. The contrast spectrum of quartz exposed to 1 mM R6G is shown in Figure 2.8. The contrast is small, negative, and close to flat across the 400 – 800 nm spectral range, indicating that the R6G concentration on the quartz substrate is negligible.

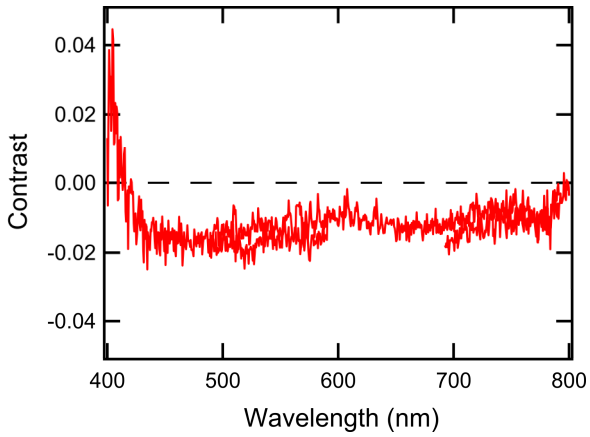

Figure 2.8 Contrast spectrum of a quartz substrate after immersion in a 1 mM aqueous solution of R6G.

Figure 2.9a shows the Raman spectrum, acquired with 514.5 nm argon ion laser excitation, of the same graphene bilayer-R6G sample as in Figure 2.5. This wavelength is resonant with the R6G $S_0 \rightarrow S_1$ transition, and Raman spectra of the molecule in solution cannot be obtained at 514.5 nm excitation under normal conditions because the strong fluorescence background buries the Raman peaks. When R6G is adsorbed on graphene or other carbon materials, however, the fluorescence is partially quenched and the sharp Raman peaks are resolved, as in Figure 2.9a.[18,49,50] The continuous background

of intensity 1500 arbitrary units and larger is residual R6G fluorescence; there is essentially no background without R6G adsorption. The integrated count level in the residual fluorescence is far larger than in the Raman signal.

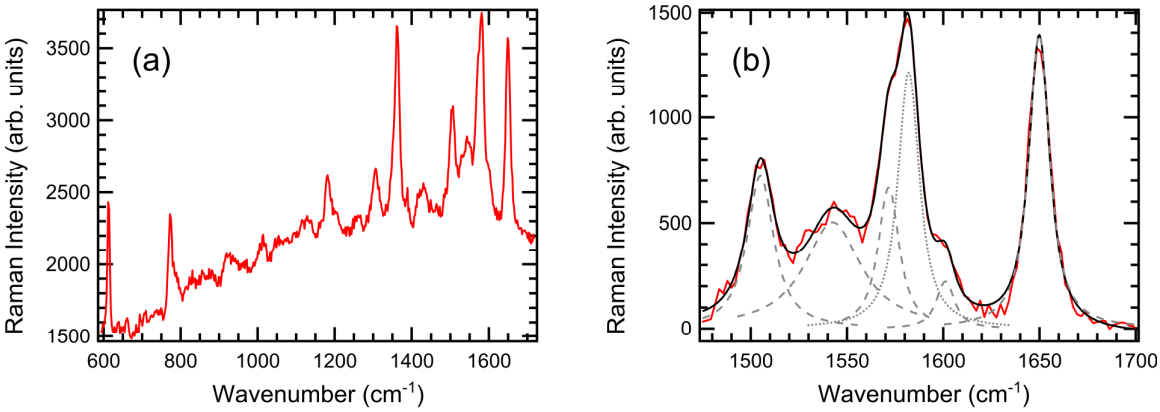

Figure 2.9 (a) Raman spectrum of the same bilayer graphene-R6G sample as in Figure 2.5, obtained at 514.5 nm excitation. (b) Background-subtracted spectrum from (a) in the region of the graphene G peak. The G peak (grey dotted line) and R6G peaks (grey dashed lines) are fit to Voigt functions with Gaussian FWHM = 4.04 cm^{-1}. Also shown is the overall fit (black line).

Table 2.3 gives the positions and literature assignments[41,42,51,52] of the strongest R6G peaks in the Figure 2.9a spectrum. The R6G HOMO and LUMO are predominantly localized in the xanthene ring, with the transition dipole moment oriented parallel to the long axis of the molecule,[52] and thus normal modes involving the xanthene ring are selectively enhanced by resonant excitation.[41,42] Indeed, the strongest Raman peaks in our spectra can be assigned to xanthene ring modes. In a micro-Raman setup such as ours, the electric field of the excitation laser is polarized primarily in the plane of the

surface, with only a small component normal to the surface.[52] If R6G adsorbs on graphene with the xanthene ring parallel to the graphene planes, we would expect only those R6G vibrational modes with significant in-plane components to be present in the Raman spectrum. According to density functional theory (DFT) calculations by Watanabe *et al.* [41] and Jensen *et al.*,[42] the strongest peaks in our spectra correspond primarily to in-plane modes of the xanthene ring.

Position (cm^{-1})	**Assignment**	**Position (cm^{-1})**	**Assignment**
613	ip XRD, op XRD	1505	XRS, C-N stretch, C-H bend, N-H bend
774	op C-H bend, ip XRD	1543	Xanthene mode(s)
1184	ip XRD, C-H bend, N-H bend	1572	XRS, ip N-H bend
1306	ip XRB, N-H bend, CH_2 wag	1601	Phenyl mode
1362	XRS, ip C-H bend	1650	XRS, ip C-H bend

Table 2.3 Strongest R6G Raman peaks from Figure 2.9a and literature assignments. (ip: in-plane; op: out-of-plane; XRD: xanthene ring deformation; XRB: xanthene ring breathing; XRS: xanthene ring stretch)

We can estimate the absolute differential Raman scattering cross-section of R6G adsorbed on graphene using the surface concentration determined from contrast

measurements. Kagan and McCreery used Raman spectroscopy to study the adsorption of several molecules, including R6G, on graphite[49] and glassy carbon.[50] They showed that the Raman scattering cross-section of adsorbed molecules on bulk graphite could be calculated using the carbon substrate G peak as an internal standard. Following their approach, the differential Raman scattering cross-section for a single R6G peak is given by:

$$\beta_{R6G} = \frac{S_{R6G}\beta_G D_G}{S_G D_{R6G}(\alpha_L + \alpha_R)} \qquad 2.26$$

where β_{R6G} and β_G are the differential Raman scattering cross-sections, D_{R6G} and D_G are the concentrations, and S_{R6G} and S_G are the Raman intensities of R6G and graphene, respectively.[50] The finite penetration depth of the incident laser and Raman scattered light in the carbon substrate are accounted for by the penetration depths α_L and α_R. In the case of bulk graphite, where the sample thickness is greater than the penetration depth, α_L and α_R are defined as:

$$\alpha_L = \frac{4\pi k_L}{\lambda_L} \qquad 2.27a$$

$$\alpha_R = \frac{4\pi k_R}{\lambda_R} \qquad 2.27b$$

where k is the imaginary part of the graphite index of refraction at the vacuum wavelengths λ. The graphene sample thickness, however, is smaller than the penetration depth of the light, and α_L and α_R cannot be defined as in Equation 2.27. Nonetheless, we can use Equation 2.26 for graphene if we interpret $(\alpha_L + \alpha_R)^{-1}$ as representing the effective sample depth.

We follow this modified approach to determine the differential Raman scattering cross-section, β_{R6G}, for the 1650 cm^{-1} R6G peak in the Figure 2.9a spectrum. To find the quantity S_{R6G}/S_G, we fit the background-subtracted spectrum to a sum of Voigt functions with a Gaussian full width at half maximum (FWHM) of 4.04 cm^{-1}, reflecting our spectral resolution. The spectrum and the fits in the region of the G peak are shown in Figure 2.9b. The graphene G peak at 1582 cm^{-1} overlaps two R6G peaks at 1572 and 1601 cm^{-1}. The ratio of the integrated areas of the R6G peak at 1650 cm^{-1} to the graphene G peak (S_{R6G}/S_G) is approximately 1.1.

For the quantity $\beta_G D_G(\alpha_L + \alpha_R)^{-1}$, we use values obtained for highly oriented pyrolytic graphite (HOPG). Kagan and McCreery found $\beta_G D_G(\alpha_L + \alpha_R)^{-1} = 3.3 \times 10^{-11}$ sr^{-1} for the G band of HOPG.[50] Wada and Solin separately determined this quantity for HOPG to be 4.3×10^{-11} sr^{-1} or 5.4×10^{-11} sr^{-1}, for two different sets of graphite optical constants.[53] Although it is reasonable to assume that these parameters are similar for graphene and HOPG, it has been demonstrated that optical interference effects must be taken into account when considering the intensity of Raman scattering from graphene on a substrate.[32,54] Multiple reflections within the graphene and substrate layers modulate the intensity of both the incident and Raman-scattered light (Figure 2.4a). As a result, the graphene G peak intensity depends on the substrate, excitation wavelength, and number of graphene layers. These effects can be modeled and the relative Raman intensities for graphene and graphite can be calculated.[34] (Equations and other details are given in Chapter 2.5.2.) Figure 2.10a shows the intensity of the graphene G peak as a function of number of layers, N, for 514.5 nm excitation on a quartz substrate. From this calculation, we find that the G peak intensity of bilayer graphene is 3.8 times smaller than that of

thick graphite at 514.5 nm excitation. Dividing $3.3 – 5.4 \times 10^{-11}$ sr^{-1} by 3.8 gives $\beta_G D_G (\alpha_L + \alpha_R)^{-1} = 0.9 – 1.4 \times 10^{-11}$ sr^{-1} for bilayer graphene.

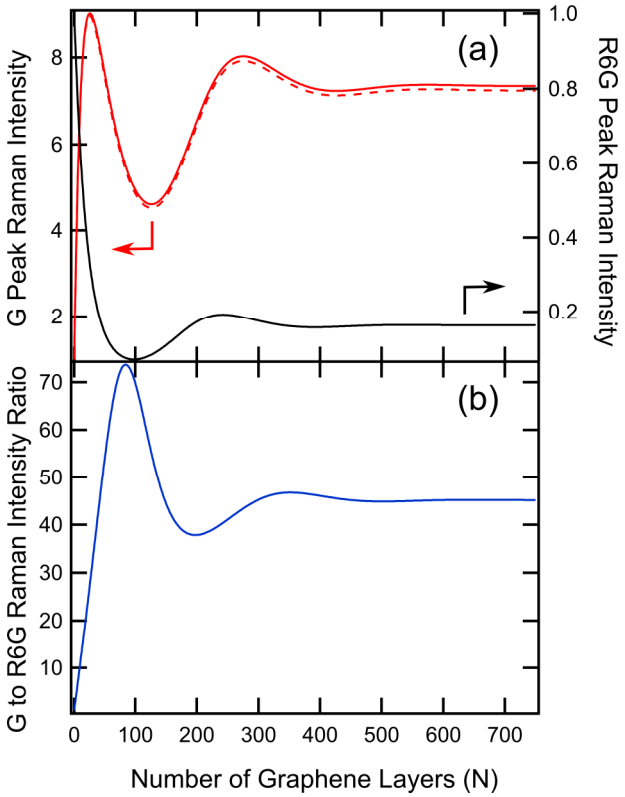

Figure 2.10 (a) Calculated relative Raman intensities for the graphene G peak (red) and R6G 1650 cm^{-1} peak (black) vs. graphene layer number N. The graphene G peak intensity is calculated for bare graphene (dashed line) and graphene with an adsorbed R6G film (solid line). Intensities are normalized to the N = 1 values. The substrate is quartz, the R6G film thickness is fixed at 0.5 nm, and the excitation wavelength is 514.5 nm. (b) Relative G peak to R6G peak Raman intensity ratio, normalized to the N = 1 ratio, calculated from the data (solid lines) in (a).

Finally, we use our contrast measurements to determine the R6G surface concentration D_{R6G}. We have calculated that the R6G coverage for this sample is approximately one monolayer. If we use 1.56 nm^2 as the cross-sectional area of R6G,[47] D_{R6G} is 6.4×10^{13} cm^{-2}. From Equation 2.26, we find $\beta_{R6G} = 1.5 - 2.4 \times 10^{-25}$ $cm^2 \cdot sr^{-1} \cdot molecule^{-1}$. This result agrees well with the cross-section obtained by Kagan and McCreery for R6G adsorbed on glassy carbon at 514.5 nm excitation. They found β_{R6G} to be 4.4×10^{-25} $cm^2 \cdot sr^{-1} \cdot molecule^{-1}$ for the same vibrational mode.[50]

Comparison to the Raman scattering cross-section of R6G in solution indicates that the Raman intensity is reduced when the molecule is adsorbed on graphene. Kagan and McCreery were unable to measure the solution cross-section for R6G due to the strong fluorescent background, but Shim *et al.* used femtosecond stimulated Raman spectroscopy (FSRS) to determine the absolute Raman cross-sections for R6G in methanolic solution at 532 nm excitation.[54] For the peak at 1647 cm^{-1}, corresponding to the 1650 cm^{-1} peak in our spectrum, they reported a cross-section of 2.0×10^{-23} $cm^2 \cdot molecule^{-1}$. They also calculated the Raman excitation profile of this peak and found the cross-section at 514.5 nm excitation was within 10% of the 532 nm value (Figure 2b in Reference 54).

This value is an integrated cross-section, whereas the value of β_{R6G} calculated above is a differential cross-section. We can make a closer comparison by correcting for the finite collection angle in our micro-Raman setup. The geometrical collection efficiency, C_{geom}, of a scattering dipole by an optical element with maximum collection angle θ_{max} is:

$$C_{geom} = \frac{1}{8}\left[4 - 3\cos\theta_{\max} - \cos^3\theta_{\max} + 3\left(\cos^3\theta_{\max} - \cos\theta_{\max}\right)\cos^2\Delta\right] \qquad 2.28$$

where Δ is the angle of the dipole with respect to the optical axis,[55] which is perpendicular to the graphene surface in our setup. With $\theta_{max} = 36.9°$ for our 0.60 NA objective in air and $\Delta = 90°$ for R6G adsorbed flat on graphene, we obtain $C_{geom} = 0.136$. Dividing our calculated differential cross-section for R6G by C_{geom} gives an integrated cross-section of $1.1 - 1.8 \times 10^{-24}$ cm^2·molecule^{-1}, a reduction of an order of magnitude from the solution value for this mode.

As a final correction, we take into account the photobleaching of R6G that occurs under laser excitation.[56] In a solution-phase experiment, molecules that photobleach in the excitation volume will be replaced by molecules from the bulk of the solution. For a dry film of R6G adsorbed on graphene, however, no such exchange occurs. We estimate that over the course of the Raman measurement, the instantaneous R6G fluorescence plus Raman signal decreases by a factor of six, in reasonable agreement with the fluorescence saturation at five-fold lower intensity observed by Xie *et al.*[18] We further estimate that this photobleaching reduces the total R6G signal by a factor of approximately 3.5 when averaged over the duration of the measurement (see Chapter 2.5.3). As a result, the effective R6G concentration is 3.5-fold lower than the value of D_{R6G} used in Equation 2.26, leading to an underestimate of the integrated cross-section by the same factor. Taking into account this photobleaching correction gives a final value for the integrated cross-section of $3.9 - 6.3 \times 10^{-24}$ cm^2·molecule^{-1}. The midpoint value, 5.1×10^{-24} cm^2·molecule^{-1}, represents a greater than three-fold decrease from the cross-section obtained by Shim *et al.* for R6G in methanol.

This reduction in the R6G cross-section is broadly consistent with results obtained by Kagan and McCreery for another resonant molecule, β-carotene, for which the cross-section was reduced by an order of magnitude upon adsorption on glassy carbon. They speculated that electronic interactions between the conjugated molecule and the carbon surface might result in a shift of the β-carotene absorption spectrum, detuning the molecular resonance from the excitation wavelength, but they were unable to measure this shift directly. Our contrast spectra of R6G confirm that the molecular absorption is detuned from the laser wavelength, which is known to reduce the resonance Raman enhancement.[57]

Previous studies of dye molecules adsorbed on graphene found that the adsorbate Raman intensity decreased with increasing graphene thickness.[22,25] The multiple reflection interference model discussed above can be adapted to calculate the adsorbate Raman scattering intensity as a function of number of graphene layers *N* (Figure 2.4c and Chapter 2.5.2).[34] The result of this calculation for the 1650 cm^{-1} mode of a 0.5 nm thick R6G film is plotted in Figure 2.10a, normalized to the Raman intensity calculated for R6G on single-layer graphene. As graphene thickness increases, the R6G Raman intensity decreases until N = 97, rises to a local maximum at N = 242, and ultimately reaches a plateau of approximately 16% of the N = 1 value. We can compare the relative intensity ratio of the graphene G peak to the R6G peak over the same graphene thickness range, normalized to the G peak to R6G peak ratio in single-layer graphene (Figure 2.10b). As the graphene thickness increases, the G peak intensity increases, with some oscillation, and the R6G peak intensity decreases. This is consistent with previous

studies and with our own measurements, which show that the R6G peaks become weaker with increasing graphene thickness (Figure 2.11).

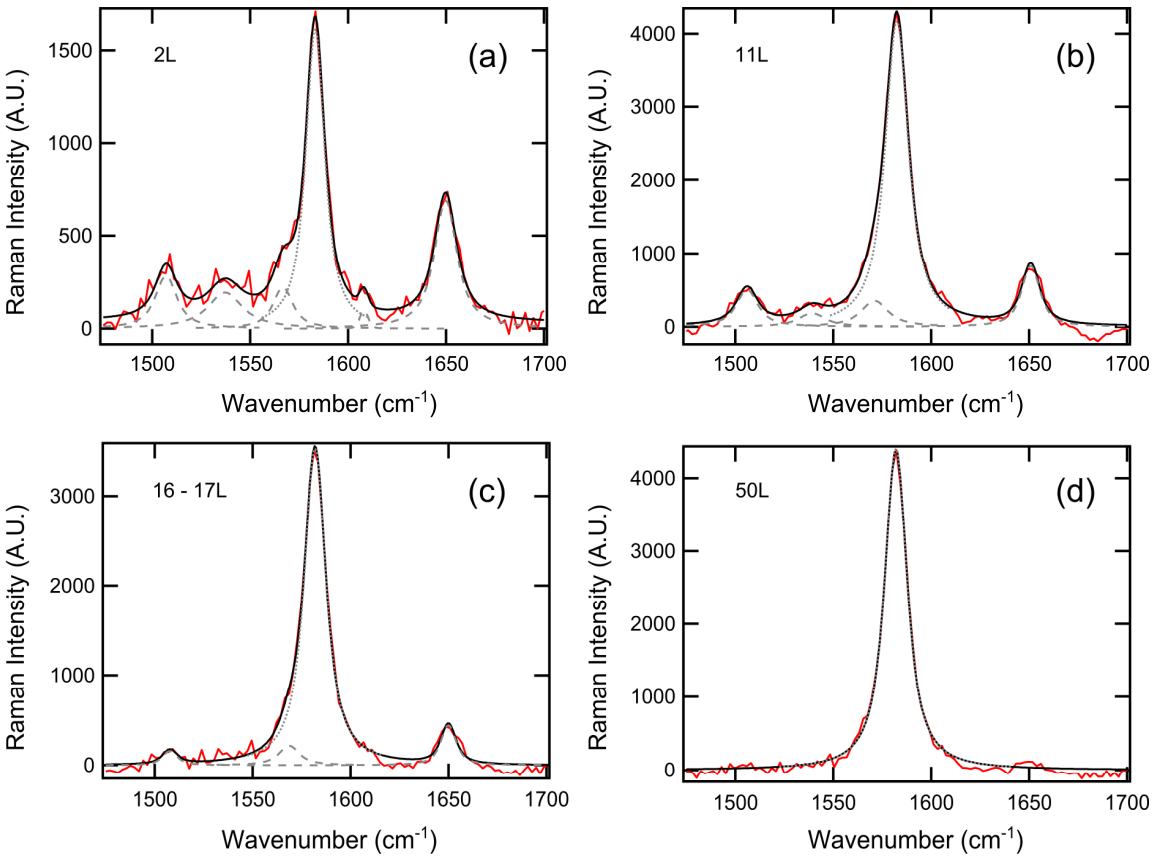

Figure 2.11 Background-subtracted Raman spectra of graphene and graphite flakes after immersion in a 1 mM aqueous solution of R6G shown in the region of the graphene G peak. The G peak (grey dotted line) and R6G peaks (grey dashed lines) are fit to Voigt functions with Gaussian FWHM set by the spectral resolution. The flake thickness and FWHM are (a) bilayer graphene, FWHM = 4.43 cm^{-1}; (b) 11L graphene, FWHM = 4.69 cm^{-1}; (c) ~ 16 – 17L graphene, FWHM = 4.46 cm^{-1}; (d) thick graphene (~ 50L), FWHM = 4.68 cm^{-1}. Thicknesses were determined by contrast spectroscopy, and are only approximate values for the flakes in (c) and (d).

Optical contrast spectroscopy gives us an independent measure of the R6G concentration on graphene, allowing us to draw several conclusions about graphene-enhanced Raman spectroscopy. First, our results confirm that R6G preferentially adsorbs on graphene rather than SiO_2 when deposited from solution, as might be expected for an aromatic molecule. This result is consistent with previous work. Kagan and McCreery found that R6G had a strong affinity for glassy carbon, displaying Langmuirian behavior with a high Langmuir adsorption constant.[50] Ling *et al.*[22] obtained similar results for R6G adsorption on graphene. As further confirmation of the low concentration of R6G on SiO_2, we were unable to measure a contrast signal for R6G deposited on a quartz substrate (see Figure 2.8 and accompanying text).

From the calculations above, we find that the R6G Raman scattering cross-section is reduced from its solution value when the dye is adsorbed on graphene. This result emphasizes the important differences between surface-enhanced Raman spectroscopy (SERS) and what has been termed graphene-enhanced Raman spectroscopy (GERS). For SERS on noble metal nanoparticles or rough surfaces, the majority of the Raman enhancement is due to the excitation of surface plasmons, which concentrates the incident and Raman scattered electromagnetic fields. The SERS cross-section for a single R6G mode under resonant excitation can be on the order of 10^{-15} cm^2,[58] almost one billion times larger than the solution cross-section and large enough to allow single-molecule detection. For R6G adsorbed on graphene, however, the Raman scattering cross-section is reduced from its solution value. There is no significant electromagnetic field enhancement at the graphene surface. This is expected, as the laser polarization is in the plane in the graphene experiment, and perpendicular to the Ag particle surface in the

SERS experiment. Nonetheless, R6G is a strong enough Raman scatterer that the 1000-fold quenching of its fluorescence by graphene, as reported by Xie *et al.*, enables measurement of its Raman spectrum.[18] Raman sensitivity on graphene can be quite high; the resonance Raman spectrum of I_3^- adsorbed on graphene has been observed with a high signal-to-noise ratio at only 3% surface coverage.[59]

Finally, we address the layer-dependence in the Raman intensity of dyes adsorbed on graphene. A multiple reflection model reproduces the trend of decreasing molecular Raman intensity with increasing graphene thickness. These effects are purely optical in nature; no chemical enhancement effects for R6G on single-layer or few-layer graphene are assumed. Some studies have found evidence for a modest chemical enhancement. Qui *et al.* reported a decrease in the Raman intensity of crystal violet from N = 1 to N = 3 that is larger than what our multiple reflection model predicts.[25] Ling *et al.* reported a first-layer effect for Langmuir-Blodgett films of protoporphyrin IX on graphene, where the Raman intensity of the first monolayer of molecules was higher than that of each subsequent layer.[23] Nonetheless, our results confirm that the majority of the graphene layer-dependence seen in the adsorbate Raman scattering intensity is due to optical effects.

2.7 Conclusion

In this study, we have used optical contrast spectroscopy and Raman spectroscopy to characterize R6G adsorbed on graphene. By combining the two techniques, we are able to calculate the Raman scattering cross-section for R6G on bilayer graphene, which we find to be reduced by three-fold from its solution value. We use contrast spectroscopy

to measure the absorbance spectrum of adsorbed R6G, which allows us to calculate the surface concentration and helps explain the decrease in its Raman cross-section. The graphene thickness dependence of R6G Raman intensity can be qualitatively reproduced by a multiple reflection model. Our findings are relevant to recent work on what has been termed graphene-enhanced Raman scattering. We find no evidence for Raman enhancement in this experiment, but the strong quenching of R6G fluorescence allows for sensitive Raman detection nonetheless.

2.8 References

(1) Novoselov, K. S.; Geim, A. K.; Morozov, S. V.; Jiang, D.; Zhang, Y.; Dubonos, S. V.; Grigorieva, I. V.; Firsov, A. A. *Science* **2004**, *306*, 666.

(2) Geim, A. K.; Novoselov, K. S. *Nat Mater* **2007**, *6*, 183.

(3) Castro Neto, A. H.; Guinea, F.; Peres, N. M. R.; Novoselov, K. S.; Geim, A. K. *Rev Mod Phys* **2009**, *81*, 109.

(4) Bolotin, K. I.; Sikes, K. J.; Jiang, Z.; Klima, M.; Fudenberg, G.; Hone, J.; Kim, P.; Stormer, H. L. *Solid State Commun* **2008**, *146*, 351.

(5) Mayorov, A. S.; Gorbachev, R. V.; Morozov, S. V.; Britnell, L.; Jalil, R.; Ponomarenko, L. A.; Blake, P.; Novoselov, K. S.; Watanabe, K.; Taniguchi, T.; Geim, A. K. *Nano Letters* **2011**, *11*, 2396.

(6) Ferrari, A. C.; Meyer, J. C.; Scardaci, V.; Casiraghi, C.; Lazzeri, M.; Mauri, F.; Piscanec, S.; Jiang, D.; Novoselov, K. S.; Roth, S.; Geim, A. K. *Physical Review Letters* **2006**, *97*, 187401.

(7) Ferrari, A. C. *Solid State Commun* **2007**, *143*, 47.

(8) Dresselhaus, M. S.; Jorio, A.; Saito, R. *Annu Rev Conden Ma P* **2010**, *1*, 89.

(9) Dresselhaus, M. S.; Jorio, A.; Hofmann, M.; Dresselhaus, G.; Saito, R. *Nano Letters* **2010**, *10*, 751.

(10) Ni, Z. H.; Wang, H. M.; Kasim, J.; Fan, H. M.; Yu, T.; Wu, Y. H.; Feng, Y. P.; Shen, Z. X. *Nano Letters* **2007**, *7*, 2758.

(11) Wang, F.; Zhang, Y. B.; Tian, C. S.; Girit, C.; Zettl, A.; Crommie, M.; Shen, Y. R. *Science* **2008**, *320*, 206.

(12) Mak, K. F.; Sfeir, M. Y.; Wu, Y.; Lui, C. H.; Misewich, J. A.; Heinz, T. F. *Physical Review Letters* **2008**, *101*, 196405.

(13) Mak, K. F.; Sfeir, M. Y.; Misewich, J. A.; Heinz, T. F. *P Natl Acad Sci USA* **2010**, *107*, 14999.

(14) Mak, K. F.; Shan, J.; Heinz, T. F. *Physical Review Letters* **2011**, *106*, 046401.

(15) McIntyre, J. D.; Aspnes, D. E. *Surface Science* **1971**, *24*, 417.

(16) Dressel, M.; Grüner, G. *Electrodynamics of solids : optical properties of electrons in matter*; Cambridge University Press: Cambridge ; New York, 2002.

(17) Nair, R. R.; Blake, P.; Grigorenko, A. N.; Novoselov, K. S.; Booth, T. J.; Stauber, T.; Peres, N. M. R.; Geim, A. K. *Science* **2008**, *320*, 1308.

(18) Xie, L. M.; Ling, X.; Fang, Y.; Zhang, J.; Liu, Z. F. *Journal of the American Chemical Society* **2009**, *131*, 9890.

(19) Chen, Z. Y.; Berciaud, S.; Nuckolls, C.; Heinz, T. F.; Brus, L. E. *Acs Nano* **2010**, *4*, 2964.

(20) Swathi, R. S.; Sebastian, K. L. *The Journal of Chemical Physics* **2008**, *129*, 054703.

(21) Swathi, R. S.; Sebastian, K. L. *The Journal of Chemical Physics* **2009**, *130*, 086101.

(22) Ling, X.; Xie, L. M.; Fang, Y.; Xu, H.; Zhang, H. L.; Kong, J.; Dresselhaus, M. S.; Zhang, J.; Liu, Z. F. *Nano Letters* **2010**, *10*, 553.

(23) Ling, X.; Zhang, J. *Small* **2010**, *6*, 2020.

(24) Ling, X.; Zhang, J. *Journal of Physical Chemistry C* **2011**, *115*, 2835.

(25) Qiu, C. Y.; Zhou, H. Q.; Yang, H. C.; Chen, M. J.; Guo, Y. J.; Sun, L. F. *Journal of Physical Chemistry C* **2011**, *115*, 10019.

(26) Yu, X. X.; Cai, H. B.; Zhang, W. H.; Li, X. J.; Pan, N.; Luo, Y.; Wang, X. P.; Hou, J. G. *Acs Nano* **2011**, *5*, 952.

(27) Xu, H.; Xie, L. M.; Zhang, H. L.; Zhang, J. *Acs Nano* **2011**, *5*, 5338.

(28) Xu, H.; Chen, Y. B.; Xu, W. G.; Zhang, H. L.; Kong, J.; Dresselhaus, M. S.; Zhang, J. *Small* **2011**, *7*, 2945.

(29) Voggu, R.; Das, B.; Rout, C. S.; Rao, C. N. R. *J Phys-Condens Mat* **2008**, *20*, 472204.

(30) Malig, J.; Jux, N.; Kiessling, D.; Cid, J. J.; Vazquez, P.; Torres, T.; Guldi, D. M. *Angew Chem Int Edit* **2011**, *50*, 3561.

(31) Wojcik, A.; Kamat, P. V. *Acs Nano* **2010**, *4*, 6697.

(32) Wang, Y.; Ni, Z.; Li, A.; Zafar, Z.; Zhang, Y.; Ni, Z.; Qu, S.; Qiu, T.; Yu, T.; Shen, Z. X. *Appl Phys Lett* **2011**, *99*, 233103.

(33) Yoon, D.; Moon, H.; Son, Y. W.; Choi, J. S.; Park, B. H.; Cha, Y. H.; Kim, Y. D.; Cheong, H. *Phys Rev B* **2009**, *80*, 125422.

(34) Jung, N.; Crowther, A. C.; Kim, N.; Kim, P.; Brus, L. *Acs Nano* **2010**, *4*, 7005.

(35) Dieringer, J. A.; Wustholz, K. L.; Masiello, D. J.; Camden, J. P.; Kleinman, S. L.; Schatz, G. C.; Van Duyne, R. P. *Journal of the American Chemical Society* **2009**, *131*, 849.

(36) Reisfeld, R.; Zusman, R.; Cohen, Y.; Eyal, M. *Chemical Physics Letters* **1988**, *147*, 142.

(37) Martinez, V. M.; Arbeloa, F. L.; Prieto, J. B.; Lopez, T. A.; Arbeloa, I. L. *Journal of Physical Chemistry B* **2004**, *108*, 20030.

(38) Bryukhanov, V. V.; Elistratova, S. A.; Laurinas, V. C. *Journal of Applied Spectroscopy* **2003**, *70*, 450.

(39) Zhao, J.; Jensen, L.; Sung, J. H.; Zou, S. L.; Schatz, G. C.; Van Duyne, R. P. *Journal of the American Chemical Society* **2007**, *129*, 7647.

(40) Kasha, M.; Rawls, H. R.; El-Bayoumi, M. A. *Pure and Applied Chemistry* **1965**, *3-4*, 371.

(41) Watanabe, H.; Hayazawa, N.; Inouye, Y.; Kawata, S. *Journal of Physical Chemistry B* **2005**, *109*, 5012.

(42) Jensen, L.; Schatz, G. C. *J Phys Chem A* **2006**, *110*, 5973.

(43) Hinckley, D. A.; Seybold, P. G.; Borris, D. P. *Spectrochim Acta A* **1986**, *42*, 747.

(44) Govindanunny, T.; Sivaram, B. M. *Appl Phys* **1980**, *23*, 253.

(45) Lu, Y.; Penzkofer, A. *Chem Phys* **1986**, *107*, 175.

(46) Penzkofer, A.; Drotleff, E.; Holzer, W. *Opt Commun* **1998**, *158*, 221.

(47) Iyi, N.; Sasai, R.; Fujita, T.; Deguchi, T.; Sota, T.; Arbeloa, F. L.; Kitamura, K. *Appl Clay Sci* **2002**, *22*, 125.

(48) Palik, E. D.; Ghosh, G. *Handbook of optical constants of solids*; Academic Press: San Diego, 1998.

(49) Kagan, M. R.; Mccreery, R. L. *Anal Chem* **1994**, *66*, 4159.

(50) Kagan, M. R.; Mccreery, R. L. *Langmuir* **1995**, *11*, 4041.

(51) Majoube, M.; Henry, M. *Spectrochim Acta A* **1991**, *47*, 1459.

(52) Hildebrandt, P.; Stockburger, M. *Journal of Physical Chemistry* **1984**, *88*, 5935.

(53) Wada, N.; Solin, S. A. *Physica B & C* **1981**, *105*, 353.

(54) Shim, S.; Stuart, C. M.; Mathies, R. A. *Chemphyschem* **2008**, *9*, 697.

(55) Plakhotnik, T.; Moerner, W. E.; Palm, V.; Wild, U. P. *Opt Commun* **1995**, *114*, 83.

(56) Soper, S. A.; Nutter, H. L.; Keller, R. A.; Davis, L. M.; Shera, E. B. *Photochem Photobiol* **1993**, *57*, 972.

(57) Myers, A. B. *J Raman Spectrosc* **1997**, *28*, 389.

(58) Michaels, A. M.; Jiang; Brus, L. *The Journal of Physical Chemistry B* **2000**, *104*, 11965.

(59) Jung, N.; Kim, N.; Jockusch, S.; Turro, N. J.; Kim, P.; Brus, L. *Nano Letters* **2009**, *9*, 4133.

Chapter 3

Optical Studies of the Model Dissimilatory Metal-Reducing Bacterium *Geobacter sulfurreducens*

Here we describe preliminary optical studies of the model dissimilatory metal-reducing bacterium (DMRB) *Geobacter sulfurreducens*. This bacterium couples the oxidation of organic carbon sources to the reduction of iron oxides and other insoluble extracellular electron acceptors, a form of anaerobic respiration that requires the electron transport chain to extend outside the cell. Many questions remain about the mechanisms by which *G. sulfurreducens* and other DMRB transfer electrons to extracellular acceptors. *G. sulfurreducens* produces type IV pili, extracellular protein filaments that some researchers have found to be electrically conductive. It has been proposed that pili act as biological nanowires to transport charge to extracellular electron acceptors. It is also clear that *G. sulfurreducens* produces a variety of *c*-type cytochromes in large concentrations, and it has been demonstrated that these proteins are involved in electron transport. We aim to study electron transport in *G. sulfurreducens* using optical and electrical methods developed to study nanomaterials. This chapter describes the progress we have made in culturing and characterizing *G. sulfurreducens* and the results of preliminary optical experiments. We also discuss future goals for these ongoing studies.

3.1 Introduction to Dissimilatory Metal-Reducing Bacteria

Microorganisms have evolved a variety of mechanisms for generating energy and maintaining cellular redox balance in the absence of oxygen. Fermentation is one approach, where adenosine triphosphate (ATP) is generated through substrate level phosphorylation. Anaerobic respiration is another approach, in which cells ultimately transfer electrons produced in oxidation reactions to an external electron acceptor other than oxygen. As part of respiration, electrons travel along an electron transport chain and a proton motive force is established; this force provides the energy for ATP synthesis in the process of oxidative phosphorylation. Many types of anaerobic respiration have been identified, such as dissimilatory metal reduction, dissimilatory denitrification, sulfur and sulfate reduction, and methanogenesis.[1] This chapter will focus on microorganisms that utilize dissimilatory metal reduction as their primary respiratory mechanism.

In a dissimilatory reduction process, microorganisms transfer electrons to an extracellular species. In contrast to assimilatory reduction processes, where reduction occurs as part of the incorporation of the species into the cell for the production of biomolecules, dissimilatory reduction products are released into the extracellular environment or reduced externally without ever entering the cell.[2] Microorganisms that reduce extracellular metals such as Fe(III) and Mn(IV) oxides are referred to as dissimilatory metal-reducing bacteria (DMRB), although this group includes members of both the *Bacteria* and *Archaea*.[3] DMRB are found in a variety of anoxic environments, such as aquatic sediments and subsurface aquifers. Fe(III) and Mn(IV) are common in these environments, and the absence of oxygen necessitates other forms of microbial metabolism. Of particular interest are DMRB that can conserve energy from the

reduction of extracellular metals and can grow with an extracellular metal as the sole terminal electron acceptor for respiration. In 1988, Lovley and Phillips described the first DMRB that could completely reduce organic carbon to carbon dioxide while utilizing Fe(III) oxides as the sole electron acceptor.[4] This organization was subsequently classified as the first representative of the genus *Geobacter* and named *G. metallireducens* for its ability to conserve energy from the reduction of Fe(III), Mn(IV), and U(VI).[5,6]

DMRB are a phylogenetically diverse group, and it is believed that the ability to reduce Fe(III) and Mn(IV) evolved independently.[3] As might be expected, then, there is great variety in the metabolism of different DMRB. Most DMRB are able to utilize other organic or inorganic electron acceptors in addition to Fe(III) and Mn(IV), including other metals, oxygen, nitrate, elemental sulfur, sulfate, and humic substances. (Humic substances are a broad class of organic compounds of variable composition that generally contain redox-active quinone moieties; they are prevalent in many soils and sediments.[6]) Certain organic acids, like fumaric acid, can also serve as electron acceptors, although they are not believed to be significant as electron acceptors in the environment. There is less diversity in the electron donors utilized by DMRB. Although hydrogen, sugars and, in at least a few cases, amino acids can be completely oxidized to carbon dioxide by certain DMRB species, organic acids are likely the most environmentally relevant class of electron donors. Acetate, in particular, is an end product of fermentation in anoxic environments and a common electron donor for DMRB. Thus even if DMRB cannot outcompete fermentative microorganisms for sugars and other fermentable compounds in

the environment, they may be able to utilize the organic acids that other organisms produce.[3]

Iron exists in a variety of forms in the environment, but Fe(III) is only soluble under acidic conditions (pH < 3) or in the presence of certain chelators.[7] The utilization of an insoluble electron acceptor has two important implications for DMRB. First, Fe(III) reduction becomes less thermodynamically favorable when Fe(III) is in the form of iron oxides or hydroxides. The standard electrode potential E^0 for the Fe^{3+}/Fe^{2+} redox couple is + 0.77 V vs. the standard hydrogen electrode (SHE). The effective reduction potential is lower, however, when Fe(III) is in the form of insoluble oxide or hydroxides, according to the Nernst equation:

$$E = E^{\circ} - \frac{RT}{nF} \ln Q \qquad 3.1$$

where E is the electrode potential, R is the gas constant, T is the temperature, n is the number of moles of electrons transferred in the half-reaction, and F is the Faraday constant.[8] Q, the reaction quotient, is given by the ratio of the concentrations (or, technically, the activities) of the reduced and oxidized species. For the Fe^{3+}/Fe^{2+} couple, $Q = [Fe^{2+}]/[Fe^{3+}]$. A relatively insoluble Fe(III) species will have a small value of $[Fe^{3+}]$ and, as a result, a larger value of Q. From Equation 3.1, a larger Q corresponds to a lower effective reduction potential. Thus highly crystalline iron oxides have lower reduction potentials than poorly crystalline iron hydroxides. The reduction potential of ferrihydrite, a nanocrystalline oxyhydroxide, may range from − 0.1 to + 0.1 V vs. SHE under environmental conditions, while Fe_3O_4 has a potential of − 0.314 V vs. SHE. Likewise the potentials of solubilized Fe(III) chelated by nitrilotriacetic acid (NTA) or citrate are higher, at + 0.372 V and + 0.385 V vs. SHE, respectively. It should be noted

that these values are dependent on pH and concentration. The reduction potentials of organic acids, an important class of electron donors for DMRB, are near − 0.3 V vs. NHE. For example, E^0 of the CO_2/acetate redox couple is − 0.29 V vs. NHE.[7] These values indicate that the oxidation of organic acids may be thermodynamically unfavorable when coupled to the reduction of Fe(III) in crystalline oxides.

The second implication of the insolubility of Fe(III), and perhaps the more remarkable one, is DMRB must either transport electrons out of the cell or else solubilize Fe(III) in order to respire. In contrast, microbes that utilize soluble electron acceptors for respiration can rely on diffusion to transport the electron acceptor to the inner membrane where reduction typically occurs.[9] Considerable effort has been devoted to elucidating the electron transfer mechanisms in different DMRB species, particularly the model organisms *Shewanella oneidensis* and *Geobacter sulfurreducens*. Nonetheless, many questions remain. Electron transfer mechanisms can be broadly classified as direct, involving cell-electron acceptor contact, or indirect, where charge is transported by a soluble redox-active mediator (or electron shuttle).[3] Although *G. sulfurreducens* does not appear to secrete electron shuttles,[6] *S. oneidensis* has been shown to produce flavins that can reduce Fe(III) oxides.[10,11] Instead of or in addition to transporting electrons out of the cell, there are reports that some DMRB might use chelators to solubilize Fe(III),[6] but less is known about this mechanism.[7]

Despite the unresolved questions about electron transfer processes in DMRB, it is clear that *c*-type cytochromes play a key role. Cytochromes are heme-containing proteins that facilitate electron transport in biological systems. The genomes of certain DMRB contain dozens of genes predicted to encode multiheme *c*-type cytochromes; *G.*

sulfurreducens, for example, has 111 predicted *c*-type cytochromes, while *Escherichia coli* has only 7.[12] Unlike *c*-type cytochromes in bacteria like *E. coli*, which are primarily localized to the inner membrane, *c*-type cytochromes in DMRB are also found in the periplasm and associated with the outer membrane. These *c*-type cytochromes comprise an electron transport chain that links the cell interior, where electrons are generated during metabolism, to the outer membrane, where reduction of extracellular electron acceptors can occur. This electron transport chain is critical for the reduction of insoluble electron acceptors; many *c*-type cytochrome mutants of *G. sulfurreducens* and *S. oneidensis* are impaired at or essentially incapable of growth on metal oxides or electrodes.[13-16] There is also some evidence for the involvement of outer-membrane cytochromes in the reduction of soluble electron shuttles like humic substances.[17] The role of *c*-type cytochromes in metal reduction by *G. sulfurreducens* is discussed in more detail in Chapter 3.2, and the spectroscopy of cytochrome proteins is introduced in Chapter 3.3.

Like metal oxides, electrodes are insoluble and extracellular, and it has been found that some DMRB can transfer electrons to anodes in microbial fuel cells (MFCs).[18] In MFCs, a pure or mixed microbial culture extracts electrons from organic matter, either by fermentation or by oxidation, and transfers electrons to the anode. Electrons travel through a load in the external circuit to the cathode, where an abiotic reduction process, typically the reduction of oxygen, occurs to complete the electrochemical circuit. The anodic compartment is usually kept anoxic to prevent losses due to the diversion of electrons to oxygen. When MFCs are established in aquatic sediments or in other anoxic environments, complex microbial communities form on the anodes. Members of the

Geobacteraceae family are heavily represented in these communities. Further it has been shown that pure cultures of some DMRB lab strains, like *G. sulfurreducens*, can grow on MFC anodes, forming biofilms up to 50 μm in thickness.[19] The ability of organisms like *G. sulfurreducens* and *S. oneidensis* to produce current in MFCs is also dependent on *c*-type cytochromes.[16,20,21] In addition to the practical interest in developing MFCs for power generation in remote areas or for remediation of contaminated subsurface environments,[18] the growth of microbial biofilms on electrodes is proving to be a valuable platform for fundamental studies, allowing researchers to use electrochemical methods and theory to probe charge transfer processes in DMRB.

3.2 Electron Transport in *Geobacter sulfurreducens*

3.2.1 Introduction to Geobacter sulfurreducens

We use the model dissimilatory metal-reducing bacterium *Geobacter sulfurreducens* in our studies. *G. sulfurreducens* was isolated from a hydrocarbon-contaminated ditch and first described by Caccavo *et al.* in 1994.[22] Taxonomically, *G. sulfurreducens* is a member of the *Geobacteraceae* family, within the *δ-proteobacteria* class of Gram-negative bacteria. *G. sulfurreducens* cells are rod-shaped and approximately 0.5 μm in diameter by 2 – 3 μm in length. *G. sulfurreducens* was the first bacterium found to couple acetate and hydrogen oxidation to Fe(III) reduction, and the species was named for its ability to reduce elemental sulfur (S^0) to hydrogen sulfide. Unlike *G. metallireducens*, the first member of the genus *Geobacter* to be isolated, *G. sulfurreducens* can also couple oxidation of acetate to the reduction of fumarate,

facilitating its routine laboratory culture. *G. sulfurreducens* was found to produce on average 6.8 equivalents of Fe(II) per equivalent of acetate consumed. If no acetate is reserved for other biosynthetic processes, oxidation of acetate to bicarbonate should yield 8 equivalents of Fe(II):[22]

$$CH_3COO^- + 8Fe(III) + 4H_2O \rightarrow 2HCO_3^- + 8Fe(II) + 9H^+$$

When fumarate was used as an electron acceptor, *G. sulfurreducens* produced 3.8 equivalents of the reduction product succinate per equivalent of acetate consumed, close to the expected 4:1 stoichiometry:[23]

$$CH_3COOH + 4C_4H_4O_4 + 2H_2O \rightarrow 4C_4H_6O_4 + 2CO_2$$

G. sulfurreducens was initially reported to be a strict anaerobe, but more recent studies have found that it is tolerant of low levels of oxygen and can even utilize oxygen as the sole electron acceptor under certain conditions.[23] The *G. sulfurreducens* genome was sequenced in 2003; it was found to contain 3.8 million base pairs and 3,466 open reading frames that could encode proteins.[24] Proteomic studies have detected approximately 90% of these predicted proteins in total under different growth conditions.[25,26] A genetic system for *G. sulfurreducens* was developed in 2001.[27]

3.2.2 The Role of c-Type Cytochromes in G. sulfurreducens Electron Transport

As mentioned above, the genome of *G. sulfurreducens* encodes 111 predicted *c*-type cytochromes, many of which contain multiple heme prosthetic groups. These proteins are identified by the common heme binding motifs: CX_2CH, $CX_{3–4}CH$, CX_2CK, and A/FX_2CH, where X is variable. The hemes are covalently bound to the cysteine residues by thioester linkages.[12] Over the last decade researchers have begun to explore the role of some of these hemes in the *G. sulfurreducens* electron transport chain.

Several of the *c*-type cytochromes produced in large quantity by *G. sulfurreducens* or found to be important in the reduction of different electron acceptors are summarized in Table 3.1. In particular, the outer-membrane hexaheme cytochromes OmcS and OmcT are required for growth on insoluble Fe(III) and Mn(IV) oxides, but not for growth on fumarate, soluble Fe(III) citrate, or metal oxides in the presence of chelating agents or electron shuttles.[15] Current produced by a Δ*omcST* double knockout mutant in a MFC was under 40% of the wild type (WT) level.[20] OmcZ, an octaheme cytochrome found primarily in the extracellular matrix, was shown to be critical to MFC current production. It does not, however, appear to be necessary for reduction of Fe(III) oxides.[21] Determining the role of different cytochromes is complicated by the redundancy in the *G. sulfurreducens* electron transport chain. OmcE, a tetraheme cytochrome, is one of the most abundant outer-membrane cytochromes produced by *G. sulfurreducens* during growth on Fe(III) oxides, Fe(III) citrate, or fumarate. A deletion mutant of *omcE* was found to be initially impaired in the reduction of Fe(III) oxides, but after a long lag time it recovered some ability to grow on the insoluble metal.[15] The Δ*omcE* mutant likewise displayed a delay in MFC current production, but with eventual recovery to WT levels.[20] In addition to facilitating electron transport from the cytoplasm to extracellular electron acceptors, *c*-type cytochromes may act as capacitors, storing electrons when no other electron acceptor is available. Esteve-Núñez *et al.* estimated that *G. sulfurreducens* contains 10^7 hemes per cell, and speculated that this electron storage capacity might help *G. sulfurreducens* maintain critical cellular functions during periods of electron acceptor limitation.[28]

Protein	Gene	# of Hemes	Location	Deletion Mutant Phenotype
OmcB	GSU2737	12	Outer membrane	Severe impairment in Fe(III) oxide and citrate reduction[14]; no impairment in MFC[20]; slight impairment in reduction of AQDS and humic substances[17]
OmcE	GSU0618	4	Outer membrane	Long lag time and impairment in Fe(III) oxide reduction, but not Fe(III) citrate[15]; lag time but recovery to WT levels in MFC[20]; slight impairment in reduction of AQDS and humic substances[17]
OmcS	GSU2504	6	Outer membrane (also on pili[29])	Severe impairment in Fe(III) oxide reduction, but not Fe(III) citrate[15]; moderate impairment in MFC[20]; slight impairment in reduction of AQDS and humic substances[17]
OmcT	GSU2503	6	Outer membrane	Severe impairment in Fe(III) oxide reduction, but not Fe(III) citrate[15]; moderate impairment in MFC[20]
OmcZ	GSU2076	8	Outer membrane	Severe impairment in MFC[21]; no impairment in reduction of AQDS and humic substances[17]
PpcA	GSU0612	3	Periplasm	Moderate impairment in reduction of Fe(III) citrate and severe impairment in reduction of AQDS coupled to acetate oxidation, but not to hydrogen oxidation[13]

Table 3.1 Properties of several important *c*-type cytochromes produced by *G. sulfurreducens*. AQDS is 9,10-anthraquinone-2,6-disulfonic acid, a humic acid analog.

3.2.3 The Role of Type IV Pili in G. sulfurreducens Charge Transport

Although it is clear that *c*-type cytochromes are involved in charge transport to extracellular electron acceptors in *G. sulfurreducens*, there remains considerable controversy about the role of a different protein: PilA, a type IV pilin protein. Type IV pili are protein filaments produced by a wide range of bacteria, although they are frequently studied in the context of pathogenic Gram-negative bacteria.[30-33] Pili are 6 – 8

nm in width and several micrometers long and are typically composed of a single pilin monomer, although minor pilin proteins are sometimes present. Type IV pili are important in cell attachment to surfaces, cell aggregation, and, in the case of pathogenic bacteria, adhesion to and invasion of host cells. They can be actively extended and retracted by the cell, which allows bacteria to move on surfaces in a type of motion called twitching motility. Type IV pili are separated into two groups, type IVa and type IVb, on the basis of several conserved elements in the pilin protein. Pilin proteins have: i) a glycine-terminated hydrophilic leader sequence, which is cleaved by a dedicated peptidase after the prepilin is secreted to the periplasmic side of the inner membrane ii) an N-methylated amino acid at the N-terminus of the cleaved protein; iii) a hydrophobic and highly-conserved N-terminal domain approximately 25 residues long; and iv) a pair of conserved cysteine residues, which form a disulfide bond, at the C-terminus of the protein. Type IVa pili have shorter leader sequences—less than 10 amino acids, in comparison to 15 – 30 for type IVb—and are smaller after processing—on average 150 amino acids, in comparison to 190.[30]

Atomic-scale structures of several pilin monomers have been obtained from X-ray crystallography and NMR. Pilin proteins of both type IVa and IVb have the same structural organization, with an N-terminal α-helix extending from a globular head domain. The globular head domain is defined by a β-sheet that interacts with the α-helix in an αβ-roll; the topologies of type IVa and type IVb pilin proteins differ in this region. Two highly variable sections within the head domain are the αβ-loop, linking the C-terminal end of the α-helix to the start of the β-sheet, and the D-region, flanked by the two conserved cysteine residues. Structural information about the polymerized pilus has

been obtained from X-ray fiber diffraction and cryo-electron microscopy.[30] The filament is assembled from pilin monomers packed in a helical arrangement with their N-terminal α-helices buried in the center of the fiber. Non-covalent interactions between these hydrophobic tails help hold the pilus together. The globular head domains form the filament surface, with primarily the variable αβ-loop and D-region exposed. These regions of the protein are implicated in adhesion to host cells in pathogenic bacteria, and their variability helps in evasion of the host immune response. The N-terminal α-helices do not fill the pilus interior completely; instead, a 1 – 2 nm diameter central channel runs along the length of the filament.[30]

Pilus assembly occurs on the periplasmic side of the inner membrane and requires several accessory proteins.[33] An overview of the assembly mechanism is given by Craig *et al.*[32] After a pilin monomer is secreted across the inner membrane, the globular head domain folds and an oxidoreductase enzyme catalyzes disulfide bond formation. Then a peptidase (PilD, in the nomenclature used for the pili of two common *Neisseria* species) cleaves the hydrophilic leader sequence, leaving the hydrophobic N-terminal α-helix buried in the inner membrane. Pilin monomers are recruited to the base of the growing pilus at a molecular platform formed by a tetrameric inner-membrane protein (PilG). A hexameric assembly ATPase (PilB) hydrolyzes ATP and acts as a lever to push the pilus away from the inner membrane by approximately 1 nm, enough to create a space at the base of the pilus for the next pilin monomer. The growing filament is secreted through an outer-membrane dodecameric secretin protein (PilQ). Pilus retraction occurs by depolymerization of the filament, which requires a separate retraction ATPase (PilT).[32] Type IV pili are related to the bacterial type II secretion system, which excretes proteins

from the periplasm through the outer-membrane to the extracellular environment. Certain proteins in this system have some homology with type IV pilin proteins and are termed pseudopilins. It has been hypothesized that these pseudopilins may aggregate to form a pilus-like structure that acts as a piston to extrude proteins through the outer-membrane.[31]

In 2005, Reguera *et al.* observed that the genome of *G. sulfurreducens* contained a gene, which they designated *pilA*, encoding a protein with an N-terminal domain homologous to other type IV pilin proteins.[34] They further found that a Δ*pilA* mutant was unable to reduce Fe(III) oxides in the absence of added chelators or electron shuttles. Most remarkably, they reported that conducting probe atomic force microscopy (CP-AFM) measurements revealed that isolated pili on a graphite surface were conductive transverse to the filament, with a linear current-voltage dependence. They proposed that conductive *G. sulfurreducens* pili could function to transport electrons from periplasmic or outer-membrane cytochromes to electron acceptors at a distance from the cell.

Assessment of the intrinsic conductivity of *G. sulfurreducens* pili has been hampered by a lack of structural information. The structure of the PilA protein has not been determined, nor is there a fiber model of the assembled pilus. There is, however, some genetic and biochemical information available. The PilA protein in its unprocessed form is 90 amino acids long. From residue Phe30 to Phe53 it is homologous to the hydrophobic N-terminal domains in post-processed type IV pilins, corresponding to the first half of the N-terminal α-helix in those proteins.[31] This homology implies that the first 29 residues of the *G. sulfurreducens* PilA protein are an extended leader sequence that is cleaved at some point in the assembly process, and that the mature PilA protein is

only 61 residues long. Thus PilA is much smaller than other Type IV pilin proteins. It has recently been demonstrated that the *pilA* gene contains two functional translation start codons, and that two PilA preprotein isoforms are produced, a long isoform (the full 90 amino acid sequence) and a short isoform (the 71 amino acids starting from Met20).[35] Although the mature PilA protein appears to be the same for both isoforms, the two preproteins nonetheless were found to have distinct functions in the cell.

It was initially reported by Reguera *et al.* that the Δ*pilA* mutant of *G. sulfurreducens* did not produce any extracellular filaments, but a subsequent study has shown that it can still produce some pilus-like structures, albeit a smaller number.[36] A significant decrease in filament production was observed after several additional mutations were made in the Δ*pilA* background to remove other identified or hypothetical pseudopilin proteins. It should be noted that a hyper-filamented strain, *G. sulfurreducens* strain MA, was used in these studies. Highlighting the similarities between type IV pili and the type II secretion system, there is growing evidence that the deletion of *pilA* impairs the secretion of cytochrome proteins to the extracellular side of the outer membrane.[35] In addition to the role of PilA in cytochrome secretion, there is some evidence that cytochromes may bind to pili in the extracellular environment. Immunogold localization and transmission electronic microscopy (TEM) imaging indicated that OmcS proteins were associated with *G. sulfurreducens* pili, with an average cytochrome spacing of almost 28.6 nm.[29]

3.2.4 Previous Studies of G. sulfurreducens Electrical Transport and Electrochemistry

Since the initial report of conductive pili in 2005, the electrical characteristics of *G. sulfurreducens* pili and biofilms have been studied using several different

experimental approaches. Veazey *et al.* measured the conductivity of individual pili on highly oriented pyrolytic graphite (HOPG) by scanning tunneling microscopy (STM),[37] and Malvankar *et al.* measured the conductivity of a network of pili between gold electrodes.[38] Both groups concluded that the pili showed metallic-like conductivity, which they assigned to intrinsic conductivity of the pilin monomers and not to electron hopping between cytochromes. Other work has been done using methods adopted from electrochemistry to characterize *G. sulfurreducens* biofilms in MFCs. Richter *et al.* demonstrated that cyclic voltammetry (CV) of a biofilm-graphite anode could be modeled qualitatively as a network of electrode-bound redox enzymes; they attributed the charge transport through the biofilm to electron hopping through cytochrome proteins.[39] Liu *et al.* grew *G. sulfurreducens* biofilms on indium tin oxide (ITO) substrates for spectroelectrochemical analysis, allowing them to monitor the spectral signature of *c*-type cytochromes in the biofilm while applying a potential and measuring the electrochemical current through the cell.[40] They found that the cytochrome proteins in the biofilm could be oxidized or reduced by the application of a potential to the electrode. In a different approach, Malvankar *et al.* grew *G. sulfurreducens* biofilms on an anode composed of two gold electrodes, each connected to the cathode, separated by a non-conductive 50 μm gap; after some time, the biofilm bridged the gap between the two halves of the anode.[38] In this geometry, the electrical conductance of the biofilm could be measured between the two gold electrodes. They found that the electrical conductance of biofilms produced by different *G. sulfurreducens* strains increased with increasing PilA production. Further they reported that a quadruple cytochrome deletion mutant (Δ*omcBEST*) biofilm was more conductive than a WT biofilm despite the loss of four prevalent cytochrome

proteins. On the basis of these results, they argued that the mechanism of charge transport through *G. sulfurreducens* biofilms was metallic-like conductivity through pili rather than electron hopping through cytochromes. This debate over the intrinsic conductivity of *G. sulfurreducens* pili and the role of *c*-type cytochromes in electron transport has not been resolved.

3.3 Spectroscopy of *c*-Type Cytochrome Proteins

3.3.1 Introduction to Cytochrome Proteins

The optical spectra of cytochrome proteins are dominated by the properties of their associated hemes, which themselves are iron complexes of porphyrin macrocycles. Porphyrins are derived from the parent compound porphin by substitution of R groups for the pyrrolic hydrogen atoms (Figure 3.1a). Porphyrins are highly-conjugated aromatic systems with π electrons delocalized around the planar ring. Neglecting substituents, the ring is approximately 8.5 Å in diameter and 4.7 Å thick.[41] Metalloporphyrins are metal complexes of porphyrin in which two pyrrole nitrogens are deprotonated and the ring carries a net charge of negative two. The metal cation is chelated by all four pyrrole nitrogens, as shown in Figure 3.1b. The resulting complex is neutral in the case of divalent metal cations. When trivalent metal cations such as Fe(III) are coordinated the metalloporphyrin bears a net positive charge, which is balanced by a counterion. In metalloporphyrins of larger cations, the metal ion may sit slightly above the molecular plane; the iron atoms in Fe(II) and Fe(III) hemes, for example, are out of the plane by approximately 0.8 Å and 0.3 Å respectively. This structural change triggers doming and

ruffling distortion in the porphyrin ring itself.[42] One or two axial ligands may coordinate the metal ion in metalloporphyrins, resulting in a square pyramidal or octahedral geometry.[41]

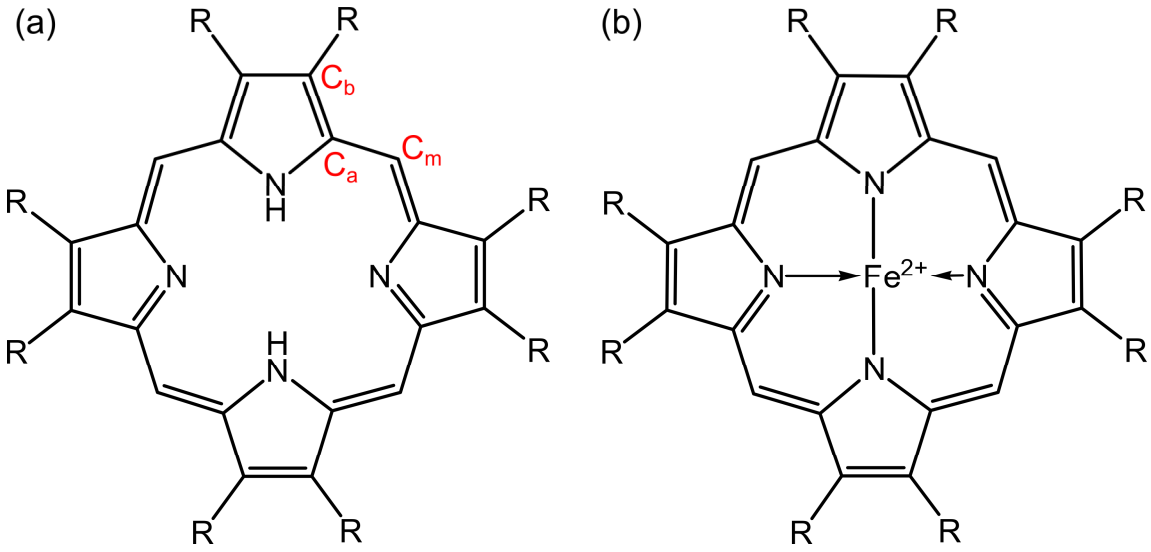

Figure 3.1 (a) General porphyrin structure with the *a*, *b*, and *m* carbons indicated. (b) General Fe(II) porphyrin structure.

Cytochrome proteins are hemeproteins, in which the metalloporphyrin chelate contains an iron atom in the Fe(II) or Fe(III) oxidation state.[41,43] They are classified as *a*-type, *b*-type, *c*-type, or *d*-type depending on the identity of the heme prosthetic group and the visible absorption spectrum. The iron atom is coordinated by cytoporphyrin IX in *a*-type cytochromes and by protoporphyrin IX in *b*-type cytochromes. In these two classes of cytochromes, the heme group is bound loosely to the protein through a coordinate bond with an amino acid side chain. The prosthetic group in *c*-type cytochromes is heme *c* (Figure 3.2), which is closely related to heme *b* but bound to the protein through two thioether bonds, although a few cytochromes have only one such bond. The heme may

be further coordinated to the protein in *c*-type cytochromes by amino acid side chains in one or both axial positions. The *d*-type cytochromes, in which the porphyrin macrocycle is partially hydrogenated to yield a hydroporphyrin, were initially considered a subclass of *a*-type cytochromes. These structural differences correspond to changes in UV-visible absorption spectra, and cytochromes are also classified on the basis of their α band absorption in the reduced state. (See Chapter 3.3.2 for a discussion of cytochrome UV-visible absorption spectroscopy). Cytochromes can be reversibly oxidized and reduced, a property that is integral to their role as electron transport proteins. The reduction potential of the Fe(II)/Fe(III) redox couple in heme is lower than for the uncoordinated cations, due to stabilization of Fe(III) by the negatively charged porphyrin macrocycle, and electron donating porphyrin side chains or axial ligands can further stabilize the oxidized form.[41] It follows that the reduction potentials of different *c*-cytochromes vary widely depending on the characteristics of the apoprotein.

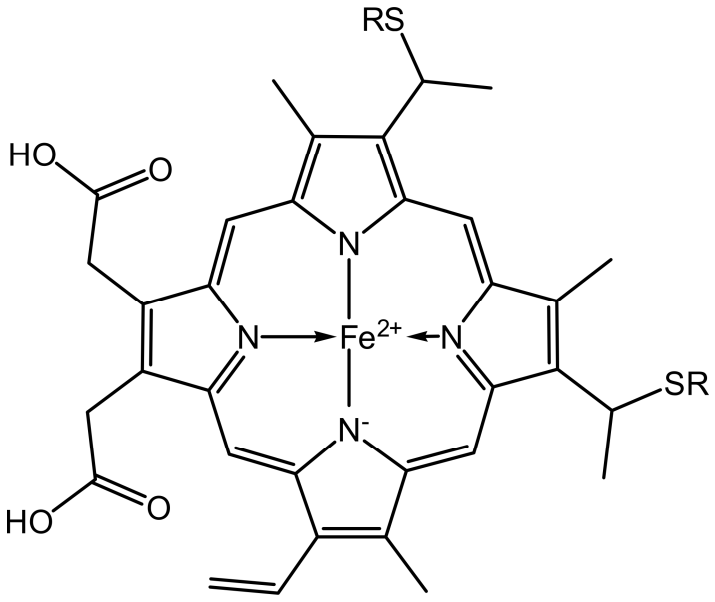

Figure 3.2 Heme *c* structure. The R groups in the thioether bonds represent the protein.

3.3.2 UV-Visible Absorption Spectroscopy of c-Type Cytochromes

The delocalized π-bonding network of porphyrins and metalloporphyrins gives rise to strong electronic transitions in the UV-visible spectral range; as a result, the molecules are strongly colored. In considering the symmetry of porphyrins and metalloporphyrins side groups can be neglected to first approximation, especially those groups with fully-saturated C-C bonds that are not part of the conjugated system. With this simplification, porphyrins and metalloporphyrins are members of the D_{2h} and D_{4h} point groups respectively.[42,44] This discussion will focus on the electronic spectra of metalloporphyrins, although porphyrin spectra are similar. The optical transitions of hemes in *c*-type cytochromes have a few dominant features. There is a strong peak at approximately 400 nm, with extinction coefficient ε on the order of 10^5 $M^{-1}\cdot cm^{-1}$, called the Soret or B band.[42] Weaker peaks at approximately 550 nm and 520 nm, with $\varepsilon \sim 10^4$ $M^{-1}\cdot cm^{-1}$, are the α and β bands, collectively labeled the Q bands. The Soret and α bands arise from π-to-π^* transitions between the two highest occupied molecular orbitals (HOMO) and the doubly-degenerate lowest unoccupied molecular orbitals (LUMO). The symmetries of the two HOMO states are A_{1u} and A_{2u} and the degenerate LUMO and LUMO+1 are E_g, resulting in two degenerate electronic transitions of E_u symmetry. These transitions are polarized in the plane of the porphyrin ring.[44] Configuration interaction mixes these transitions to give a higher-energy transition with a large oscillator strength, the Soret band, and a lower-energy transition with a small oscillator strength, the α band. The β band is a vibronic side band of the α transition, which gains appreciable intensity through vibronic borrowing from the strong Soret band transition.[42] The positions and intensities of the Soret and Q bands in metalloporphyrins are sensitive

to the electronegativity of the metal, with the transitions occurring at longer wavelength and with larger oscillator strength for lower oxidation states.[41] This behavior can be seen in *c*-type cytochromes upon reduction of Fe(III) to Fe(II).[40] The electronic spectra are also affected by spin state of the complexes; the transitions in high-spin octahedral Fe(II) complexes are at longer wavelength than are those in low-spin complexes.[41]

3.3.3 Raman Spectroscopy of c-Type Cytochromes

The presence of strong absorption bands in the visible spectrum of heme makes resonance Raman spectroscopy a powerful technique for the investigation of *c*-type cytochrome proteins. In resonance Raman spectroscopy, the frequency of the excitation light matches an electron transition of the molecule or material being studied.[45,46] Raman scattering cross-sections can be enhanced by a factor of 10^5 under resonant excitation.[47] Since the π-to-π^* electronic transitions in porphyrins arise from orbitals localized in the macrocycle and are polarized in the plane of the molecule, resonance Raman excitation of cytochromes primarily probes in-plane vibrational modes of the central chromophore and is less sensitive to non-conjugated side groups and the apoprotein itself.[48]

It has been shown that certain vibrational modes are most enhanced for Soret band excitation while others are prominent for Q band excitation.[42] Under Soret band excitation, totally symmetric vibrational modes (A_{1g} symmetry) are enhanced; these bands are polarized, with depolarization ratio $\rho < ¾$ as expected, where:

$$\rho = \frac{I_{\perp}}{I_{\parallel}} \qquad 3.2$$

In this expression, $I_{\perp}$ and $I_{\parallel}$ are the intensities of the Raman-scattered light polarized perpendicular and parallel to the excitation laser, respectively. Under Q band excitation,

however, vibrational modes of B_{1g}, B_{2g}, and A_{2g} symmetry are obtained. The B_{1g} and B_{2g} modes are depolarized ($\rho = ¾$) and the A_{2g} modes are inversely polarized ($\rho = \infty$). This behavior is explained by the vibronic theory of resonance Raman scattering. The enhancement of totally symmetric vibrational modes under Soret band excitation is due to A-term Raman scattering; these modes have favorable Franck-Condon overlap in the electronic transition. The enhancement of the Raman-active B_{1g} and B_{2g} modes and the normally Raman-inactive A_{2g} modes is a result of B-term activity; these are the modes that contribute to the vibronic mixing between the α and Soret band discussed above.

The resonance Raman spectra of hemeproteins are quite complicated, with many Raman-active vibrational modes. For example, 21 in-plane vibrational modes can be predicted by symmetry to appear in resonance Raman spectra of cytochrome *c* in the 1000 – 1650 cm^{-1} range,[42] and over 70 modes have been resolved and assigned from 100 – 1700 cm^{-1}.[49] In addition to the expected in-plane vibrations, deviations from planarity in the porphyrin macrocycle have been shown to activate out-of-plane vibrational modes as well as many IR-active modes of E_u symmetry, which are Raman-inactive under true D_{4h} symmetry.[49] Nonetheless, it is possible to determine the oxidation state and spin state of the heme moieties in *c*-type cytochrome proteins with good confidence by considering only one or a few Raman modes. In general, the position of porphyrin vibrational modes will be affected by both electronic and structural factors.[42] The totally symmetric pyrrole half-ring stretch at 1360 – 1375 cm^{-1} is considered the best marker band for heme oxidation state.[42,48,50] This band appears at the lower end of the frequency range for reduced heme and at the upper end for oxidized heme, and it is the strongest mode in the Raman spectrum for Soret band excitation. Consistent with the behavior of this marker

band, the porphyrin skeletal Raman modes are usually at lower frequencies when the central iron atom is in a reduced state. This behavior can be rationalized by considering the extent of back-bonding from the metal *d* orbitals to the porphyrin π^* orbitals; the more significant this back-bonding, the lower the effective porphyrin bond order and thus the lower the vibrational frequencies are expected to be. The *d* orbitals are more diffuse for Fe(II) than for Fe(III), so overlap with the porphyrin π^* orbitals will be greater for Fe(II).[42] The best marker band for iron spin state appears in the 1555 – 1585 cm^{-1} range and is resonant for Q band excitation. This mode appears at lower frequencies, and with lower intensity, for high-spin hemes than for low-spin hemes. The frequency shift in this mode can be understood in terms of structural changes in the porphyrin and the resulting effects on electronic coupling.[42]

3.3.4 Resonance Rayleigh Scattering of Porphyrin and Hemeproteins

As discussed in the previous section, the Raman scattering from *c*-type cytochromes provides a great deal of information about the oxidation state, spin state, and coordination of the heme moieties in the protein. Elastic Rayleigh scattering, although generally stronger than inelastic Raman scattering, is less informative. Nonetheless, because the Rayleigh scattering cross-section of a molecule is related to its polarizability, Rayleigh scattering is sensitive to molecular electronic properties.[51] Thus Rayleigh scattering, like Raman scattering, is enhanced when the incident light is resonant with a molecular electronic transition. Reinisch and colleagues measured quasielastic light scattering (QELS), corresponding to light within ± 5 cm^{-1} from the incident laser line, from cytochrome-*c* and another heme protein.[52,53] They found a resonance in the QELS cross-section when the incident light was resonant with the Soret band of the heme.

There were further able to distinguish the two contributions to QELS from cytochrome-*c*, the resonant scattering from the heme moiety and the non-resonant scattering from the globular protein, by the polarization characteristics of the scattered light. Rayleigh scattering from a hemeprotein like cytochrome-*c* is rather weak even at resonance, with cross-sections on the order of $10^{-21} – 10^{-23}$ $cm^2 \cdot sr^{-1} \cdot molecule^{-1}$.[53] For large aggregates of chromophores, however, the Rayleigh-scattered light can be quite strong.[51]

3.3.5 Previous Spectroscopic Studies of c-type Cytochromes in Geobacter spp.

The optical activity of *c*-type cytochromes and their prevalence in *G. sulfurreducens* and other *Geobacter* spp. has been exploited in several different types of spectroscopic studies. As discussed above, Liu *et al.* monitored the UV-visible absorption of *G. sulfurreducens* biofilms as a function of applied potential, showing from the spectra that the *c*-type cytochromes in the biofilm could be reversibly tuned between the oxidized and reduced states.[40] Although the strong fluorescence of porphyrin is normally quenched by coordination to iron in hemes,[41] Esteve-Núñez detected fluorescence from *c*-type cytochromes in *G. sulfurreducens* liquid culture and biofilms under UV excitation; they found only hemes in the reduced state displayed significant fluorescence intensity, with an excitation maximum at 350 nm and emission maxima at 402 nm and 437 nm.[28]

Other researchers have monitored the vibrational spectra of *G. sulfurreducens* and *Geobacter* spp. using several different techniques. Jarvis *et al.* demonstrated that *G. sulfurreducens* cells exposed to Ag(I) and Au(III) ions precipitated Ag nanoparticles outside of the cell and Au nanoparticles both inside and outside of the cell.[54] They obtained both unenhanced Raman spectra as well as surface-enhanced Raman spectra

(SERS) using the noble metal nanoparticles in a confocal micro-Raman configuration. (See Chapter 1.2 for a brief introduction to SERS.) In another confocal micro-Raman study, Millo *et al.* recorded surface-enhanced resonance Raman spectra (SERRS) of a mixed biofilm including *Geobacter* spp. on a silver electrode under potentiostatic control.[55] Virdis *et al.* performed a similar experiment but on a graphite electrode and thus without the SERS enhancement.[56] The IR spectra of *G. sulfurreducens* cells on a gold electrode under potential control was reported by Busalmen *et al.* using attenuated total reflection-surface enhanced infrared absorption spectroscopy (ATR-SEIRAS).[57] These last three studies found that the oxidation state of the *Geobacter c*-type cytochromes could be reversibly changed by sweeping the applied potential, in agreement with the work of Liu *et al.*[40]

3.4 Overview of Project Goals

The mechanism of electron transport in *G. sulfurreducens* and other DMRB is both of fundamental scientific interest and of great importance for applications like MFCs. There is an ongoing disagreement in the field about the intrinsic conductivity of *G. sulfurreducens* pili and the role of *c*-type cytochromes in electron transport. Spectroelectrochemical studies have clearly shown that *c*-type cytochromes in *G. sulfurreducens* are electrode-accessible, and some recent theoretical work has concluded that the electrical characteristics of DMRB pili can be explained by an electron hopping mechanism—meaning that band-like conduction through pili is not needed to account for the observed conductivity.[58-60] Questions still remain, however, and further research in this area is needed.

The goal of this project is to explore electron transport in *G. sulfurreducens* using optical and electrical methods developed to study nanomaterials. The strong UV-visible absorption and resonance Raman scattering of heme and the high concentration of *c*-type cytochromes in *G. sulfurreducens* means that we should be able to probe the redox state of cells and biofilms through optical measurements. The ability of *G. sulfurreducens* cells to transfer charge to an electrode should allow us to integrate optical measurements with electrical studies. If the observed conductivity of *G. sulfurreducens* pili results from electron hopping through pilus-associated *c*-type cytochromes, we can use our spectroscopic tools to look for the characteristic spectra of *c*-type cytochromes on the pili. If we do not detect such signals, we should be able to put an upper limit on the heme concentration associated with pili. Alternatively, if the conductivity of the pili arises from metallic band-like conduction, there should be a clear optical signature. We can look for evidence of this behavior using Raman spectroscopy and methods like micro-contrast spectroscopy and Rayleigh scattering spectroscopy, which are sensitive to electronic resonances.

3.5 Experimental Methods

3.5.1 Strain and Culture Conditions

Wild type *Geobacter sulfurreducens* strain PCA (ATCC 51573) was provided by Daniel Bond (University of Minnesota). In the standard growth medium, NBFA, acetate (20 mM) served as the electron donor and fumarate (40 mM) as the electron acceptor. A trace minerals mix, NB, was also used. The components of the NB minerals mix and the

NBFA medium are listed in Table 3.1 and Table 3.3. No vitamins, additional reducing agents (*e.g.*, cysteine hydrochloride), or redox indicators (*e.g.*, resazurin) were used. Cultures were grown in 25 mL anaerobic pressure tubes (Bellco Glass) sealed with butyl rubber stoppers and aluminum crimp seals, and 10 mL of media was added to each tube. To remove oxygen, tubes were sparged using a 20% CO_2:80% N_2 gas mix for 10 minutes before sealing and then for an additional 10 minutes after sealing.[61] To sterilize the growth media, tubes were then autoclaved for 30 minutes at 121 °C. Inoculations were performed in an anaerobic chamber (Coy Laboratory Products) from frozen stocks stored at − 80 °C. Cultures were grown primarily at 30 °C and 250 rpm in an incubator shaker, although growth was also observed at 25 °C and 37 °C.

Reagent	Molecular Mass (g/mol)	Mass per 1 L (g)	Concentration	
			Mix (mM)	Media (µM)
Nitrilotriacetic acid (only for NBFA)	191.14	1.5	7.85	78.5
$MnCl_2 \cdot 4H_2O$	197.91	0.1	0.51	5.1
$FeSO_4 \cdot 7H_2O$	278.01	0.5	1.80	18.0
$CoCl_2 \cdot 6H_2O$	237.93	0.17	0.71	7.1
$ZnCl_2$	136.3	0.1	0.73	7.3
$CuSO_4 \cdot 5H_2O$	249.69	0.03	0.12	1.2
$AlK(SO_4)_2 \cdot 12H_2O$	474.39	0.005	0.01	0.1
H_3BO_3	61.83	0.005	0.08	0.8
Na_2MoO_4	205.92	0.09	0.44	4.4
$NiCl_2$	129.6	0.05	0.39	3.9
$Na_2WO_4 \cdot 2H_2O$	329.85	0.02	0.06	0.6
Na_2SeO_4	188.94	0.1	0.53	5.3
Notes: Raise pH to 6.5 with NaOH after adding nitrilotriacetic acid (NTA). For NBFeA media, dissolve minerals in 100 mL of 0.5 M HCl instead of using NTA, then bring volume to 1 L.				

Table 3.2 NB minerals mix reagents and preparation notes.

Reagent	Molecular Mass (g/mol)	Mass per 1 L (g)	Concentration (mM)
Fumaric acid	116.07	4.64	40.0
KCl	74.55	0.38	5.1
NH_4Cl	53.49	0.2	3.7
$NaH_2PO_4 \cdot H_2O$	137.99	0.069	0.5
$CaCl_2 \cdot 2H_2O$	147.01	0.04	0.3
$MgSO_4 \cdot 7H_2O$	246.47	0.2	0.8
NB minerals mix (with NTA)	N/A	10 mL	N/A
Sodium acetate	82.03	1.66	20.2
$NaHCO_3$	84.01	2.0	23.8
Notes: Raise pH to 6 – 6.1 with NaOH after adding fumaric acid, then to 6.8 after all reagents are dissolved. Bring volume to 1 L, then add $NaHCO_3$.			

Table 3.3 NBFA medium reagents and preparation notes.

Cultures were also grown using 100 mM Fe(III) oxide as the electron acceptor in place of fumarate, in NBFeA medium. The components of NBFeA medium are listed in Table 3.4. Ferric iron was provided in the form of ferrihydrite, a nanocrystalline oxyhydroxide.[62] Ferrihydrite was synthesized by neutralization of $FeCl_3$, in an adaptation of literature procedures.[63,64] A 1 M stock of NaOH was slowly added to an aqueous 0.2 M solution of $FeCl_3$ while stirring. The initial $FeCl_3$ solution was orange and clear; upon

NaOH addition, the solution changed to reddish-brown and turbid. NaOH was added until the solution pH reached 7 – 8. The solution was then centrifuged at 2,500 × *g* for 10 minutes and resuspended in deionized (DI) water. This procedure was repeated five times to remove chloride. After the final centrifugation, the ferrihydrite solution was resuspended in a smaller volume of water to yield a final iron concentration of 100 mM and stored at 4 °C until use. For further analysis, a sample was lyophilized for 24 h and characterized by X-ray diffraction (XRD) in an Inel X-ray diffractometer.

Reagent	**Molecular Mass**	**Mass per 1 L (g)**	**Concentration (mM)**
KCl	74.55	0.38	5.1
NH_4Cl	53.49	0.2	3.7
$NaH_2PO_4 \cdot H_2O$	137.99	0.6	4.3
$CaCl_2 \cdot 2H_2O$	147.01	0.04	0.3
$MgSO_4 \cdot 7H_2O$	246.47	0.2	0.8
NB minerals mix	N/A	10 mL	N/A
Sodium acetate	82.03	1.66	20.2
$NaHCO_3$	84.01	2.0	23.8
Notes: Raise pH to 6.8 with NaOH after adding reagents, then to 6.8 after all reagents are dissolved. Bring volume to 900 mL, then add $NaHCO_3$. Add 1 mL of 100 mM ferrihydrite per 9 mL media.			

Table 3.4 NBFeA reagents and preparation notes.

NBFAYE solid medium was prepared for plating *G. sulfurreducens* cells following a modified procedure from Coppi *et al.*[27] NBFA medium was supplemented with 5 mM L-cysteine, 1.5% (w/v) agar, and 0.1% (w/v) yeast extract. The resulting NBFAYE medium was autoclaved for 30 min and then brought into the anaerobic chamber while still hot. Solutions were not sparged before autoclaving. Plates were poured inside the anaerobic chamber and stored there until use. Cells were plated and grown inside the anaerobic chamber. Micrographs of cultures were obtained using a Keyence VHX-1000 Digital Microscope.

3.5.2 Biochemical Characterization and Other Characterization Methods

Cell growth in NBFA medium was monitored by optical density at 600 nm (OD_{600nm}), measured with a Spectronic 20D+ spectrophotometer. The UV-visible extinction spectrum of *G. sulfurreducens* NBFA cultures was acquired using an Agilent 8453 Diode Array Spectrophotometer. Protein content of NBFA and NBFeA cultures was measured using the Bradford assay, where protein concentration is determined from a spectral shift in the absorption of Coomassie Brilliant Blue G-250 dye upon protein binding.[65] Bradford Reagent was obtained from Thermo Scientific, and bovine serum albumin (BSA) from New England Biolabs was used to prepare protein standards for calibration. Protein standards were prepared according to the Thermo Scientific instructions for either the standard assay (100 – 1,500 μg/mL) or the micro assay (1 – 25 μg/mL) depending on the expected protein concentration. Protein standards and samples were loaded into 96-well plates in triplicate and absorbance was measured at 595 nm and 465 nm using a plate reader (BioTek Synergy 4 Microplate Reader), after a 30 s shake and a 10 min incubation.

Before measurement of protein content for NBFeA cultures, iron oxide forms were dissolved following literature procedures.[66,67] A 650 μL aliquot of culture was pelleted by centrifugation at 3,200 × *g* for 15 min and resuspended in the same volume of phosphate buffered saline (PBS). (In some cases, the aliquot of culture was used directly without resuspension in buffer.) Then 520 μL of an oxalate solution (28 g/L ammonium oxalate monohydrate and 15 g/L oxalic acid) and 65 μL of 100 mM ferrous ethylenediammonium sulfate were added; the trace amount of Fe^{2+} assists in iron oxide dissolution. The solution was mixed by vortexing and incubated for 30 min at 37 °C, with additional vortexing once or twice during the incubation. To help precipitate protein, 110 μL of 6.1 M trichloroacetic acid (TCA) was added and the sample was incubated on ice for 30 min. The sample was centrifuged at 16,873 × *g* for 15 min and the supernatant was discarded. Finally the pellet was resuspended in 0.1 M NaOH and boiled for 5 min at 95 °C to lyse the cells. The sample was allowed to cool to room temperature before protein measurements were made. A small amount of iron oxide sometimes precipitated from solution upon addition of 0.1 M NaOH, but it was allowed to settle to the bottom of the tube and aliquots for the protein assay were removed from the top. In these measurements, BSA standards for the Bradford assay were prepared using 0.1 M NaOH instead of water because the addition of base was found to have a small but non-negligible effect on the absorption of the dye.

The identity of *G. sulfurreducens* cells was confirmed by 16S ribosomal RNA (rRNA) sequencing. The polymerase chain reaction (PCR) technique was used to amplify 16S rRNA using primers 27F and 1492R (see Table 3.5) with Phusion polymerase (New England Biolabs) and a Techne TC-3000G Thermal Cycler. An

aliquot of culture in NBFA medium was used as the template for PCR. Cells were lysed by a longer initial denaturation step, 5 minutes at 98 °C, before the first PCR cycle. PCR products were separated by gel electrophoresis on an 0.8% agarose gel in Tris-acetate-EDTA (TAE) buffer. DNA was stained with bromophenol blue and visualized using a MinBIS Pro gel imaging system (DNR Bio-Imaging Systems Ltd.). Bands were cut from the gel and separated with an E.Z.N.A. Ultra-Sep Gel Extraction Kit (Omega Bio-Tek), then DNA concentrations were measured (BioTek plate reader with Take3 Micro-Volume Plate). DNA sequencing was performed by GENEWIZ, Inc.

Primer	**Sequence**
27F (LD351)	AGA GTT TGA TCC TGG CTC AG
1492R (LD352)	GGT TAC CTT GTT ACG ACT T

Table 3.5 Primers used for PCR amplification of *G. sulfurreducens* 16S rRNA gene.

Pili and other loosely-bound extracellular proteins were isolated from *G. sulfurreducens* cells following a procedure published by Rollefson *et al.*[68] NBFA cultures were pelleted by centrifugation at 3,220 × *g* for 15 min (Eppendorf 5810R Centrifuge) and resuspended in 1/100th the volume of PBS. Pili and other proteins were sheared by vortexing the resuspended cells for 2 minutes (Disruptor Genie). The solutions were centrifuged at 16,000 × *g* for 5 min (Sorvall Biofuge Fresco) to pellet cells. The supernatant was removed and centrifuged again at 16,000 × *g* for 25 min at 4 °C. Following this second centrifugation step, the supernatant was collected and $MgCl_2$

was added from a 1 M stock to give a final concentration of 0.1 M. The Mg^{2+} ions help precipitate the proteins in the supernatant. The solution was incubated overnight at 4 °C and then centrifuged at 30,000 × *g* for 1 h at 4 °C (Beckman Coulter Optima MAX-E Ultracentrifuge with TLA 120.2 rotor). After centrifugation, the supernatant was carefully removed with a micropipette to prevent the small, loose pink pellet from being disturbed. The pellets were resuspended in 50 µL Tris-HCl buffer (pH 8) with or without 8 M urea. According to Rollefson *et al.*, urea helps depolymerize pili so that pilin monomers can be obtained. The resuspended proteins were separated by sodium dodecyl sulfate polyacrylamide gel electrophoresis (SDS-PAGE). Samples were boiled in sample buffer (Invitrogen) at 95 °C for 15 min and then separated on a NuPAGE 4-12% Bis-Tris gel (Invitrogen) with 2-(N-morpholino)ethanesulfonic acid (MES) running buffer (Invitrogen). Proteins were stained using a Pierce Silver Stain Kit (Thermo Scientific) and visualized using a flatbed scanner.

A similar procedure was followed to shear pili from cells for transmission electron microscopy (TEM), but the pellet from ultracentrifugation was resuspended in 50 mM N-cyclohexyl-2-aminoethanesulfonic acid (CHES) buffer (pH 9.5) to minimize bundling of pili. Samples of resuspended pili and NBFA cultures were deposited on Formvar/carbon film TEM grids (Electron Microscopy Sciences) for 5 min. Excess liquid was wicked away and then the grids were fixed for 5 min with 2% glutaraldehyde in PBS. The grids were placed on a 10 µL droplet of deionized (DI) water for 30 s to rinse off excess glutaraldehyde and then stained for 5 min with a 2% aqueous solution of uranyl acetate. Excess uranyl acetate was removed by wicking with a Kimwipe.

Micrographs were acquired in a JEOL JEM-100CX TEM with 100 kV accelerating voltage.

3.5.3 Optical Spectroscopy

For optical studies, cells were pelleted by centrifugation at 3,200 × *g* for 15 min and resuspended in 1/10th the volume of PBS. Cells were dropcast on quartz slides (SPI Supplies, 1 mm thick) or glass coverslides (VWR, 0.13 – 0.16 mm thick) for 15 min, then rinsed gently with DI water and dried with N_2 gas. Substrates were cleaned by sonication in methanol or ethanol before use.

Micro-Raman and micro-contrast spectroscopy were performed in the system described in Chapter 2.4. Dark field scattering spectroscopy was implemented in an inverted microscope (Nikon TE300) with a 100 W halogen lamp (Nikon) and a 0.95 – 0.80 NA dark field condenser (Nikon). A 100× (0.5 – 1.3 adjustable NA) oil immersion objective (Nikon) was used with Nikon Type A (n = 1.515) immersion oil. Light exiting the microscope was dispersed by a 0.3 m monochromator (Acton Spectra-Pro 300i) with a reflective ruled grating (150 grooves/mm) and imaged on a 512 × 512 pixel thermoelectrically cooled EMCCD detector (Princeton Instruments PhotonMAX 512B). A sandwich geometry was used for some measurements, in which an index matching fluid (Cargille Certified Refractive Index Liquid AAA Series, n = 1.380) was placed on the sample and topped with another glass coverslip. A 1.43 – 1.20 NA oil immersion dark field condenser (Nikon) was used in this geometry. Dark field scattering spectra of *G. sulfurreducens* cells were obtained by narrowing the spectrometer entrance slit to the width of a single cell. Spectra from multiple spatially separated cells could be acquired simultaneously by lining up the cells along the vertical length of the slit. Light scattered

by cells and the substrate was collected by reducing the objective NA to exclude directly transmitted light. The scattering intensity from a single cell was obtained by binning all the vertical pixels containing scattered light, and the corresponding background intensity was obtained by binning an equally-sized vertical region of the nearby substrate. The objective NA was increased to its maximum value to collect light from the lamp for normalization of scattering spectra. Several overlapping grating positions were needed to cover the full wavelength range of the halogen lamp. A holmium perchlorate solution was used for wavelength calibration, following the same approach as in the micro-contrast measurements. Images of cells could be recorded on the EMCCD detector by collecting the zero-order diffraction mode from the same grating. Images of cells were also recorded using a SPOT Idea 3.1 megapixel (MP) camera mounted on the trinocular tube of the microscope eyepiece.

3.6 Results and Discussion

3.6.1 Growth of G. sulfurreducens on Liquid and Solid Media

Figure 3.3a shows growth curves for two *G. sulfurreducens* NBFA cultures at 25 °C. Growth commenced after a lag time of approximately 24 h and the culture reached stationary phase at 120 h. The natural logarithm of the optical density at 600 nm is plotted for the same curves in Figure 3.3b along with linear fits to the exponential growth region. The linear fits correspond to a doubling time of approximately 11.5 – 12 h during exponential growth. *G. sulfurreducens* cultures grew faster at higher temperatures, with doubling times of 6 – 7 h at 30 °C and 5 h at 37 °C, and with somewhat shorter lag times.

NBFA medium is colorless but *G. sulfurreducens* cultures are bright pink after several days of growth (Figure 3.4a) due to the high concentration of *c*-type cytochromes. The UV-visible extinction spectrum of an air-oxidized NBFA culture is shown in Figure 3.5. The Soret band is superimposed on the broad scattering background from the cells. Although the α and β bands are not as strong, weak features in the appropriate spectral region are visible. *G. sulfurreducens* cultures grown on solid NBFAYE plates are also bright pink, with some variation in colony size (Figure 3.4b).

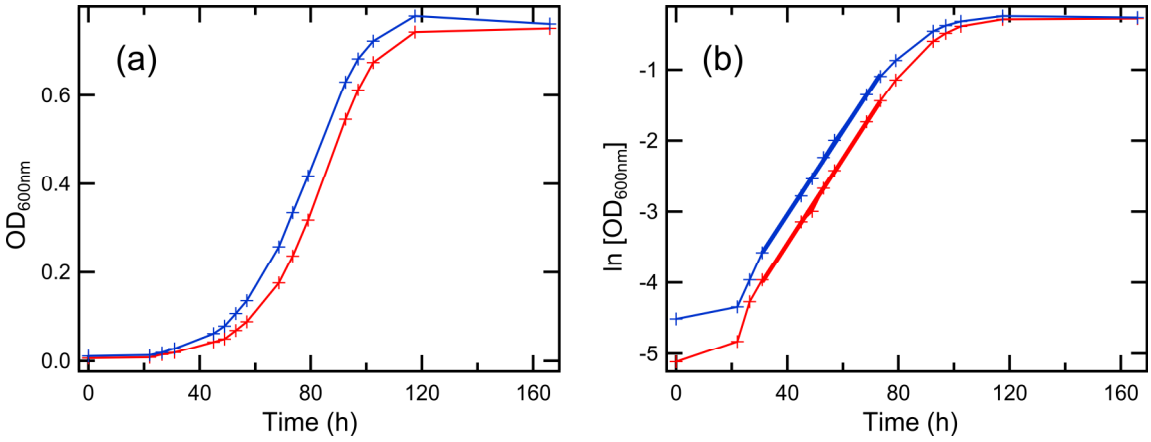

Figure 3.3 Growth curves for NBFA *G. sulfurreducens* cultures at 25 °C with (a) OD_{600nm} and (b) ln [OD_{600nm}] plotted against time. Linear fits to the exponential growth region are shown in (b).

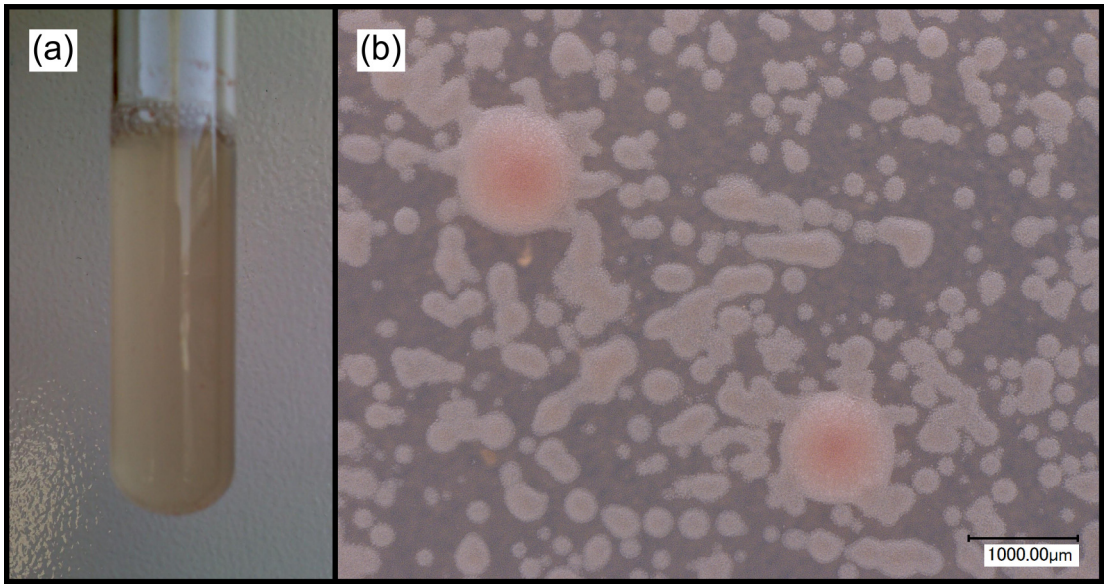

Figure 3.4 (a) Photo of *G. sulfurreducens* NBFA culture. (b) Photo of *G. sulfurreducens* colonies on an NBFAYE plate.

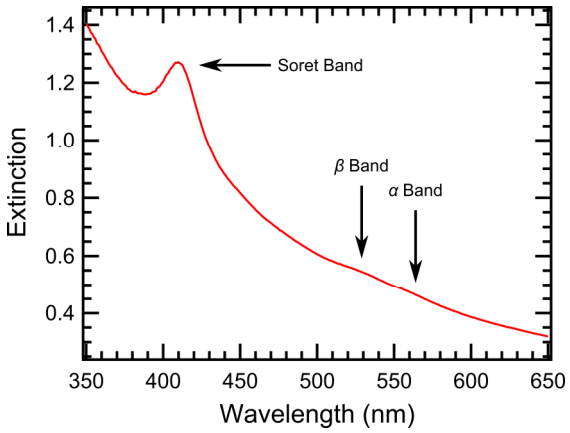

Figure 3.5 UV-visible extinction spectrum of an air-oxidized *G. sulfurreducens* culture in NBFA medium.

Fumarate serves as the sole electron acceptor in NBFA medium, but *G. sulfurreducens* can also be grown using ferrihydrite as the terminal electron acceptor. Figure 3.6 shows an XRD pattern obtained from lyophilized ferrihydrite powder. The

broad background for diffraction angles $2\theta > 10°$ is indicative of an amorphous or nanocrystalline material and typical of ferrihydrite.[62] NBFeA medium prepared with 100 mM ferrihydrite is reddish-brown (Figure 3.7). After inoculation with *G. sulfurreducens* cells and incubation for several weeks, the NBFeA medium gradually turns black. No color change is observed over the same time period for NBFeA medium incubated under the same conditions. Strong scattering from the ferrihydrite particles in NBFeA medium precludes the use of OD_{600nm} measurements to monitor cell growth. Instead, cell growth can be confirmed by dissolving the iron oxide particles and assaying for protein using the Bradford method. Preliminary experiments have confirmed that the protein content determined by the Bradford assay for *G. sulfurreducens* NBFA cultures tracks the growth curves obtained from OD_{600nm} measurements. The protein content for a *G. sulfurreducens* NBFeA culture late in stationary phase was found to be approximately 3 μg protein/mL. Taking the average protein content per bacterial cell to be on the order of 100 fg,[1] we can calculate a cell density of approximately 10^7 cells/mL. This value is in reasonable agreement with previous reports of cell density for *G. sulfurreducens* grown on iron oxides,[22] albeit somewhat lower, possibly because our culture was in late stationary phase. It should be emphasized that the Bradford assay provides only an approximate measure of protein content, and these results should be validated further.

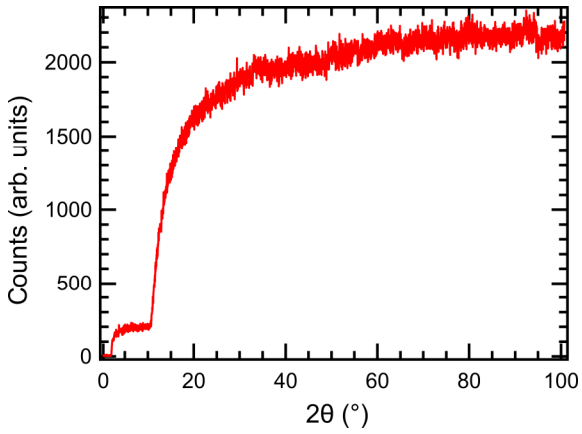

Figure 3.6 XRD spectrum of lyophilized ferrihydrite powder.

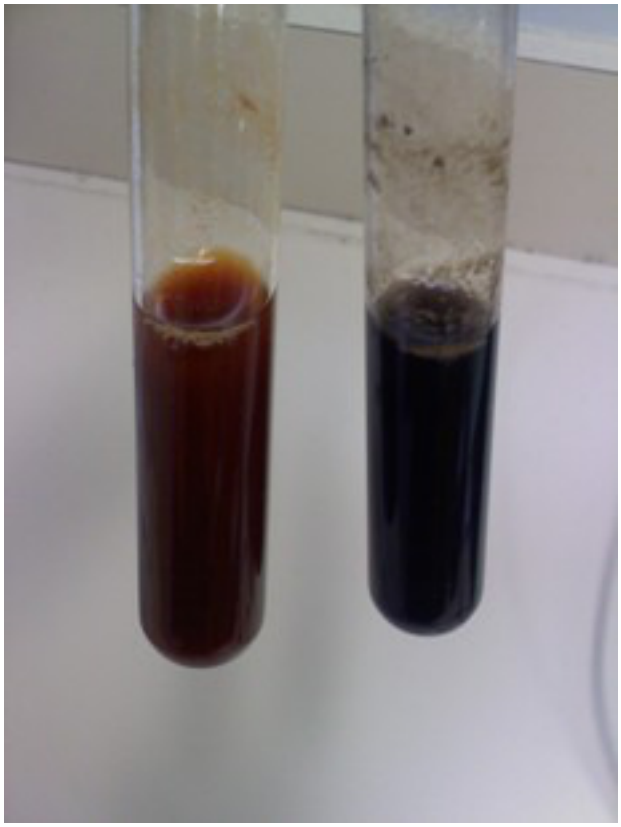

Figure 3.7 Photo of NBFeA medium after inoculation with *G. sulfurreducens* and incubation for several weeks (right tube) or after incubation alone (left tube).

Successful growth of *G. sulfurreducens* was verified by 16S rRNA sequencing. PCR was used to amplify the *G. sulfurreducens* 16S rRNA gene. Figure 3.8 shows the PCR products separated on an agarose gel. A band is seen at 1.5 kilobase pairs, the expected 16S rRNA fragment size. DNA sequencing confirmed that the amplified 16S rRNA sequence matched that of *G. sulfurreducens*.

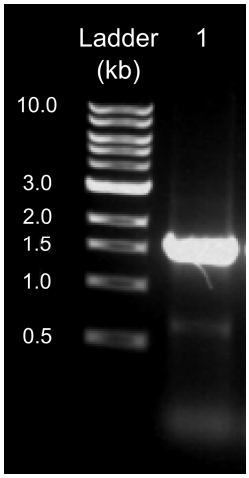

Figure 3.8 Agarose gel showing PCR amplification of *G. sulfurreducens* 16S rRNA gene.

3.6.2 Characterization of G. sulfurreducens Pili and Extracellular Proteins

The expression of type IV pili and other extracellular proteins was confirmed by SDS-PAGE of material sheared from the outside of *G. sulfurreducens* cells as described in Chapter 3.5.2. Bands appear in the protein gel (Figure 3.9) at approximately 6, 8, 12, 25, 30, 40, 50, 70, and 110 kDa. Several of these bands have been identified previously. The expected mass of PilA is approximately 6 kDa, and Rollefson *et al.* used mass spectrometry to confirm the identity of that band in their protein gel.[68] Other prominent

bands likely correspond to outer-membrane cytochromes OmcE, OmcS, and OmcZ. Lanes 1 and 2 in the protein gel correspond to extracellular material resuspended with and without urea, as described in Chapter 3.5.2. Although the PilA band appears in both lanes, additional bands are present in the sample that was not treated with urea. Lane 3 is the supernatant from the final ultracentrifugation step and lane 4 is an aliquot of the sample before incubation with $MgCl_2$.

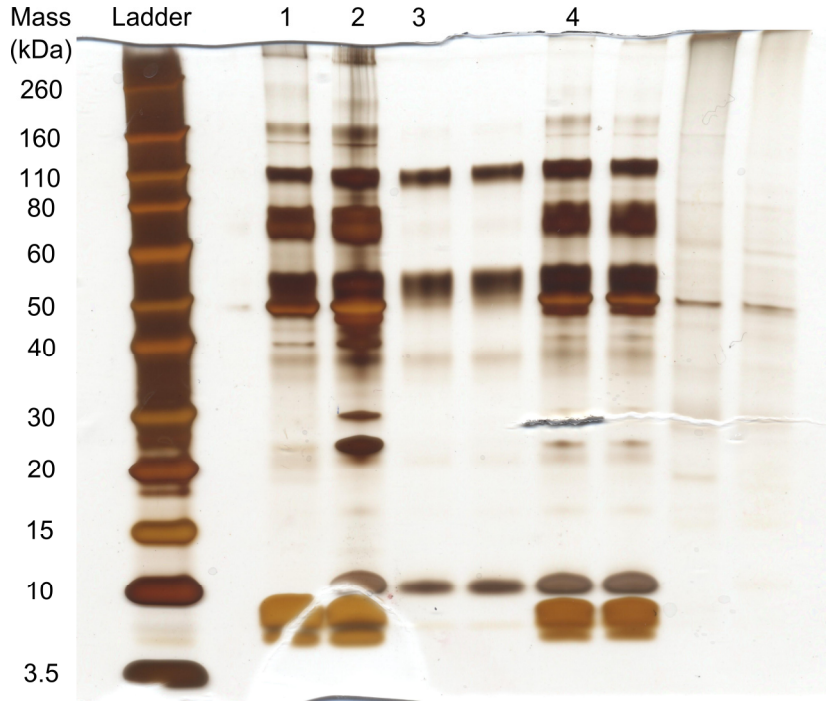

Figure 3.9 SDS-PAGE of pili and extracellular proteins. Lanes 1 and 2 are extracellular material resuspended with and without urea, respectively. Lane 3 is the supernatant from the final ultracentrifugation step and lane 4 is an aliquot of the sample before incubation with $MgCl_2$.

TEM was used to image *G. sulfurreducens* cells as well as sheared pili fractions. Figure 3.10a shows a *G. sulfurreducens* cell with filaments extending 100s of nm or more

from the cell surface. Based on the identification of a protein with the same molecular weight as PilA by SDS-PAGE, these filaments are likely to be type IV pili. We observed both isolated and bundled pili in sheared extracellular fractions (Figure 3.10b). In some cases dark globular structures are observed near or associated with pili. We are unsure what these features are, but we note that Reguera *et al.* observed similar features, which they found to be nonconductive, in their CP-AFM studies.[34] Reguera *et al.* also reported that pili expression during growth on soluble electron acceptors could be induced at 25 °C, lower than the optimal growth temperature for *G. sulfurreducens*. We observed pili in TEM micrographs of cultures grown at 25, 30, and 37 °C, although we cannot quantify the relative expression levels.

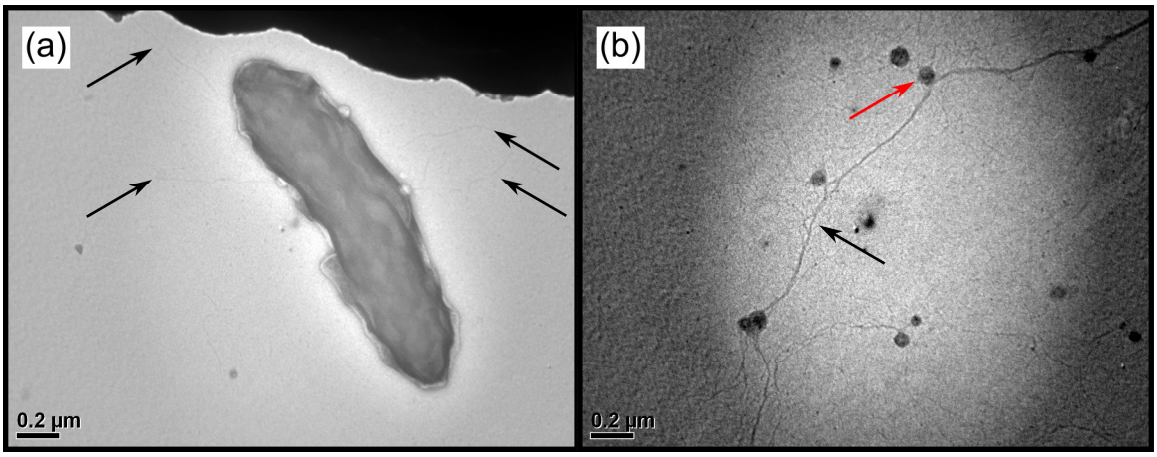

Figure 3.10 TEM micrographs of (a) *G. sulfurreducens* cell and (b) sheared pili. Black arrows indicate pili and the red arrow in (b) points to a globular pilus-associated feature.

3.6.3 Dark field Scattering Spectroscopy of G. sulfurreducens Cells

Dark field Rayleigh scattering spectroscopy is a powerful technique for the characterization of nanomaterials that inteact strongly with light. It has been used to probe the electronic transitions of carbon nanotubes[69-71] and the localized surface plasmon resonance of noble metal nanoparticles.[72] (See Chapter 1.1.2 for an introduction to localized surface plasmon resonances.) As discussed in Chapter 3.3.4, resonance Rayleigh scattering has been observed from purified hemeproteins.[52,53] Alignment or aggregation of the heme groups should increase the scattering intensity.[51] Further, dark field microscopy is a proven method for imaging unstained bacterial flagella,[73] which have diameters of approximately 15 nm, although we are not aware of any successful detection of unstained type IV pili. Here we describe initial attempts to use dark field scattering microscopy and spectroscopy to characterize *G. sulfurreducens* cells.

G. sulfurreducens cells were dropcast on glass coverslips for dark field scattering studies. An image of cells acquired using dark field illumination and a 3.1 MP CCD camera is shown in Figure 3.11a. The cell membrane scatters light strongly, giving the cells a hollow appearance. No pili or other extracellular appendages can be resolved. An image of the same region acquired with the 512 × 512 EMCCD detector is shown for comparison in Figure 3.11b. Here the light is passed through a spectrometer and reflected by a 150 grooves/mm grating before imaging, but the zero-order diffraction mode of the grating is used. Dark field scattering spectra of single cells are obtained by closing the slit and collecting the spectrally dispersed light. The Rayleigh scattering intensity, I, is calculated as:

$$I = \frac{I_{sample} - I_{background}}{I_{lamp} - I_{background}} \qquad 3.3$$

where I_{sample} is light scattered from the cell, $I_{background}$ is light scattered from the substrate, and I_{lamp} is the lamp light collected in transmission. Division by the lamp spectrum is necessary to normalize the scattering intensity. Rayleigh scattering spectra of the cells in Figure 3.11 are plotted in Figure 3.12. Although there is some variation in the scattering intensity for different cells, the general behavior is the same. The scattering intensity increases with decreasing wavelength, consistent with the frequency dependence of Rayleigh scattering, $I \sim \nu^{4.74}$ Below 425 or 450 nm the scattering intensity starts to decrease. There are no obvious features in the Soret or Q band regions.

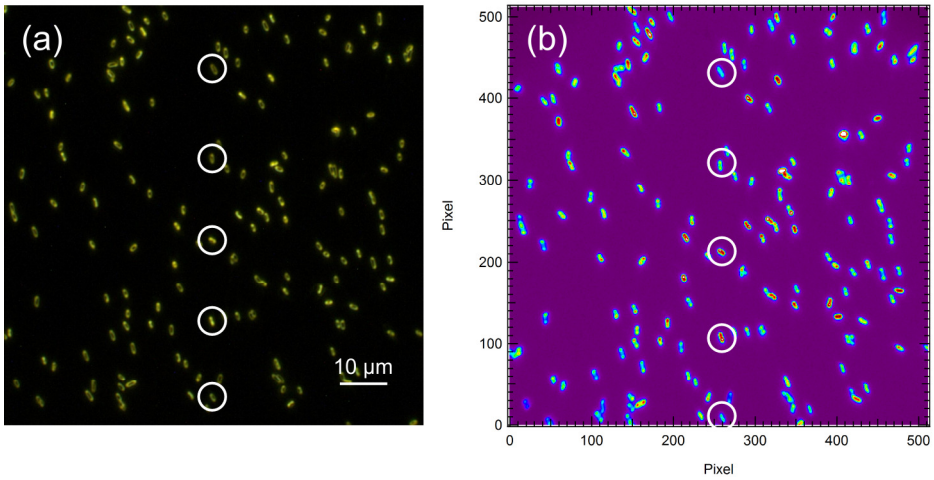

Figure 3.11 Dark field scattering micrographs of *G. sulfurreducens* cells on a glass coverslip recorded with (a) a 3.1 MP CCD camera and (b) a 512 × 512 pixel EMCCD detector. Spectra were acquired from the circled cells.

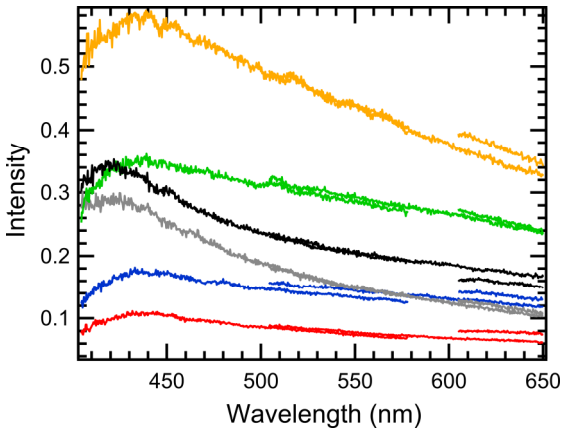

Figure 3.12 Dark field Rayleigh scattering spectra of single *G. sulfurreducens* cells on a glass coverslip in air.

The strong and spectrally broad scattering from *G. sulfurreducens* cells will obscure the narrower scattering peaks that should arise from cytochrome electronic transitions. Scattering from the cells can be reduced using an index-matching fluid and an oil immersion dark field condenser. Figure 3.13 compares dark field scattering images obtained under three different conditions. In Figure 3.13a, as in Figure 3.11b, the cells are on a glass coverslip and the dark field condenser is used with air as the imaging medium. In Figure 3.13b, the cells have been sandwiched between two glass coverslips with an index-matching fluid filling the space between the coverslips. A refractive index $n = 1.380$ was used in this measurement. This value was chosen to approximate an average cellular index of refraction, which should be somewhat larger than that of water ($n = 1.33$). It does not perfectly match the refractive index of the glass coverslips, and the introduction of an extra interface leads to an increase in the background scattering. The Figure 3.13c image was acquired with the same sandwich geometry but with an oil immersion dark field condenser. In this configuration the background scattering is

reduced. Although scattering from the cells in Figure 3.13b and Figure 3.13c is suppressed, we are still unable to resolve pili or other extracellular filaments. Rayleigh scattering spectra obtained in those configurations are shown in Figure 3.14. There are no clear cytochrome resonances in the Figure 3.14 spectra. There does appear to be some structure in the 400 – 450 nm region, but we have observed similar features in spectra of surface scratches or particles and in spectra of *E. coli* cells, which should have a much smaller concentration of heme.

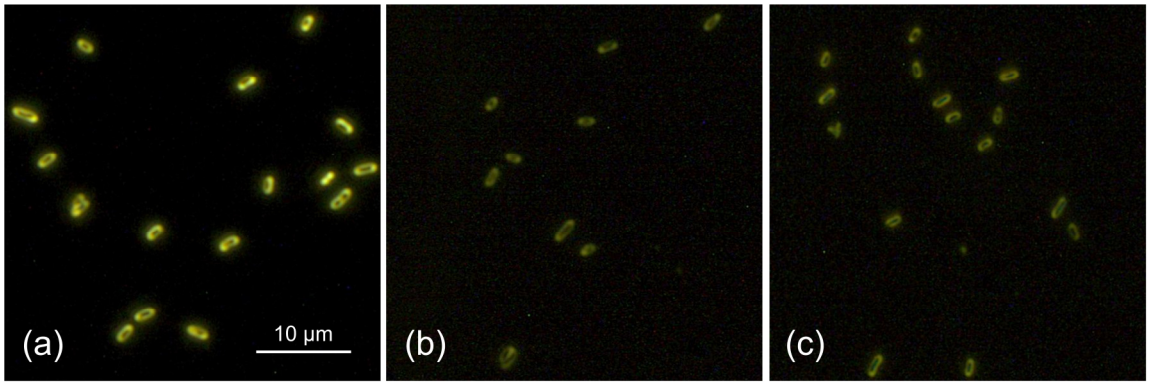

Figure 3.13 Dark field scattering micrographs of *G. sulfurreducens* cells taken in three configurations. (a) Cells on a glass coverslip with air dark field condenser. (b) Cells sandwiched between two glass coverslips with $n = 1.380$ refractive index fluid and air dark field condenser. (c) Same as (b) but with oil immersion dark field condenser.

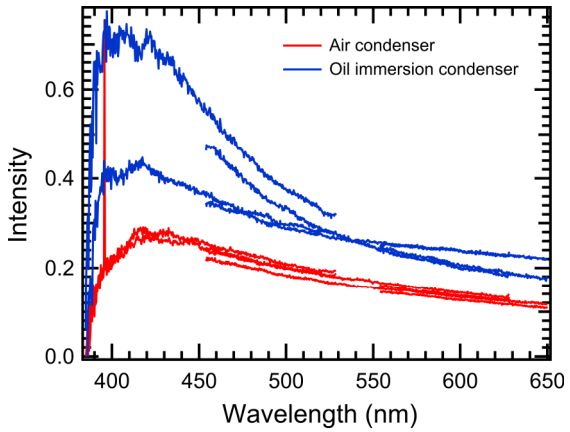

Figure 3.14 Dark field Rayleigh scattering spectra of *G. sulfurreducens* cells acquired using index-matching fluid and an air dark field condenser (red) or an oil immersion dark field condenser (blue).

3.6.4 Contrast Spectroscopy of G. sulfurreducens Cells

Reflective contrast spectroscopy is another probe of the optical properties of a material. As demonstrated in Chapter 2, this technique can be used to obtain electronic spectra of thin films of dye molecules and graphene. We have made preliminary attempts to measure reflective contrast spectra from *G. sulfurreducens* cells deposited on quartz slides. Figure 3.15 shows a micrograph of a typical sample recorded in a backscattering bright field geometry. A single cell, a small cell aggregate, and a region covered by a thick film of cells are indicated. Contrast spectra of single cells and small aggregates are plotted in Figure 3.16a. The contrast spectra are broad and featureless over the approximately 400 – 800 nm spectral range. The contrast increases going toward shorter wavelength until 450 – 500 nm, at which point it starts to drop. The contrast is generally positive, meaning that the cells reflect light more strongly than the quartz substrate, but the contrast magnitude varies for different cells. The contrast of the small cell aggregates

is larger than that of single cells. Contrast spectra for two thick films of *G. sulfurreducens* cells are shown in Figure 3.16b. Although the contrast of one spectrum (red) is positive and several times larger than the single cell and small aggregate contrast, the contrast of the other spectrum (blue) is negative and the magnitude of the contrast is somewhat smaller. Both traces have similar profiles to the spectra in Figure 3.16a but with a periodic series of peaks and troughs superimposed. The peak-to-peak spacing is approximately 50 nm at the short wavelength end of the spectrum and somewhat larger at the long wavelength end. We attribute these features to interference caused by multiple reflections of the light at the film-air and film-quartz interfaces.

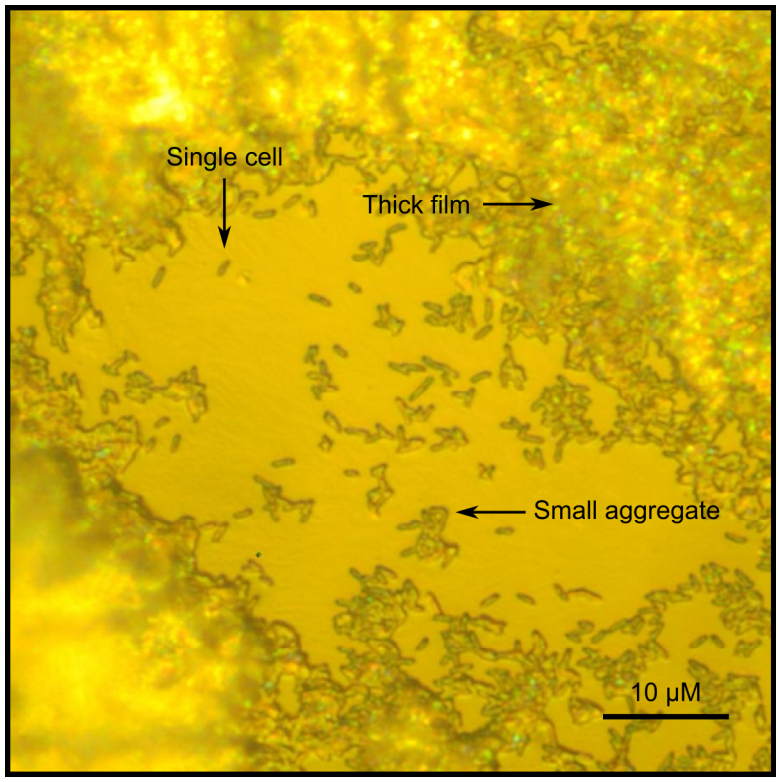

Figure 3.15 Bright field backscattering micrograph of *G. sulfurreducens* cells on a quartz slide. Arrows indicate a single cell, a small aggregate, and a thick film of cells.

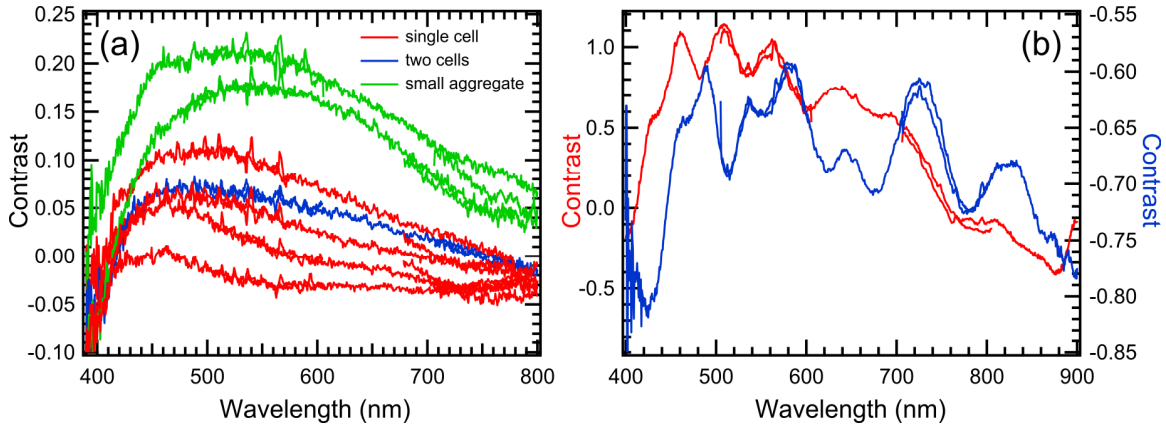

Figure 3.16 Reflective contrast spectra of *G. sulfurreducens* cells on a quartz substrate. (a) Contrast of single cells and small aggregates. (b) Contrast of thick films of cells.

There are no obvious signatures of *c*-type cytochromes in the Soret or Q band regions of the Figure 3.16 spectra, and interpretation of the data is complicated by several factors. First, the focused white light spot is approximately 2 μm in diameter at the sample, about four times larger than the typical *G. sulfurreducens* cell diameter and comparable to the cell length. A single cell or even two cells do not completely fill the light spot, and thus some light will be reflected from the substrate. The reflective contrast of a thin film is calculated as:

$$\delta_R = \frac{R_f - R_s}{R_s} \qquad 3.4$$

where R_f and R_s are the background-subtracted film and substrate reflectance, respectively. From Equation 3.4, it is clear that the measured contrast will be lower if R_f includes light reflected by the substrate. Small differences in cell size or in the position and focus of the light spot will introduce variation in the contrast measured for different cells. A related issue involves chromatic aberrations in our system. Due to these aberrations, the focusing conditions for light at the long and short wavelength edges of

the spectral range are not the same as for light in the middle. Thus light at the edges of the spectral range is partially defocused when contrast spectra are measured. For samples that do not completely fill the light spot, this might translate to a greater contribution from substrate reflectance at the edges of the spectral range. Chromatic aberrations should not be as significant of an issue for samples larger than the light spot. It should also be noted that even a single *G. sulfurreducens* cell is too thick to satisfy the thin-film condition $d \ll \lambda_0$, where d is the film thickness and λ_0 is the free space wavelength of the light. Thus the reflective contrast cannot be directly related to the film absorption in this case. (See Chapter 2.2.2 for a discussion of the relationship between reflective contrast and absorption for thin films.) Finally, reflection conditions in the system are complicated by the curvature of *G. sulfurreducens* single cells and films, unlike a relatively flat and homogeneous graphene sheet.

3.6.5 Resonance Raman Spectroscopy of G. sulfurreducens Cells

We have obtained Raman spectra of *G. sulfurreducens* cells using Q band excitation at 514.5 nm. Figure 3.17a shows the spectrum of a thick film of cells recorded with a 5 min integration time and 2 mW power. Several strong features are visible in the spectrum between 1100 – 1700 cm^{-1} and an intense band appears at approximately 2900 cm^{-1}. The sharp Raman features are superimposed on a structured background with broad peaks near 1500 cm^{-1} and 3000 cm^{-1}. The same spectrum in a narrower wavenumber range is plotted in Figure 3.17b. The Raman peaks are fit to Voigt functions with Gaussian full width at half maximum (FWHM) determined by our spectral resolution, 11.25 cm^{-1} for this data. Although the signal-to-noise ratio is not large for some of the peaks, and the noisy background may be obscuring others, several features

are clear. The strongest peak in this region is centered at 1586 cm^{-1}; this peak was also observed by Millo *et al.*[55] and Virdis *et al.*[56] in their studies of *Geobacter* spp. biofilms. (It should be noted that the former study used Soret band excitation while the latter used Q band excitation.) This peak is assigned to an asymmetric C_a-C_m stretch.[42] (See Figure 3.1a for porphyrin carbon atom labels.) Millo *et al.* found this band at 1592 cm^{-1} in reduced biofilms and 1588 cm^{-1} in oxidized biofilms. The peak at 1366 cm^{-1} is in the same region as the totally symmetric pyrrole half-ring stretch considered to be the best marker band for heme oxidation state. Millo *et al.* reported that this peak shifted from 1361 cm^{-1} to 1375 cm^{-1} upon biofilm oxidation. The band at 1640 cm^{-1} appeared in the oxidized biofilm spectrum obtained by Millo *et al.*, although it was weak. The peaks at 1130 cm^{-1} and 1315 cm^{-1} correspond to ones observed by Virdis *et al*. The broad band centered at 2900 cm^{-1} can be fit to two or three peaks; it presumably includes vibrations of water[56] and possibly additional contributions from C-H and N-H stretches.[75]

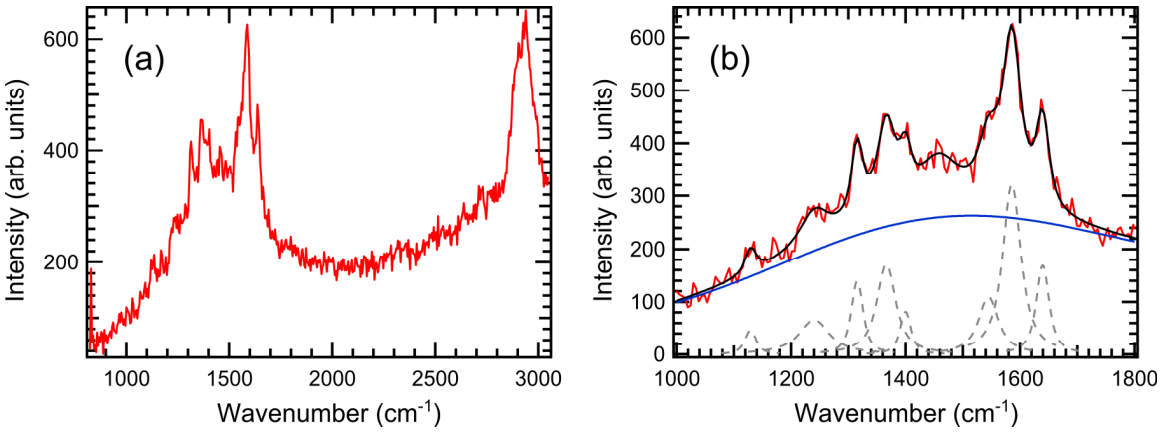

Figure 3.17 (a) Raman spectrum of a film of *G. sulfurreducens* cells supported on a quartz substrate in air. The excitation wavelength was 514.5 nm, the incident power was 2 mW, and the integration time was 5 min. (b) Same spectrum as in (a) in the 1000 – 1800 cm^{-1} region. The Raman peaks (grey dashed lines) are fit to Voigt functions with Gaussian FWHM = 11.25 cm^{-1} and the background is fit to a log polynomial function. Also shown is the overall fit (black line).

The main features in the Figure 3.17b spectrum are compiled in Table 3.6. As expected, the strongest *c*-type cytochrome peak that we observe with Q band excitation corresponds to the asymmetric C_a-C_m stretch at 1586 cm^{-1}.[42] In comparison to the spectra reported by Millo *et al.*,[55] this spectrum is consistent with *c*-type cytochromes primarily in the oxidized state, a reasonable result for cells exposed to air. Although the position of the pyrrole half-ring stretch is intermediate, at 1366 cm^{-1}, it is closer to the position of the mode in the oxidized biofilm. The position of the C_a-C_m asymmetric stretch at 1586 cm^{-1} and the presence of the mode at 1640 cm^{-1} are also consistent with oxidized hemes. It has also been demonstrated that the *c*-type cytochrome Raman modes

are weaker for heme in the oxidized state,[56] but our preliminary data do not allow us to confirm that finding.

Frequency (cm^{-1})	**Tentative Assignments and Notes**	**Observed in *Geobacter***
1129	C_a-N stretch[56]	Virdis *et al.*[56]
1240	—	Jarvis *et al.*[54]
1316	C_a-H bend[56]	Virdis *et al.*[56]
1366	Pyrrole half-ring symmetric stretch[48] Oxidation state marker band[42]	Millo *et al.*[55]
1400	—	Jarvis *et al.*[54]
1545	Possible oxidation state marker band[42]	Jarvis *et al.*[54]
1586	C_a-C_m asymmetric stretch[56] Spin state marker band[42]	Millo *et al.*[55] Virdis *et al.*[56]
1640	Possible spin state marker band[42]	Millo *et al.*[55] Jarvis *et al.*[54]

Table 3.6 Strongest Raman peaks from the Figure 3.17b Raman spectrum. Also listed are tentative literature assignments, notes about the bands, and observations of bands in similar positions in previous Raman studies of *Geobacter* spp. Porphyrin carbon atom labels are shown in Figure 3.1a.

Raman spectra can also be obtained from a single *G. sulfurreducens* cell, as in Figure 3.18a. Despite a lower signal-to-noise ratio, similar features are evident in the

spectrum. We note that the diameter of the focused laser spot in these measurements, approximately 0.5 μm, is comparable to the diameter of the cell and only a few times smaller than its length. Achieving higher signal-to-noise is challenging for single cells in air due to cytochrome photobleaching. Figure 3.18b shows four consecutive 5 min scans, starting with the Figure 3.18a spectrum, taken at the same spot on the single cell. Within the first ten minutes the intensity of the Raman peaks in the 1100 – 1700 cm^{-1} range drops significantly, as does the intensity of the background luminescence. The broad band at 2900 cm^{-1} is largely unaffected, however, supporting the hypothesis that the signal loss is due primarily to cytochrome photobleaching and not photodegradation of the cell itself.

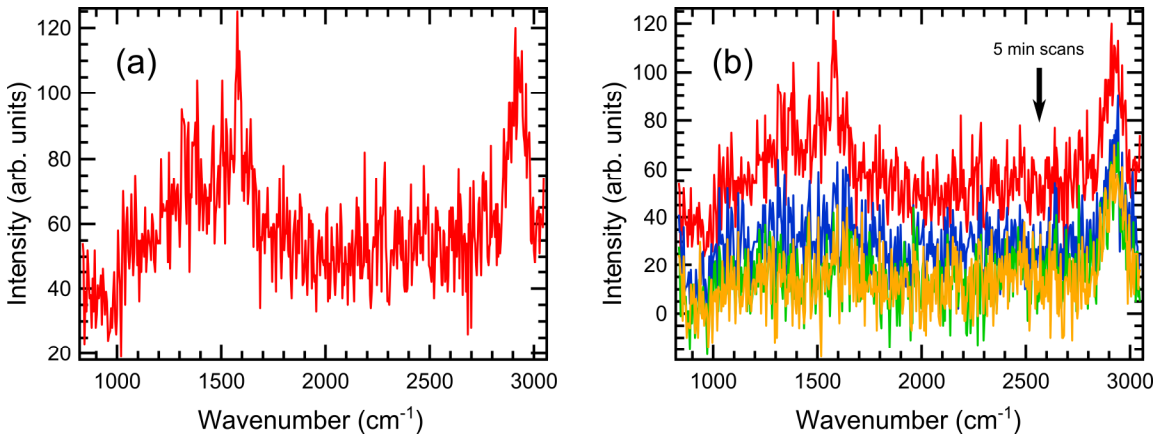

Figure 3.18 (a) Raman spectrum of a single *G. sulfurreducens* cell supported on a quartz substrate in air. The excitation wavelength was 514.5 nm, the incident power was 2 mW, and the integration time was 5 min. (b) Four consecutive 5 min Raman spectra, starting with the spectrum in (a), taken at the same spot.

3.7 Summary and Outlook

In summary, we have made progress in culturing and characterizing the model DMRB *G. sulfurreducens*. We have routinely cultured *G. sulfurreducens* using fumarate as an electron acceptor and have begun to characterize its growth on insoluble iron oxides, a more environmentally relevant electron acceptor for this bacterium. The identity of *G. sulfurreducens* has been confirmed by 16S rRNA sequencing, and we have verified the expression of pili using TEM imaging and SDS-PAGE. Preliminary micro-Raman studies confirm that we can obtain Raman spectra from *G. sulfurreducens* cells, and characteristic *c*-type cytochrome peaks can be resolved in the spectra. We have made initial attempts to probe the electronic absorption of *c*-type cytochromes using micro-contrast spectroscopy and dark field Rayleigh scattering spectroscopy.

Future experiments will build on these preliminary optical studies. We have made improvements to our micro-Raman setup to achieve higher collection efficiency and a better signal-to-noise ratio; these changes should allow us to obtain clearer Raman spectra with shorter integration times. In the initial Raman measurements described here we have used the 514.5 nm Ar^+ laser line for excitation, which is resonant with the heme Q band. We have recently started working to add a 406 nm diode laser to our micro-Raman setup, which will allow us to obtain resonance Raman spectra with Soret band excitation. The heme Raman scattering cross-section should be enhanced at this excitation wavelength, and the oxidation state marker band, in particular, will be stronger. We will also work to develop devices that will allow us to make electrical contact to *G. sulfurreducens* cells for combined electrical and optical studies. Our first experiments might involve depositing cells or even a single cell on a substrate with thin graphite

flakes connected to electrodes. We should be able to tune the oxidation state of the cell by applying a potential to the graphite electrode and we can monitor the Raman spectra and the current throughout the measurement. There might be considerable heterogeneity in the cellular response, and something might be learned from this variation. We might also try to study charge transport through a thin film of *G. sulfurreducens* cells between two electrodes using optical and electrical methods in a smaller-scale version of the electrical studies reported by Malvankar *et al.*[38] We note that Jiang *et al.* demonstrated *in situ* electrical measurements and phase-contrast microscopy of *S. oneidensis* cells on a nanoelectrode substrate.[76] A similar method might be developed for spectroscopic and electric studies of *G. sulfurreducens*. On the biochemical side, it may be important to work with *c*-type cytochrome mutants of *G. sulfurreducens*. As discussed in Chapter 3.2.2, it has been demonstrated that different cytochrome proteins have distinct electron transport roles in *G. sulfurreducens*, although there may also be significant redundancy and the capability for adaptation. Following these approaches we hope to address some of the outstanding questions described earlier in this chapter about electron transport mechanisms in the model DMRB *G. sulfurreducens*.

3.8 References

(1) Madigan, M. T.; Martinko, J. M.; Parker, J. *Brock biology of microorganisms*; 9th ed.; Prentice Hall: Upper Saddle River, NJ, 2000.

(2) Mahadevan, R.; Palsson, B. O.; Lovley, D. R. *Nat Rev Microbiol* **2011**, *9*, 39.

(3) Lovley, D. R.; Holmes, D. E.; Nevin, K. P. *Advances in Microbial Physiology, Vol. 49* **2004**, *49*, 219.

(4) Lovley, D. R.; Phillips, E. J. P. *Appl Environ Microb* **1988**, *54*, 1472.

(5) Lovley, D. R.; Giovannoni, S. J.; White, D. C.; Champine, J. E.; Phillips, E. J. P.; Gorby, Y. A.; Goodwin, S. *Arch Microbiol* **1993**, *159*, 336.

(6) Lovley, D. R.; Ueki, T.; Zhang, T.; Malvankar, N. S.; Shrestha, P. M.; Flanagan, K. A.; Aklujkar, M.; Butler, J. E.; Giloteaux, L.; Rotaru, A. E.; Holmes, D. E.; Franks, A. E.; Orellana, R.; Risso, C.; Nevin, K. P. *Adv Microb Physiol* **2011**, *59*, 1.

(7) Bird, L. J.; Bonnefoy, V.; Newman, D. K. *Trends Microbiol* **2011**, *19*, 330.

(8) Bard, A. J.; Faulkner, L. R. *Electrochemical methods : fundamentals and applications*; 2nd ed.; Wiley: New York, 2001.

(9) Nealson, K. H.; Finkel, S. E. *Mrs Bull* **2011**, *36*, 380.

(10) Marsili, E.; Baron, D. B.; Shikhare, I. D.; Coursolle, D.; Gralnick, J. A.; Bond, D. R. *Proceedings of the National Academy of Sciences* **2008**, *105*, 3968.

(11) von Canstein, H.; Ogawa, J.; Shimizu, S.; Lloyd, J. R. *Appl Environ Microb* **2008**, *74*, 615.

(12) Shi, L.; Squier, T. C.; Zachara, J. M.; Fredrickson, J. K. *Mol Microbiol* **2007**, *65*, 12.

(13) Lloyd, J. R.; Leang, C.; Myerson, A. L. H.; Coppi, M. V.; Cuifo, S.; Methe, B.; Sandler, S. J.; Lovley, D. R. *Biochem J* **2003**, *369*, 153.

(14) Leang, C.; Coppi, M. V.; Lovley, D. R. *J Bacteriol* **2003**, *185*, 2096.

(15) Mehta, T.; Coppi, M. V.; Childers, S. E.; Lovley, D. R. *Appl Environ Microb* **2005**, *71*, 8634.

(16) Bretschger, O.; Obraztsova, A.; Sturm, C. A.; Chang, I. S.; Gorby, Y. A.; Reed, S. B.; Culley, D. E.; Reardon, C. L.; Barua, S.; Romine, M. F.; Zhou, J.; Beliaev, A. S.; Bouhenni, R.; Saffarini, D.; Mansfeld, F.; Kim, B.-H.; Fredrickson, J. K.; Nealson, K. H. *Appl Environ Microb* **2007**, *73*, 7003.

(17) Voordeckers, J. W.; Kim, B. C.; Izallalen, M.; Lovley, D. R. *Appl Environ Microb* **2010**, *76*, 2371.

(18) Lovley, D. R. *Nat Rev Microbiol* **2006**, *4*, 497.

(19) Reguera, G.; Nevin, K. P.; Nicoll, J. S.; Covalla, S. F.; Woodard, T. L.; Lovley, D. R. *Appl Environ Microb* **2006**, *72*, 7345.

(20) Holmes, D. E.; Chaudhuri, S. K.; Nevin, K. P.; Mehta, T.; Methe, B. A.; Liu, A.; Ward, J. E.; Woodard, T. L.; Webster, J.; Lovley, D. R. *Environ Microbiol* **2006**, *8*, 1805.

(21) Nevin, K. P.; Kim, B. C.; Glaven, R. H.; Johnson, J. P.; Woodard, T. L.; Methe, B. A.; DiDonato, R. J.; Covalla, S. F.; Franks, A. E.; Liu, A.; Lovley, D. R. *Plos One* **2009**, *4*.

(22) Caccavo, F.; Lonergan, D. J.; Lovley, D. R.; Davis, M.; Stolz, J. F.; Mcinerney, M. J. *Appl Environ Microb* **1994**, *60*, 3752.

(23) Lin, W. C.; Coppi, M. V.; Lovley, D. R. *Appl Environ Microb* **2004**, *70*, 2525.

(24) Methe, B. A.; Nelson, K. E.; Eisen, J. A.; Paulsen, I. T.; Nelson, W.; Heidelberg, J. F.; Wu, D.; Wu, M.; Ward, N.; Beanan, M. J.; Dodson, R. J.; Madupu, R.; Brinkac, L. M.; Daugherty, S. C.; DeBoy, R. T.; Durkin, A. S.; Gwinn, M.; Kolonay, J. F.; Sullivan, S. A.; Haft, D. H.; Selengut, J.; Davidsen, T. M.; Zafar, N.; White, O.; Tran, B.; Romero, C.; Forberger, H. A.; Weidman, J.; Khouri, H.; Feldblyum, T. V.; Utterback, T. R.; Van Aken, S. E.; Lovley, D. R.; Fraser, C. M. *Science* **2003**, *302*, 1967.

(25) Ding, Y. H. R.; Hixson, K. K.; Giometti, C. S.; Stanley, A.; Esteve-Nunez, A.; Khare, T.; Tollaksen, S. L.; Zhu, W. H.; Adkins, J. N.; Lipton, M. S.; Smith, R. D.; Mester, T.; Lovley, D. R. *Bba-Proteins Proteom* **2006**, *1764*, 1198.

(26) Ding, Y. H. R.; Hixson, K. K.; Aklujkar, M. A.; Lipton, M. S.; Smith, R. D.; Lovley, D. R.; Mester, T. *Bba-Proteins Proteom* **2008**, *1784*, 1935.

(27) Coppi, M. V.; Leang, C.; Sandler, S. J.; Lovley, D. R. *Appl Environ Microb* **2001**, *67*, 3180.

(28) Esteve-Núñez, A.; Sosnik, J.; Visconti, P.; Lovley, D. R. *Environ Microbiol* **2008**, *10*, 497.

(29) Leang, C.; Qian, X. L.; Mester, T.; Lovley, D. R. *Appl Environ Microb* **2010**, *76*, 4080.

(30) Craig, L.; Pique, M. E.; Tainer, J. A. *Nat Rev Microbiol* **2004**, *2*, 363.

(31) Hansen, J. K.; Forest, K. T. *J Mol Microb Biotech* **2006**, *11*, 192.

(32) Craig, L.; Li, J. *Curr Opin Struc Biol* **2008**, *18*, 267.

(33) Proft, T.; Baker, E. N. *Cell Mol Life Sci* **2009**, *66*, 613.

(34) Reguera, G.; McCarthy, K. D.; Mehta, T.; Nicoll, J. S.; Tuominen, M. T.; Lovley, D. R. *Nature* **2005**, *435*, 1098.

(35) Richter, L. V.; Sandler, S. J.; Weis, R. M. *J Bacteriol* **2012**, *194*, 2551.

(36) Klimes, A.; Franks, A. E.; Glaven, R. H.; Tran, H.; Barrett, C. L.; Qiu, Y.; Zengler, K.; Lovley, D. R. *Fems Microbiol Lett* **2010**, *310*, 62.

(37) Veazey, J. P.; Reguera, G.; Tessmer, S. H. *Phys Rev E* **2011**, *84*.

(38) Malvankar, N. S.; Vargas, M.; Nevin, K. P.; Franks, A. E.; Leang, C.; Kim, B. C.; Inoue, K.; Mester, T.; Covalla, S. F.; Johnson, J. P.; Rotello, V. M.; Tuominen, M. T.; Lovley, D. R. *Nat Nanotechnol* **2011**, *6*, 573.

(39) Richter, H.; Nevin, K. P.; Jia, H. F.; Lowy, D. A.; Lovley, D. R.; Tender, L. M. *Energ Environ Sci* **2009**, *2*, 506.

(40) Liu, Y.; Kim, H.; Franklin, R. R.; Bond, D. R. *Chemphyschem* **2011**, *12*, 2235.

(41) Falk, J. E. *Porphyrins and metalloporphyrins; their general, physical and coordination chemistry, and laboratory methods*; Elsevier Pub. Co.: Amsterdam, New York,, 1964.

(42) Spiro, T. G.; Strekas, T. C. *Journal of the American Chemical Society* **1974**, *96*, 338.

(43) Horio, T.; Kamen, M. D. *Annual Review of Microbiology* **1970**, *24*, 399.

(44) Nemykin, V. N.; Hadt, R. G. *The Journal of Physical Chemistry A* **2010**, *114*, 12062.

(45) Myers, A. B. *J Raman Spectrosc* **1997**, *28*, 389.

(46) Kelley, A. M. *J Phys Chem A* **2008**, *112*, 11975.

(47) Le Ru, E. C.; Schroeter, L. C.; Etchegoin, P. G. *Anal Chem* **2012**, *84*, 5074.

(48) Desbois, A. *Biochimie* **1994**, *76*, 693.

(49) Hu, S.; Morris, I. K.; Singh, J. P.; Smith, K. M.; Spiro, T. G. *Journal of the American Chemical Society* **1993**, *115*, 12446.

(50) Champion, P. M.; Albrecht, A. C. *The Journal of Chemical Physics* **1979**, *71*, 1110.

(51) Pasternack, R. F.; Collings, P. J. *Science* **1995**, *269*, 935.

(52) Reinisch, L.; Schomacker, K. T.; Champion, P. M. *J Chem Phys* **1987**, *87*, 150.

(53) Chiarello, R.; Reinisch, L. *J Chem Phys* **1988**, *88*, 1253.

(54) Jarvis, R. M.; Law, N.; Shadi, I. T.; O'Brien, P.; Lloyd, J. R.; Goodacre, R. *Anal Chem* **2008**, *80*, 6741.

(55) Millo, D.; Harnisch, F.; Patil, S. A.; Ly, H. K.; Schroder, U.; Hildebrandt, P. *Angew Chem Int Ed Engl* **2011**, *50*, 2625.

(56) Virdis, B.; Harnisch, F.; Batstone, D. J.; Rabaey, K.; Donose, B. C. *Energ Environ Sci* **2012**, *5*, 7017.

(57) Busalmen, J. P.; Esteve-Nunez, A.; Berna, A.; Feliu, J. M. *Bioelectrochemistry* **2010**, *78*, 25.

(58) Strycharz-Glaven, S. M.; Snider, R. M.; Guiseppi-Elie, A.; Tender, L. M. *Energ Environ Sci* **2011**, *4*, 4366.

(59) Polizzi, N. F.; Skourtis, S. S.; Beratan, D. N. *Faraday Discuss* **2012**, *155*, 43.

(60) Pirbadian, S.; El-Naggar, M. Y. *Phys Chem Chem Phys* **2012**.

(61) Speers, A. M.; Cologgi, D. L.; Reguera, G. *Curr Protoc Microbiol* **2009**, *Appendix 4*, Appendix 4F.

(62) Jambor, J. L.; Dutrizac, J. E. *Chem Rev* **1998**, *98*, 2549.

(63) Lovley, D. R.; Phillips, E. J. P. *Appl Environ Microb* **1986**, *51*, 683.

(64) Raven, K. P.; Jain, A.; Loeppert, R. H. *Environ Sci Technol* **1998**, *32*, 344.

(65) Bradford, M. M. *Analytical Biochemistry* **1976**, *72*, 248.

(66) Suter, D.; Siffert, C.; Sulzberger, B.; Stumm, W. *Naturwissenschaften* **1988**, *75*, 571.

(67) Jiao, Y. Y. Q.; Kappler, A.; Croal, L. R.; Newman, D. K. *Appl Environ Microb* **2005**, *71*, 4487.

(68) Rollefson, J. B.; Stephen, C. S.; Tien, M.; Bond, D. R. *J Bacteriol* **2011**, *193*, 1023.

(69) Yu, Z. H.; Brus, L. *Journal of Physical Chemistry B* **2001**, *105*, 1123.

(70) Sfeir, M. Y.; Wang, F.; Huang, L. M.; Chuang, C. C.; Hone, J.; O'Brien, S. P.; Heinz, T. F.; Brus, L. E. *Science* **2004**, *306*, 1540.

(71) Joh, D. Y.; Herman, L. H.; Ju, S. Y.; Kinder, J.; Segal, M. A.; Johnson, J. N.; Chan, G. K. L.; Park, J. *Nano Letters* **2011**, *11*, 1.

(72) Brus, L. *Accounts of Chemical Research* **2008**, *41*, 1742

(73) Macnab, R. M. *Journal of Clinical Microbiology* **1976**, *4*, 258.

(74) Jackson, J. D. *Classical electrodynamics*; 3rd ed.; Wiley: New York, 1999.

(75) Patzold, R.; Keuntje, M.; Theophile, K.; Muller, J.; Mielcarek, E.; Ngezahayo, A.; Ahlften, A. A. V. *J Microbiol Meth* **2008**, *72*, 241.

(76) Jiang, X.; Hu, J.; Fitzgerald, L. A.; Biffinger, J. C.; Xie, P.; Ringeisen, B. R.; Lieber, C. M. *Proceedings of the National Academy of Sciences* **2010**, *107*, 16806.